| | |
|---|---|
| **Titre:** Title: | An Efficient Approach for Electromagnetic Transient Modeling of Electric Vehicle Power System |
| **Auteur:** Author: | Seyedarmin Mirnikjoo |
| **Date:** | 2026 |
| **Type:** | Mémoire ou thèse / Dissertation or Thesis |
| **Référence:** Citation: | Mirnikjoo, S. (2026). An Efficient Approach for Electromagnetic Transient Modeling of Electric Vehicle Power System [Thèse de doctorat, Polytechnique Montréal]. PolyPublie. https://publications.polymtl.ca/73224/ |

**POLYTECHNIQUE MONTRÉAL**

affiliée à l'Université de Montréal

# An Efficient Approach for Electromagnetic Transient Modeling of Electric Vehicle Power System

**SEYEDARMIN MIRNIKJOO**

Département de génie électrique

Thèse présentée en vue de l'obtention du diplôme de *Philosophiæ Doctor*

Génie électrique

Février 2026

**POLYTECHNIQUE MONTRÉAL**

affiliée à l'Université de Montréal

Cette thèse intitulée :

# An Efficient Approach for Electromagnetic Transient Modeling of Electric Vehicle Power System

présentée par **Seyedarmin MIRNIKJOO**

en vue de l'obtention du diplôme de *Philosophiæ Doctor*

a été dûment acceptée par le jury d'examen constitué de :

**Antoine LESAGE-LANDRY**, président
**Jean MAHSEREDJIAN**, membre et directeur de recherche
**Paul AKIKI**, membre et codirecteur de recherche
**Nicolas BRACIKOWSKI**, membre et codirecteur de recherche
**Keyhan SHESHYEKANI**, membre
**Berker BILGIN**, membre externe

# DEDICATION

*Dedicated to my beloved parents*

# ACKNOWLEDGEMENTS

I would like to sincerely thank my supervisor, Prof. Jean Mahseredjian, for his exceptional guidance, insightful feedback, and unwavering support throughout my Ph.D. journey. Working under his supervision has been a truly inspiring experience. His extensive knowledge and expertise in the field of electromagnetic transients have provided me with an invaluable opportunity to develop a solid understanding and gain considerable expertise in this field.

I am also grateful to Prof. Nicolas Braciskowski for his valuable guidance, constructive suggestions, and continuous support throughout my research. I would like to extend my appreciation to Paul Akiki at *Électricité de France* for their collaboration. I would also like to acknowledge the contributions of Mohammed Naidjate to this Ph.D. thesis.

I wish to thank my lab colleagues, Juan Antonio Ocampo Wilches, Mohammad Jafari Matehkolaei, Ahmad Allabadi, Renan Morais Furlaneto, Anoosh Dini, Kouame N'zi for their friendship, support, and the stimulating research environment we shared.

Words can never fully express my gratitude to my family for the sacrifices they have always made, like a candle that burns itself to illuminate the path for others. They have been an unwavering source of love, endless care, and constant support throughout my Ph.D. journey and at every step of my life.

# RÉSUMÉ

Cette thèse propose une représentation basée sur des circuits pour les études au niveau du système des systèmes d'entraînement électrique et de leurs systèmes électriques environnants, représentant le système de puissance d'un véhicule électrique. Le principal défi dans le développement de ce modèle réside dans la modélisation précise et efficace de la machine électrique. Pour y répondre, une approche basée sur des circuits est utilisée pour développer les modèles transitoires électromagnétiques (EMT) de la machine électrique. Ces modèles sont constitués de circuits équivalents magnétiques, électriques et mécaniques interconnectés.

Divers circuits magnétiques sont proposés afin de développer un modèle EMT approprié de la machine électrique pour différents types d'études transitoires. Dans cette thèse, une machine à réluctance variable (SRM) et son système d'entraînement sont utilisés comme étude de cas. Tous les modèles utilisent une approche sans maillage afin de prendre en compte la rotation de la machine de manière efficace sur le plan computationnel, ce qui est adapté aux simulations transitoires. Tous les modèles proposés sont intégrés de manière transparente avec le circuit externe par une solution simultanée. Les modèles sont implémentés dans un solveur EMT développé en langage Julia, où le système matriciel du réseau est construit selon l'analyse nodale augmentée modifiée (MANA) et résolu à l'aide du solveur KLU.

Pour les études transitoires portant sur les phénomènes internes à la machine ou visant à étudier son comportement interne détaillé et local, un modèle distribué basé sur des circuits est proposé. Dans ce modèle, les circuits magnétiques du stator et du rotor sont construits selon une approche basée sur un maillage, la précision du modèle dépendant du nombre de divisions du maillage. La comparaison entre les performances de ce modèle et un modèle basé sur les éléments finis montre que le modèle proposé atteint non seulement une bonne précision, mais offre également une charge computationnelle réduite. Le modèle distribué basé sur des circuits est intégré de manière transparente dans le système d'entraînement pour étudier les défauts internes de la machine. De plus, ce modèle est intégré dans une étude de cas représentant le système de puissance d'un véhicule électrique. L'impact des défauts du système de batterie sur le comportement transitoire de l'ensemble du système et sur le comportement magnétique interne de la machine est analysé.

Pour les phénomènes transitoires se produisant à l'extérieur de la machine, un modèle distribué simplifié basé sur des circuits est proposé. Ce modèle utilise un nombre réduit de divisions de

maillage dans la direction orthoradiale tout en conservant une précision acceptable, offrant ainsi des simulations plus rapides par rapport aux modèles distribués. Le modèle distribué simplifié est utilisé pour étudier les effets des variations soudaines de charge et de vitesse de la machine sur le comportement du système.

Un modèle topologique basé sur des circuits, utilisant une approche sans maillage pour construire le circuit magnétique de la machine, est utilisé pour simuler un défaut en circuit ouvert au point de connexion entre le convertisseur électronique de puissance et les enroulements de phase de la machine, ainsi qu'un court-circuit dans le système de batterie.

Afin d'obtenir une simulation rapide tout en maintenant une précision acceptable sur le comportement global de la machine, le modèle basé sur des circuits concentrés (lumped) est proposé. Bien que ce modèle soit moins précis que les modèles précédemment mentionnés, il nécessite un effort computationnel réduit. Il est utilisé pour étudier l'impact des variations des commandes de vitesse de la machine sur le comportement transitoire du système d'entraînement.

# ABSTRACT

This thesis proposes a circuit-based representation for system-level studies of motor drive systems and their surrounding power systems, which represents the electric vehicle's power system. The primary challenge in developing this model lies in accurately and efficiently modeling the electric machine. To address this, a circuit-based approach is employed to develop the electromagnetic transient (EMT) models of the electric machine. These models consist of interconnected magnetic, electrical, and mechanical equivalent circuits.

Various magnetic circuits are proposed to develop an appropriate EMT model of the electric machine for different types of transient studies. In this thesis, a switched reluctance machine (SRM) and its drive system are used as the case study. All models use a non-meshed approach to account for the machine's rotation in a computationally efficient way, which is suitable for transient simulations. All proposed models are seamlessly integrated with the external power circuit through a simultaneous solution. The models are implemented in an EMT solver developed in the Julia programming language, where the network matrix system is constructed based on modified augmented nodal analysis (MANA) and solved by the KLU solver.

For transient studies that focus on phenomena occurring inside the machine or aim to study its detailed and local internal behavior, a distributed circuit-based model of the machine is proposed. In this model, the magnetic circuits within the stator and rotor are constructed using a mesh-based approach, where the model's accuracy depends on the number of mesh divisions. The comparison between the performance of this model and a finite element-based model shows that the proposed model not only achieves good accuracy but also provides a lower computational burden. The distributed circuit-based model is seamlessly integrated into the drive system to study the internal fault of the machine. Moreover, this model is integrated into a case study representing an electric vehicle power system. The impact of faults in the battery system on the transient behavior of the whole system and the internal magnetic behavior of the machine is analyzed.

For transient phenomena occurring outside the machine, a simplified distributed circuit-based model is proposed. This model uses a reduced number of mesh divisions in the orthoradial direction while maintaining acceptable accuracy, offering faster simulation performance compared to distributed models. The simplified distributed circuit-based model is used to study the effects of sudden changes in the machine's load and speed on the system behavior.

A topological circuit-based model, which uses a non-meshed approach to build the magnetic circuit of the machine, is used to simulate an open-circuit fault at the connection point between the power electronics converter and the machine's phase windings, as well as a short circuit in the battery system.

To achieve fast simulation while maintaining acceptable accuracy in the global behavior of the machine, the lumped circuit-based model is proposed. Although this model is less accurate than the previously mentioned models, it offers less computational effort. It is used to study the impact of changes in the machine's speed commands on the transient behavior of the motor drive system.

# TABLE OF CONTENTS

# LIST OF TABLES

# LIST OF FIGURES

# LISTE OF SYMBOLS AND ABBREVIATIONS

EMT Electromagnetic Transient

EV Electric Vehicle

FEM Finite Element Method

SRM Switched Reluctance Machine

MMF Magnetomotive Force

EMF Electromotive Force

IGBT Insulated Gate Bipolar Transistor

SOC State of Charge

Li-Ion lithium-ion

MANA Modified Augmented Nodal Analysis

CoSim-FEM Co-Simulation of FEM and circuit-based software

CBEMT Circuit-Based Electromagnetic Transient

TCM Tooth Contour Method

EXP Exponential

S-CBEMT Simplified Distributed Circuit-Based Electromagnetic Transient.

# CHAPTER 1 INTRODUCTION

## 1.1 Context and Motivation

Electric vehicles (EVs) are gaining considerable attention as an environmentally friendly means of transportation. The power system of EV consists of several interconnected components, including the battery, power converters, electric machine, and their related control systems, as shown in Figure 1.1.

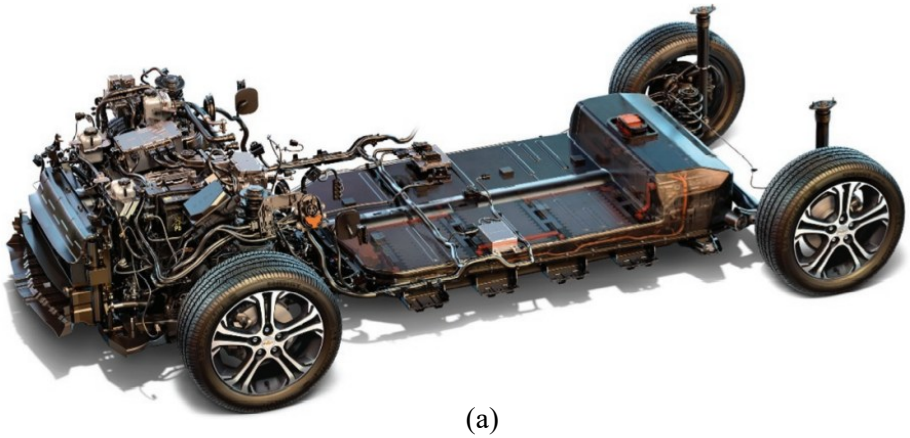

(a)

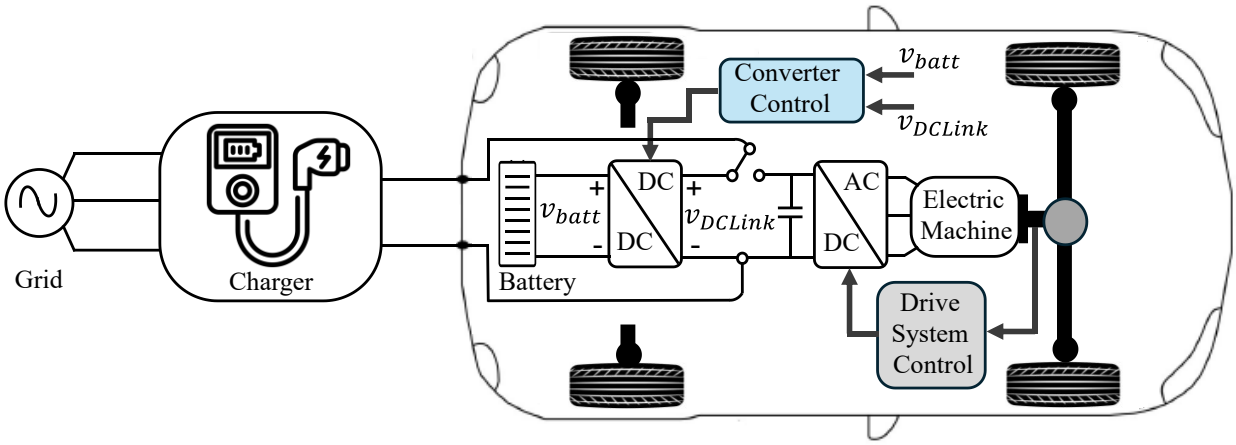


(b)

Figure 1.1 EV's power system, (a) a real EV [1], (b) schematic diagram [2]

Accurate and efficient modeling of an EV's power system requires a detailed representation of its components, while considering their interactions with each other. Among the components of an EV power system, the electric machine is considered the most challenging to model. The electric machine has highly nonlinear magnetic behavior and involves interactions between various

physical domains, including electrical, magnetic, mechanical, etc. Additionally, the performance of electric machines strongly depends on their drive and control systems, making it essential to accurately model the interaction between the drive system and the machine. Therefore, the machine's model should be capable of considering the nonlinear behavior of the machine, the interaction between its various physical behaviors, and the efficient integration within the EV power systems.

## 1.2 Contributions

This thesis develops the comprehensive EMT model of the system shown in Figure 1.2. This system represents the EV's power system. Developing the comprehensive EMT model of this system allows studying various transient phenomena occurring throughout the system and their impact on the internal behavior of each component.

Developing an accurate EMT model of the electric machine that can be computationally efficiently integrated into the external power system is an important step toward building the comprehensive EMT model of an EV power system. In this regard, the circuit-based approach is used to develop the EMT model of the electric machine. The circuit-based EMT model of the electric machine can be implemented in EMT-type software which offers an extensive library of components, ranging from transmission lines to power electronics devices and control diagram blocks. Therefore, the EMT model of the machine can be seamlessly integrated within any external power system.

In this thesis, the machine's EMT model is built by the seamless coupling of the magnetic circuit with the electric and mechanical circuits, enabling simultaneous solution integration of the machine's EMT model into the large external power system, like the power system of EVs, as shown in Figure 1.2. Also, the machine's EMT model accounts for geometrical and physical characteristics of the electric machine. In this regard, various magnetic circuits are developed and proposed in this thesis. These magnetic circuits range from basic representations to detailed models that account for all detailed magnetic behavior of the machine. These magnetic circuits are suitable for various transient studies happening inside and outside of the machine.

In all proposed models of electric machine, the non-meshed approach is used to model the machine's airgap. Using this method enables modeling the machine's rotation without changing the magnetic circuit topology. This method is suitable for transient studies where we have sudden changes in machine's speed.

The closest works to the machine's model proposed in this thesis are presented in [3] and [4]. However, in [3], the airgap is modeled by mesh-based approach which requires changing the topology of magnetic circuit at each time point. Using a mesh-based approach for modeling the airgap is not suitable for transient studies where we have sudden changes in the machine's speed. In [4], the non-meshed approach is used to model machine's airgap. However, the study is limited to the magnetic domain, and the magnetic circuits are not coupled with the electrical and mechanical circuits, nor with any external system.

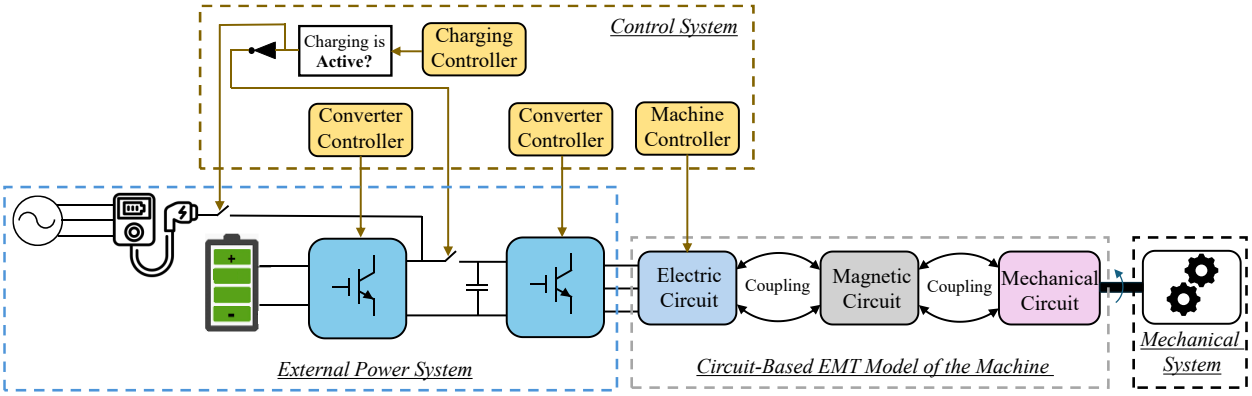


Figure 1.2 Concept of the circuit-based EMT model of electric machine and its integration within the external power system

## 1.3 Case Study

A 3-phase switched reluctance machine (SRM) with 12 stator poles and 8 rotor teeth, named 12/8 SRM, and its drive system are selected as the case study in this thesis. The detailed specifications and the working principle of this case study are demonstrated in this section.

### 1.3.1 Specification of the Studied SRM

The geometrical specification of the studied SRM is presented in Table 1-1. Figure 1.3 shows the geometric specification of the studied 12/8 SRM [3] .Also, Table 1-2 presents the drive system and mechanical specifications of the studied case.

Table 1-1 Geometric specification of the studied SRM

| **Parameter** | **Symbol** | **Value** | **Unit** |
|---|---|---|---|
| Stator outer radius | $R_o$ | 68 | [mm] |
| Shaft radius | $R_{sh}$ | 12.5 | [mm] |
| Stack length | $L_{stk}$ | 70 | [mm] |
| Airgap length | $g$ | 0.3 | [mm] |
| Rotor tooth angle | $\beta_{t_r}$ | 15 | [deg] |
| Stator tooth angle | $\beta_{t_s}$ | 15 | [deg] |
| Stator pole height | $h_s$ | 14.9 | [mm] |
| Rotor pole height | $h_r$ | 11 | [mm] |
| Stator yoke thickness | $h_{b_s}$ | 11.3 | [mm] |
| Rotor yoke thickness | $h_{b_r}$ | 18 | [mm] |
| Number of turns per coil | $N_t$ | 28 | - |

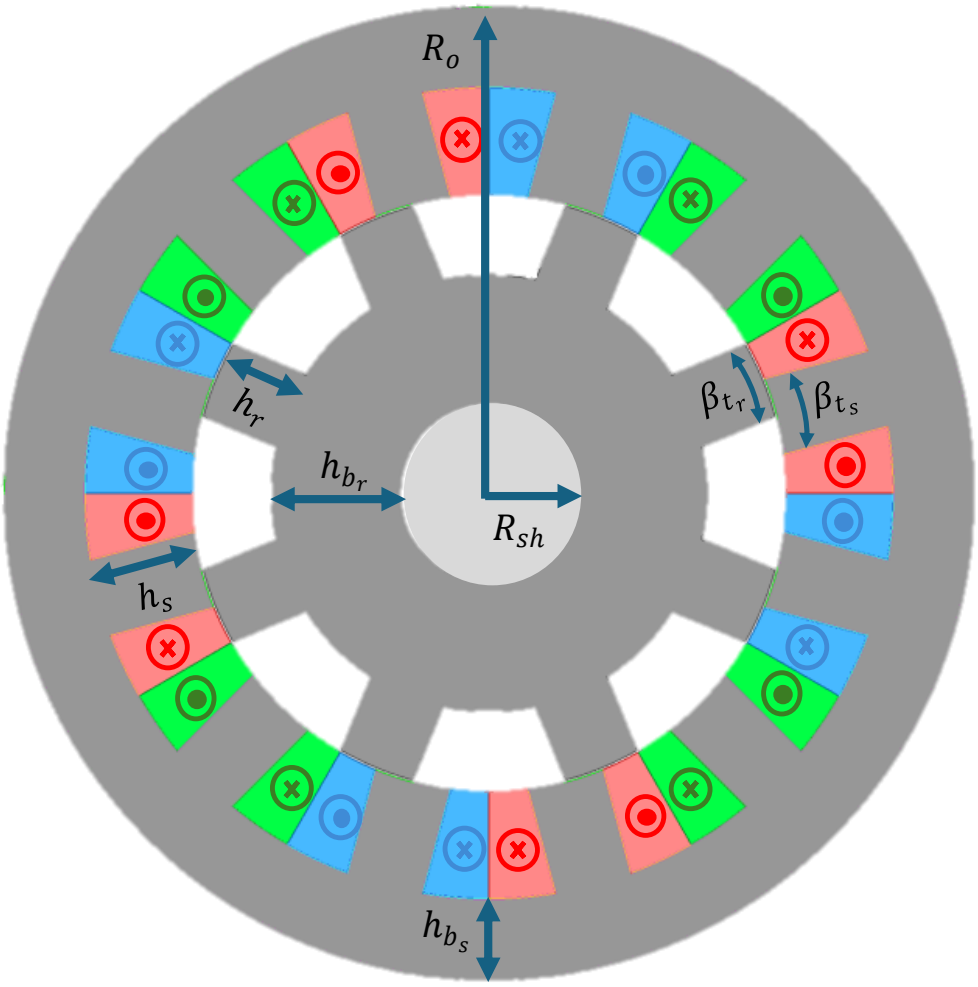


Figure 1.3 The geometric specification of the studied 12/8 SRM

Table 1-2 SRM's mechanical and drive system's specifications

| Parameter | Symbol | Value | Unit |
|---|---|---|---|
| Rotor moment of inertia | $J_m$ | 0.0003318 | [kg.m$^2$] |
| Damping coefficient | $D_m$ | 0.000608 | [Nm.s/rad] |
| Load Torque Coefficient | $A_\omega$ | 0.0171 | [Nm/rad] |
| Turn ON angle | $\theta_{on}$ | 0 | [deg] |
| Turn OFF angle | $\theta_{off}$ | 22.5 | [deg] |
| DC link voltage | $V_{DC}$ | 300 | [V] |
| Phase peak current | $I_{ref}$ | 20 | [A] |

### 1.3.2 Working Principle of SRM

The drive system of SRMs consists of the power electronics converter, electric machine, and control system. Figure 1.4 shows a schematic diagram of an SRM drive system.

Continuous torque production of SRM relies on the sequential excitation of its phase windings via a power converter. The sequential excitation of SRM phase windings is enabled by the position control. As shown in Figure 1.4, the rotor position $\theta$ is fed back to the control system, which generates phase pulses ($S_A$, $S_B$, and $S_C$ in Figure 1.4). The width of these pulses corresponds to the difference between the turn ON $\theta_{on}$ and turn OFF angles $\theta_{off}$. In addition to the position control, the hysteresis current control is implemented to maintain the SRM phase current at the reference current $I_{ref}$. As illustrated in Figure 1.4, the SRM phase currents ($i_A$, $i_B$, and $i_C$) are fed back into the controller to keep the phase currents within the defined bandwidth of the hysteresis current controller $bw$ [5].

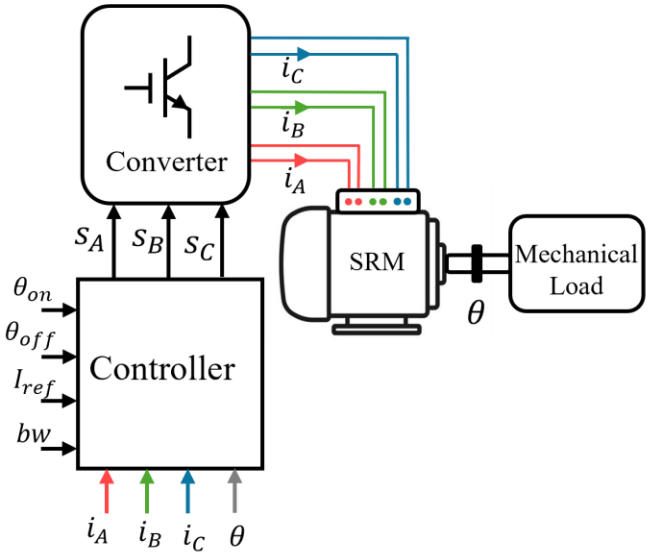


Figure 1.4 Schematic diagram of SRM drive system

Various types of power converters have been proposed for use in the drive systems of SRM. The asymmetric bridge converter is the most commonly used due to its several advantages, such as:

1) Independent control of each phase
2) Simplicity
3) High fault tolerance
4) Possibility of returning the machine's phase current to the DC link.

Therefore, the asymmetric bridge converter is employed as the power converter for the SRM drive system in this thesis. Figure 1.5 shows the schematic circuit of the three-phases asymmetric bridge converter. As depicted in this figure, each phase of this converter consists of two insulated gate bipolar transistors (IGBTs) and two diodes [5].

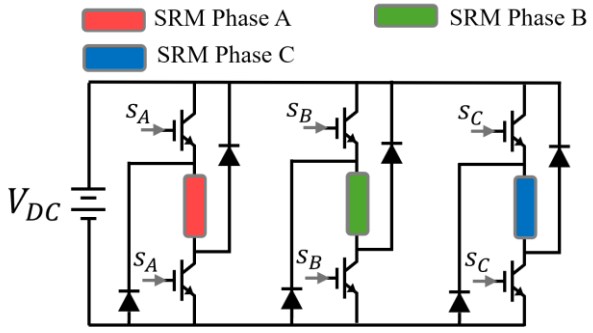


Figure 1.5 Asymmetric bridge converter

Each phase of the asymmetric bridge converter operates in three modes: energization, freewheeling, and de-energization, as shown in Figure 1.6. In the energization mode, the IGBTs are conducting, and it will energize the phase coils of the machine, as shown in Figure 1.6 (a). Figure 1.6 (b) and Figure 1.6 (c) illustrate the freewheeling mode where zero voltage is applied across the phase winding. The de-energization mode occurs when both IGBTs are turned off, allowing the phase current to return to the DC link and thereby de-energize the machine's phase coil, as shown in Figure 1.6 (d). This working principle results in the phase voltage and current waveforms shown in the Figure 1.6 (e), where the conduction angle is controlled by the rotor position. The phase conducts for a duration corresponding to a conduction angle of $\theta_{cond}$ degrees which is equal to

$$\theta_{cond} = \theta_{off} - \theta_{on} \tag{1.1}$$

The hysteresis current control limits the phase current to its reference value $I_{ref}$ within a defined bandwidth $bw$.

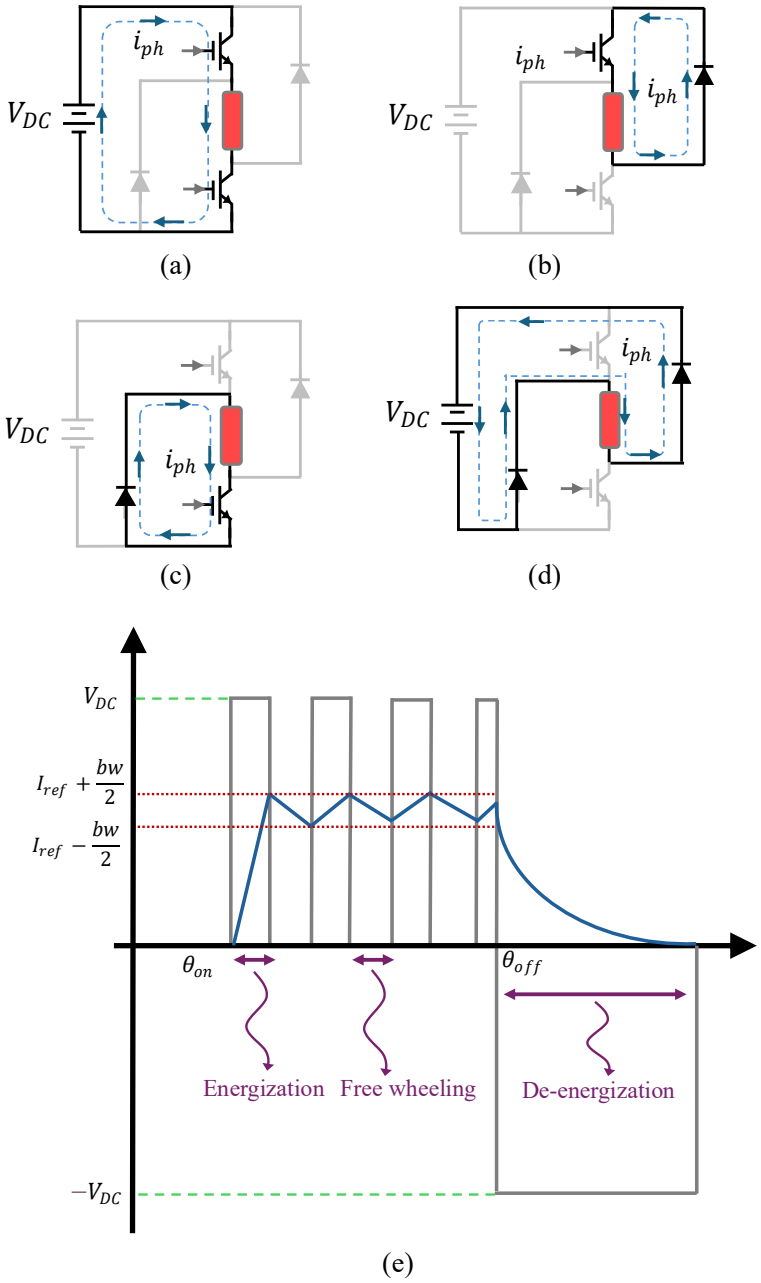


Figure 1.6 Working principle of Asymmetric bridge converter in SRM drive system, (a) energization, (b) freewheeling, (c) freewheeling, (d) de-energization, (e) phase voltage and phase current of an asymmetric bridge converter

### 1.3.3 EMT solver and Verification Method

In this thesis, all proposed models are implemented in the circuit-based EMT simulation engine named EMT-Julia and developed under the Julia environment [6]. EMT-Julia uses the same methodology as EMTP® [7]. Thus, components exhibiting dynamic behavior are discretized using

the trapezoidal integration method. The network matrix system is constructed based on modified augmented nodal analysis (MANA) and solved by the KLU solver.

To validate the results of the proposed EMT models, the studied SRM is modeled by finite element method (FEM) which can accurately model the magnetic behavior of electromagnetic devices such as electric machines [8], [9], transformers [10], [11], inductors [12], actuators [13], and sensors [14], [15] by accounting for complex geometries and nonlinear materials. The FEM model of the studied SRM is implemented in ANSYS Maxwell® software. Despite the high accuracy of FEM, commercial FEM packages lack the power electronics, power system, and control components. The integration of FEM models of electromagnetic devices within their large surrounding systems (such as complex motor drive system of EV or power systems) is possible through co-simulations [16], [17]. Thus, the FEM model of the studied SRM is integrated with the asymmetric bridge converter and controller model in Simplorer® through co-simulation. This model is named CoSim-FEM in this article. To ensure high accuracy and reliability of the FEM-based model as a reference, we used a fine mesh consisting of 12030 triangular elements in the FEM-based model.

All simulations were performed on a 2.5 GHz, Core i7-11850H computer with 64 GB of RAM.

## 1.4 Thesis Outline

This thesis contains the following chapters.

Chapter 1 introduced the outline of thesis, contributions, case study and its working principles, EMT solver, and the method for verification of the proposed models.

Chapter 2 presents the principle of using circuit-based approach for system-level transient modeling of the electromagnetic devices.

Chapter 3 proposes various circuit-based EMT model for the case study machine.

Chapter 4 presents the validation of the proposed circuit-based EMT model of the SRM, provides a comprehensive comparison between the models, and recommends the most suitable model for each transient study.

Chapter 5 integrates the proposed circuit-based EMT models of the machine into an external system representing an EV's power system. The resulting EMT model of this power system is used to study various transient scenarios.

Chapter 6 provides a summary of the thesis, conclusions, and recommendations for future work.

# CHAPTER 2 SYSTEM-LEVEL EMT MODELING OF SRM DRIVE SYSTEM USING CIRCUIT-BASED APPROACH

As mentioned in the introduction, this thesis aims to develop an efficient EMT model of an electrical machine that can be seamlessly integrated into any external power system while accurately accounting for the machine's internal behavior. To this end, using the circuit-based approach for system-level transient modeling of machine and drive system is proposed. In this regard, the principle of using the circuit-based approach for system-level EMT modeling of an EV's power system is demonstrated.

Figure 2.1 shows the schematic diagram of the studied system that represents the EV's power system. As illustrated in the figure, depending on the study scenario, the batteries operate in charging or discharging mode. In this thesis, the discharging mode was considered. In this regard, the charger is not modeled. However, the model can seamlessly be connected to any large external circuit.

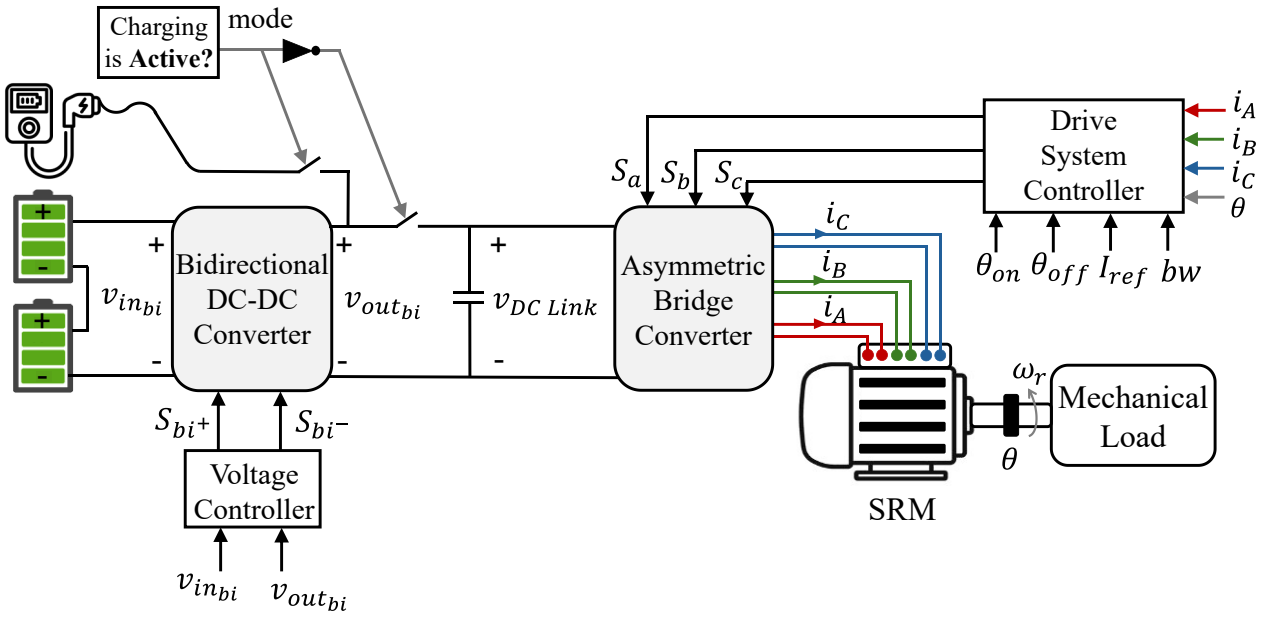


Figure 2.1 Schematic diagram of the studied system consists of batteries, converters, a machine, and their related control

Thus, the concept of the circuit-based EMT model of the machine as well as the circuit-based representation of power electronics devices and battery are presented in this chapter.

## 2.1 Concept of Circuit-Based EMT Model of Electric Machine

Accurate and computationally efficient modeling of electromagnetic devices is a crucial point for their simulation.

The circuit-based representation of electromagnetic devices has been proposed as a promising method for modeling their various physical behaviors, such as magnetic [19], [20], [21], [22], [23], thermal [24], [25], [26], vibration [27], and so on, by using equivalent circuits. The equivalent circuit of the various physical behavior can be seamlessly coupled. In this regard, it is possible to seamlessly integrate the circuit-based model of the electromagnetic devices into a large external power system by implementing them in EMT-type software. This enables system-level transient study of electromagnetic devices in conjunction with their surrounding power system.

Circuit-based approaches offer a flexible trade-off between computational efficiency and modeling accuracy [28], [29]. In the literature, various circuit-based method are presented that can model very detailed behavior of electromagnetic devices [30], [31], [32], [33] to circuit-based models offering a fast solution [34], [35], [36].

Thus, we represent the electrical, magnetic, and mechanical behavior of the machine through interconnected equivalent circuits, as shown in Figure 2.2.

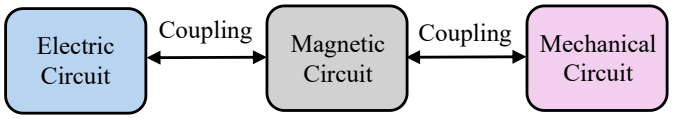


Figure 2.2 Schematic diagram of the machine's EMT modeling through the interconnected equivalent circuit of the electrical, magnetic, and mechanical behaviors

### 2.1.1 Magnetic Circuits

To illustrate the concept of the magnetic circuit, a simple gapped core inductor is shown in Figure 2.3 (a). In this figure, the current in the electric circuit is represented by $i$ while $\varphi$ is the magnetic flux.

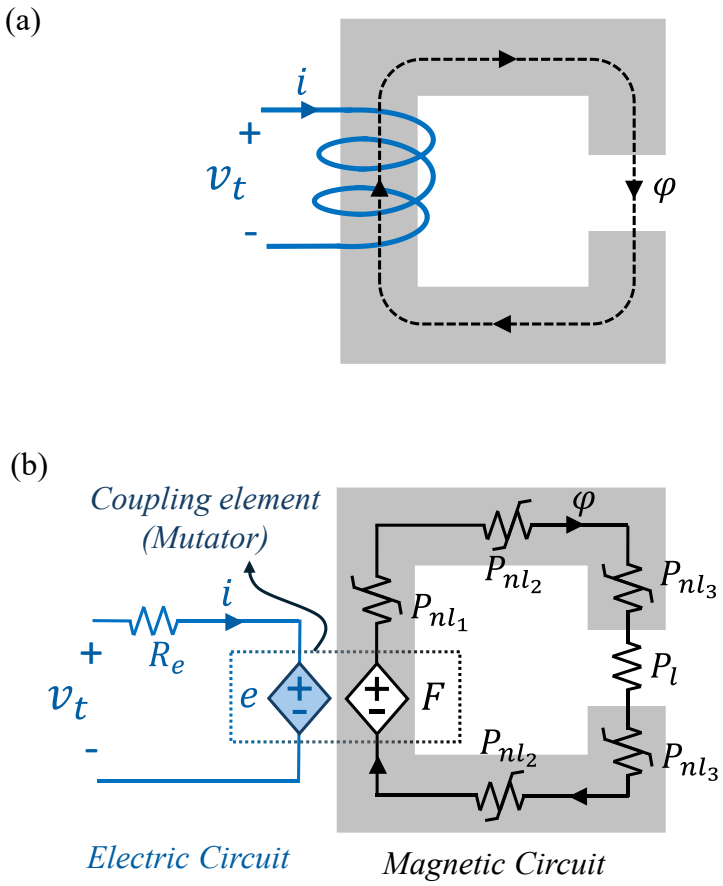


Figure 2.3 Gapped core inductor, (a) cross-sectional view, (b) equivalent permeance network

In this example, we used a simple permeance network to develop the magnetic circuit associated with this device. Thus, the magneto motive force (MMF) drop in various parts of this device is represented in permeance. As shown in Figure 2.3 (b), a linear permeance, named $P_l$, models the MMF drop in the gap, due to the constant permeability of the air. The MMF drop in the ferromagnetic core is represented by nonlinear permeances, named $P_{nl_1}$, $P_{nl_2}$, and $P_{nl_3}$. The current passing through the winding generates the MMF in the magnetic circuit. Thus, the value of the MMF depends on the electric circuit, specifically, on the current passing through it and the number of winding turns.

In the example presented in Figure 2.3, a gapped-core inductor is considered. In this electromagnetic device, there is no rotation. However, in the case of electric machines, the rotation of the rotor should be considered. To account for the mechanical dynamics, it is required to couple

the magnetic and mechanical circuits. The detail regarding the mechanical circuit is presented in the following part of this section.

To model the effect of rotor rotation in the magnetic circuit we can use mesh-based [37], [38], [39] or non-meshed [40], [41] approaches in the airgap.

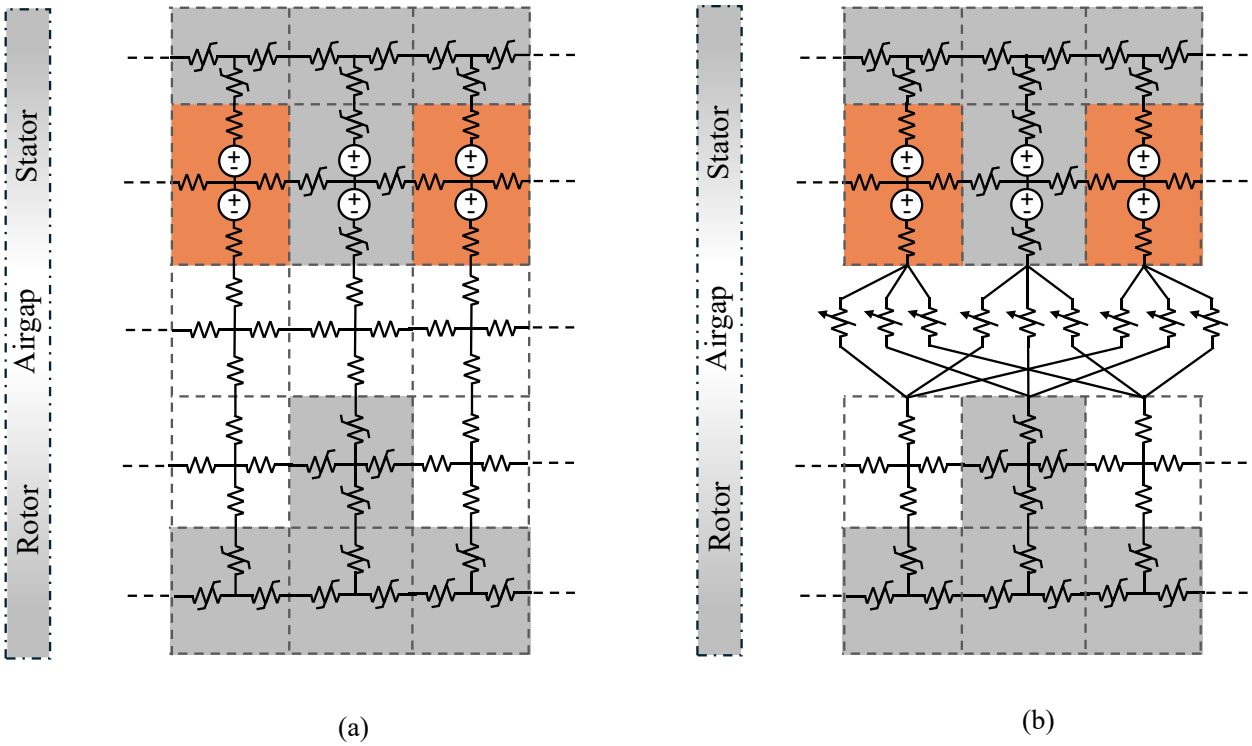


Figure 2.4 Airgap modeling by magnetic circuit, (a) mesh-based approach, (b) non-meshed approach

In the mesh-based approach, the airgap is discretized into smaller mesh elements. Each mesh element consists of linear permeances, as shown in Figure 2.4 (a). Although this method is widely used in the literature for magnetic modeling of various types of machines [42], [43], [44], [45], it comes with limitations for EMT studies. In steady state studies where the machine rotates at a fixed speed, the circuit nodes at the airgap boundary should be reconnected at each time-step. Moreover, in transient studies, dynamic and unpredictable variations of the machine speed necessitate remeshing and regenerating the permeance network at each time-step. Thus, at each time step, we must rebuild the circuit, reformulate the matrix system, and rerun the factorization process. Thus, they lead to a significant computational burden.

In the non-meshed approach, permeance network of the stator and rotor is connected through the variable permeances in the airgap as shown in Figure 2.4 (b). In this approach, the value of airgap permeances depends on the rotor position and it should be calculated at each simulation time step [46], [47], [48]. This allows the circuit topology to remain unchanged during the simulation, making the non-meshed approach suitable for transient studies. Thus, in this thesis, we use non-meshed approach for modeling machine's airgap.

Figure 2.5 (a) shows a part of a machine that includes a stator pole pitch and a rotor pole pitch. Figure 2.5 (b) shows a magnetic circuit associated with this part of the machine. Similar to the gapped-core inductor, the flux path in the ferromagnetic core and machine's slot are respectively modeled by nonlinear and linear permeances. The value of MMF sources depends on the current passing through the electric circuit and winding configuration. The airgap part is modeled by a non-meshed approach. Thus, the permeance network of the stator and rotor is connected through a variable permeance named $P_v$ in Figure 2.5 (b). As shown in this figure, each node on the stator airgap boundary is connected to all nodes on the rotor airgap boundary. For the ease of presentation, we showed only one airgap variable permeance in Figure 2.5 (b).

Therefore, the magnetic circuit of the electric machine is constructed using linear, nonlinear, and variable permeances, as well as MMF sources. Moreover, the value of electromagnetic torque is calculated by the co-energy method in this thesis. Also, the study domain can be either the full geometry of the machine or a quarter of the machine's geometry. The description regarding each element within the magnetic circuit of the machine is presented in the following section of this chapter.

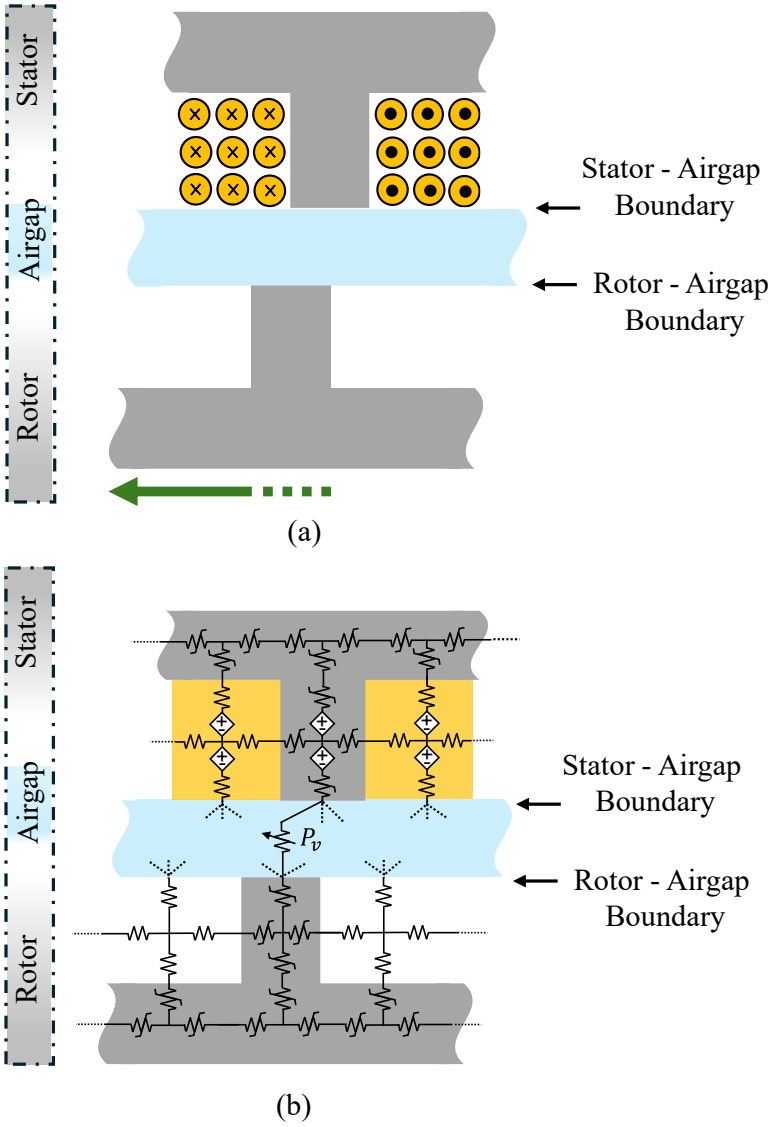


Figure 2.5 Simple magnetic circuit of the electric machine, (a) a part of the machine with a concentric winding, (b) equivalent permeance networks

### 2.1.1.1 Linear Permeances

As noted, linear permeances are used to model the flux path in parts of electromagnetic devices that exhibit linear magnetic behavior, such as air. The value of linear permeances can be calculated as [49]

$$P = \mu_r \mu_0 \frac{S_{lin}}{l_{lin}} \tag{2.1}$$

where $P$ is the value of the linear permeance, $l_{lin}$ and $S_{lin}$ respectively express the mean length and cross-section of the permeance, $\mu_0$ is the air permeability, and $\mu_r$ is the relative permeability of the material related to the permeance.

Based on the geometry of the case study12/8 SRM shown in Figure 1.3, the permeances in its magnetic circuit include both rectangular and cylindrical shapes. The permeances with rectangular shapes relate to the rotor and stator teeth, whereas those associated with the slots and yokes of the rotor and stator have cylindrical shapes. These rectangular and cylindrical shape permeances represent flux paths in the radial and orthoradial directions. Thus, the calculation of permeance values for rectangular and cylindrical shapes in radial and orthoradial directions is presented in this section.

Figure 2.6 (a) and Figure 2.6 (b) shows the permeances with rectangular shapes representing the flux path in radial and orthoradial directions, respectively. In these figures, $L_{stk}$ is the stack length of the electromagnetic device.

In Figure 2.6 (a), the rectangular permeance representing the flux path in the radial direction. This permeance is denoted by $P_{rct_r}$ and its value can be calculated as

$$P_{rct_r} = \mu_0 \mu_r L_{stk} \frac{W}{r_o - r_i} \tag{2.2}$$

Also, the rectangular permeance representing the flux path in the orthoradial direction is shown in Figure 2.6 (b). The value of this permeance $P_{rct_o}$ is expressed as

$$P_{rct_o} = \mu_0 \mu_r L_{stk} \frac{r_o - r_i}{W} \tag{2.3}$$

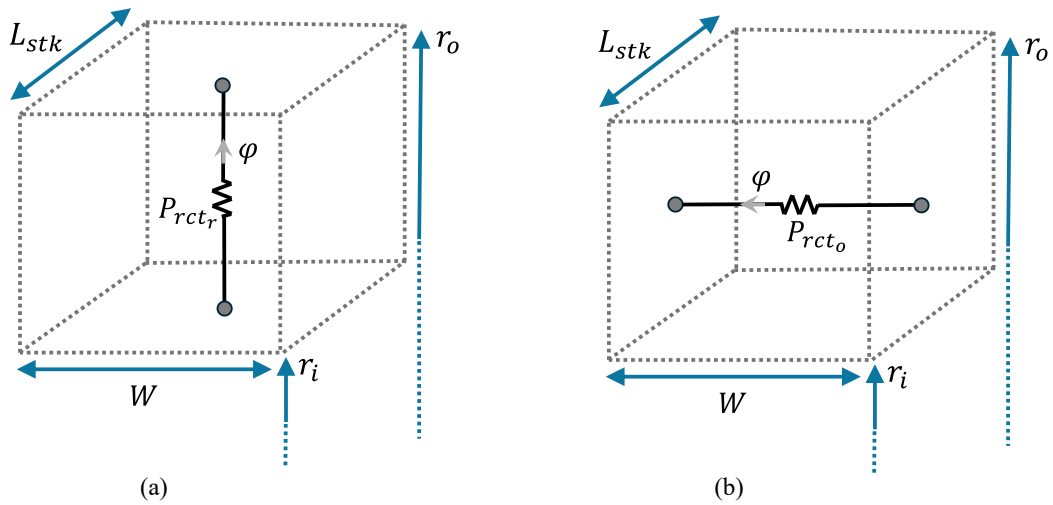


Figure 2.6 Rectangular permeance representing flux in (a) radial direction, (b) orthoradial direction

The permeance with the cylindrical shape is shown in Figure 2.7. As shown in Figure 2.7 (a), the cylindrical permeance representing the flux path in the radial direction can be expressed as

$$P_{cyl_r} = \mu_0 \mu_r L_{stk} \frac{\theta_P}{\ln\left(\frac{r_o}{r_i}\right)} \tag{2.4}$$

where $P_{cyl_r}$ is the value of a cylindrical shape permeance in the radial direction, and $\theta_P$ is the angle associated with this permeance.

Moreover, the value of the cylindrical permeance in the orthoradial direction, named as $P_{cyl_o}$ in Figure 2.7 (b), can be calculated as

$$P_{cyl_o} = \mu_0 \mu_r L_{stk} \frac{\ln\left(\frac{r_o}{r_i}\right)}{\theta_P} \tag{2.5}$$

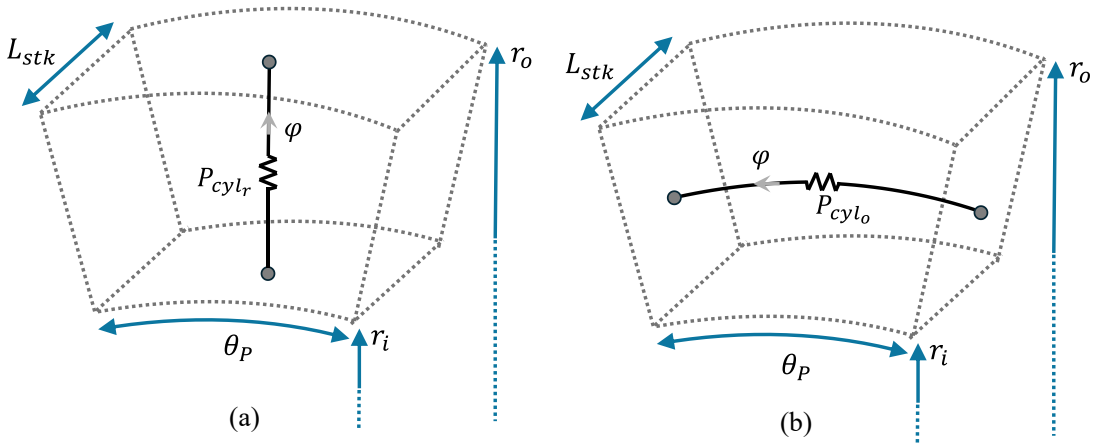


Figure 2.7 Cylindrical permeance representing flux in (a) radial direction, (b) orthoradial direction

### 2.1.1.2 Nonlinear Permeances

As shown in Figure 2.3 (b) and Figure 2.5 (b), the nonlinear characteristic of the ferromagnetic core is modeled by the nonlinear permeances in the magnetic circuit. Thus, in the magnetic circuit associated with the case study SRM shown in Figure 1.3, nonlinear permeance should be employed to account for the nonlinear magnetic behavior of the ferromagnetic core in the stator and rotor yokes and teeth.

To consider the nonlinear magnetic characteristics of the ferromagnetic core, an iterative technique like Newton's method can be employed. For each nonlinear permeance in the magnetic circuit, a piecewise approach is employed to represent the B-H characteristic. Figure 2.8 shows the B-H curve of a ferromagnetic core represented by a piecewise linear function with three segments.

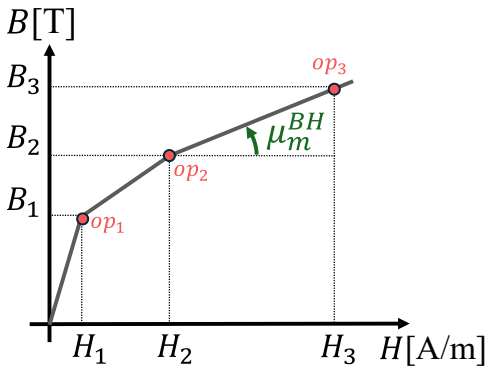


Figure 2.8 B-H Curve of ferromagnetic core represented by the piecewise linear function

To derive the equivalent circuit of the nonlinear permeance, we assume an arbitrary operating point $op_m$ located between two consecutive sampling points ($op_n$, $op_{n+1}$). The magnetic flux density of this point can be calculated as [19]:

$$B_m = \frac{B_{n+1} - B_n}{H_{n+1} - H_n}\left(H_m - H_n\right) + B_n \tag{2.6}$$

where $B_n$ and $B_{n+1}$ are respectively the magnetic flux density of consecutive sampling points $op_n$ and $op_{n+1}$, $H_n$ and $H_{n+1}$ represents the magnetic field strength of the sampling points $op_n$ and $op_{n+1}$, respectively.

If we multiply both side of equation (2.6) with the cross-section of the nonlinear permeance, we have

$$B_m S_{nl} = \frac{\mu_m^{BH} S_{nl}}{l_{nl}} H_m l_{nl} + \left(B_n - \mu_m^{BH} H_n\right) S_{nl} \tag{2.7}$$

where $l_{nl}$ is the length of the flux path modeled by the nonlinear permeance, $S_{nl}$ represents the cross-section of the nonlinear permeance, $\mu_m^{BH}$ is the magnetic permeability in $m^{th}$ segment. We can write the equation (2.7) to obtain its equivalent circuit representation as:

$$\varphi_m = P_m^{BH} \Delta\varepsilon_m + \varphi_m^{BH} \tag{2.8}$$

where $\Delta\varepsilon_m$ is the magnetic potential drop due to $H_m$, $P_m^{BH}$ and $\varphi_m^{BH}$ are the Norton equivalent circuit values at the operating point $op_m$ on the $m^{th}$ segment. The saturation of the ferromagnetic core will be modeled by adding a flux source in parallel with the permeance, while the value of the flux source $\varphi_m^{BH}$ and permeance $P_m^{BH}$ depend on the system's solution.as shown in Figure 2.9.

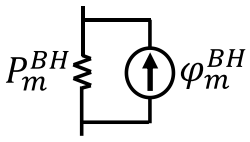


Figure 2.9 Norton companion model of nonlinear permeance

### 2.1.1.3 Variable Permeances

To account for the machine's rotation, a non-meshed approached is used in the magnetic circuit of the studied 12/8 SRM. As shown in Figure 2.10, variable permeances connect each node of the stator-airgap boundary to all nodes on the rotor-airgap boundary. The value of the airgap permeances depends on the geometrical specification of the machine as well as the rotor position. Thus, the value of these variable permeances changes according to the rotor position at each simulation time-step [50], [51]. Therefore, the circuit topology remains unchanged during the simulation process.

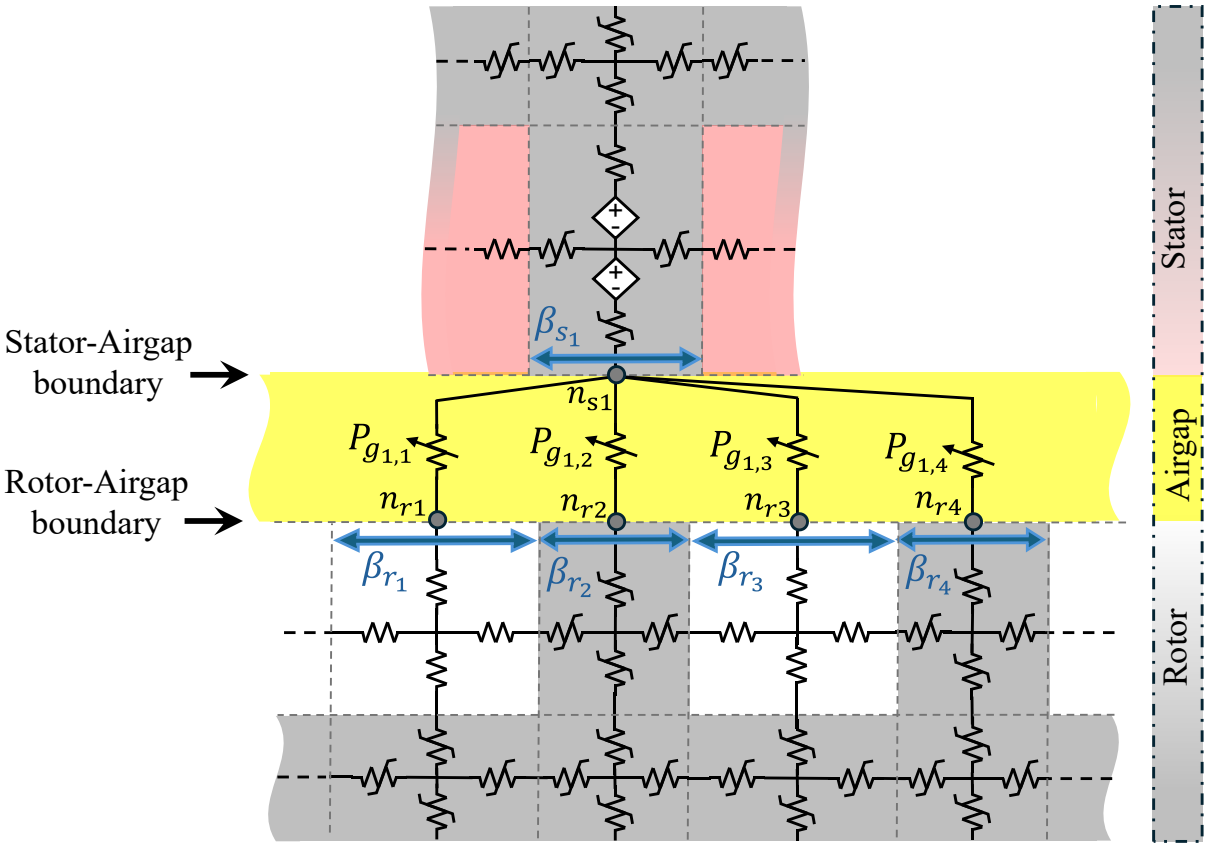


Figure 2.10 Airgap variable permeances connecting the permeance network of the stator and rotor

As mentioned the value of the airgap permeances depends on the relative position between the stator and rotor. For instance, the airgap permeance connecting the node $n_{s1}$ at the stator-airgap boundary to the node $n_{r2}$ at the rotor-airgap boundary is highly conductive, while the value of the airgap permeance decreases progressively as the teeth move apart and are in partially or non-

overlapping positions (like the relative position between $n_{s1}$ and $n_{r1}$, $n_{r3}$, $n_{r4}$ in Figure 2.10). In this regard, correct estimation of the airgap permeance values in various rotor positions is crucial for reaching an acceptable accuracy of the SRM's magnetic model.

Two methods can be used to calculate the airgap permeance values based on the rotor position. In the following parts of this section, these methods are presented.

**1) Calculation of Airgap Permeance Values by Tooth Contour Method (TCM)**

The first method is named the tooth contour method (TCM). Figure 2.11 shows the implementation of TCM. TCM calculates the airgap permeance value based on the magnetic potential difference between the edge of a stator tooth and the other teeth. In Figure 2.11, we calculate the value of the airgap permeance connecting stator tooth number 2 to rotor tooth number 1 at various rotor positions as [52]:

$$P_{g_{i,j}}(\theta) = \frac{\varphi_j(\theta)}{\Delta\varepsilon_{i,j}} \tag{2.9}$$

where $P_{g_{i,j}}$ is the value of the airgap permeance connecting the tooth $i$ of the stator to the tooth $j$ of the rotor, $\theta$ is the rotor position, $\varphi_j$ represents the flux passing through the tooth $j$ of the rotor.

In the literature, the TCM is implemented using FEM. In this thesis, we use FEM and also propose a circuit-based implementation of the TCM. In this regard, Figure 2.12 shows the studied domain, boundary condition, and implementation of the circuit-based representation of TCM. As shown in this figure, the mesh-based permeance network is used to develop the magnetic circuit of the TCM. Each mesh element consists of four permeances, two in the radial direction $P_r$ and two in the orthoradial direction $P_o$.

Figure 2.13 shows the airgap permeance values calculated by FEM-based and circuit-based TCM for an arbitrary stator and rotor teeth. As shown, the circuit-based TCM has good accuracy. The circuit-based TCM can be implemented in EMT-type software and eliminates using FEM for calculating the airgap permeance values.

Although TCM is an accurate method, it requires interpolation between precalculated values at each time-step in time domain simulations.

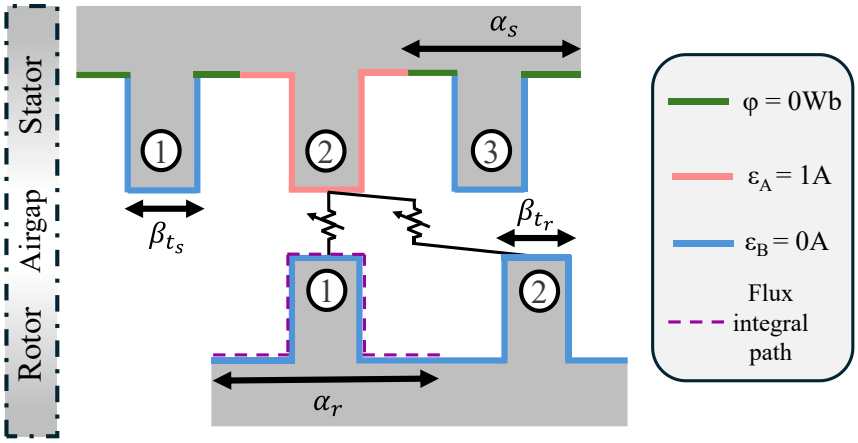


Figure 2.11 TCM implementation

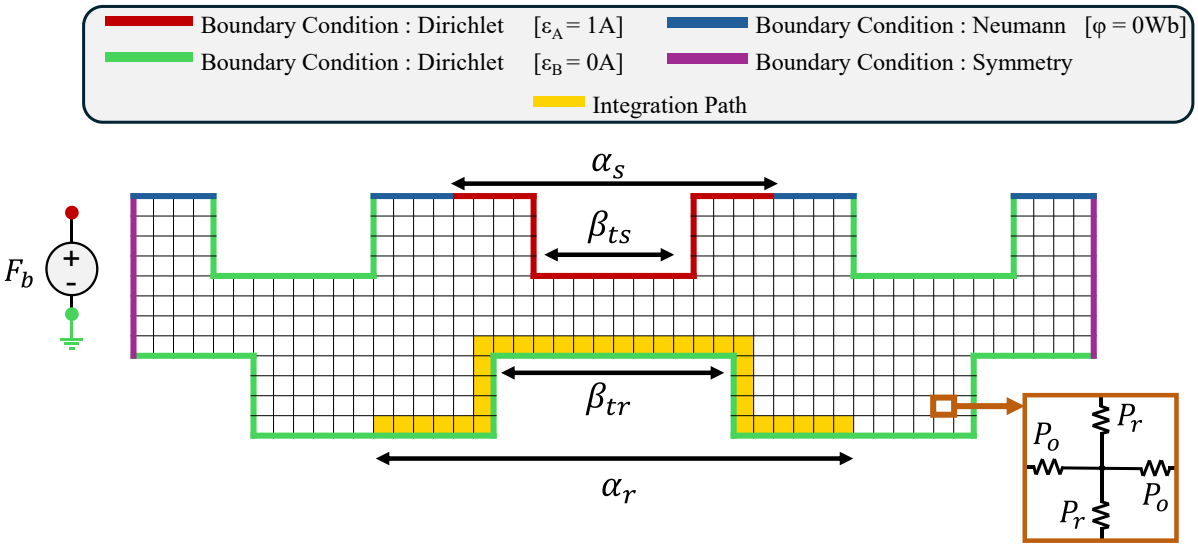


Figure 2.12 Circuit-based representation of TCM

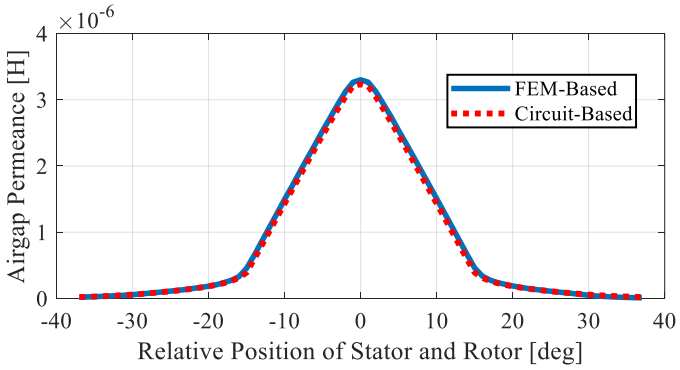


Figure 2.13 Airgap permeance value calculated by FEM-based and circuit-based TCM

**2) Calculation of Airgap Permeance Values by Analytical Functions**

To tackle the drawback of TCM, the calculation of airgap permeance by analytical functions is proposed.

In the literature, various analytical functions are proposed to calculate the value of the airgap permeance. In this section, we analyze various analytical functions available in the literature and formulate a suitable analytical function for the magnetic circuit of the studied SRM. In this airgap function analysis, we use the TCM as the reference.

We calculated the airgap permeance for an arbitrary rotor tooth angle $\beta_{t_r}$ of 15 degrees and a stator tooth angle $\beta_{t_s}$ of 17 degrees by cosine [49], [53] exponential [51], [4], [54], linear functions [55], [56], [57], and bell-shaped [52], [58] functions and compared their results with the values obtained from the TCM calculation, as presented in Figure 2.14. In this figure, the x-axis represents the relative position between the analyzed stator and rotor teeth. On the x-axis, 0° corresponds to the aligned position of the rotor and stator teeth. As shown in this figure, the values obtained from all analytical functions deviate more from the TCM calculated values as the rotor moves out of alignment with the stator tooth, particularly in the semi-aligned and unaligned positions. This inaccuracy is due to the large slot openings of SRMs, as shown in Figure 2.15. The large slot opening is a significant difference of SRMs compared to induction machines, synchronous machines, and permanent magnet synchronous machines. The large slot opening of SRM causes a high fringing and leakage flux, particularly in the semi-unaligned and unaligned relative position between stator and rotor teeth, as shown in Figure 2.16 (a) and Figure 2.16 (b).

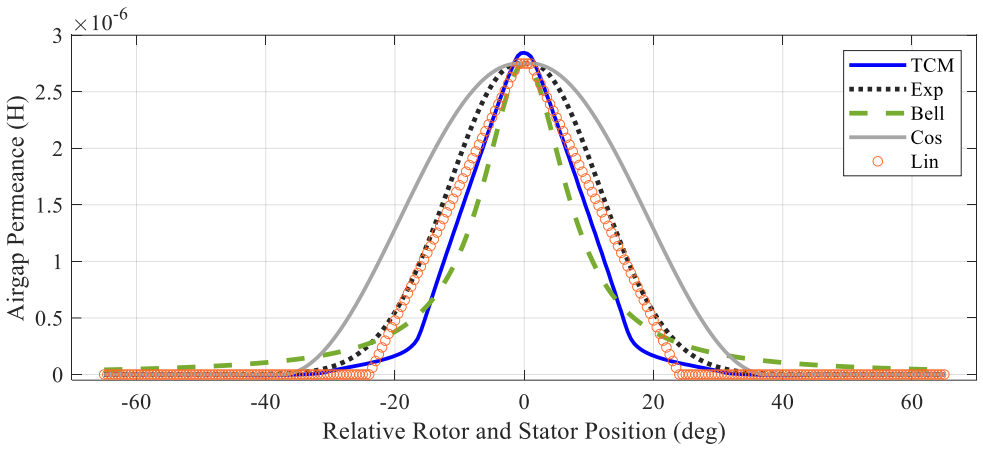


Figure 2.14 Airgap permeance values calculated by TCM and various analytical functions

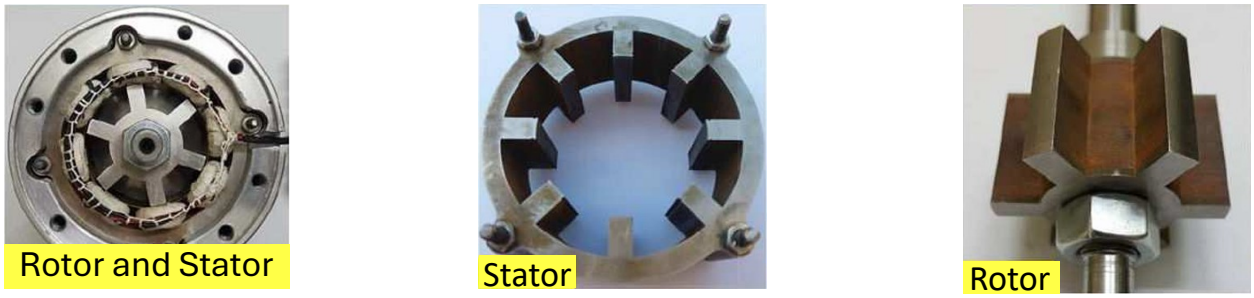


(a) (b) (c)

Figure 2.15 A prototyped SRM showing its large slot openings in rotor and stator, (a) assembled rotor and stator, (b) stator, (c) rotor [59]

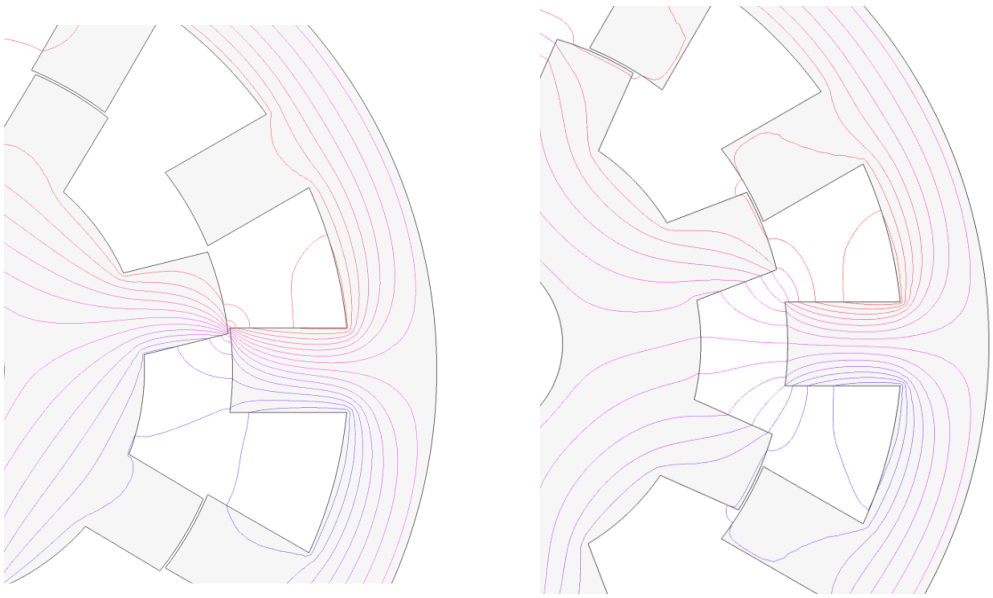

(a) (b)

Figure 2.16 Flux lines between stator and rotor in various rotor positions, (a) semi-unaligned, (b) unaligned

In the following, we aim to improve the accuracy of the analytical function. Among these analytical functions, the bell-shaped function includes certain undefined parameters that can be fitted to match a specific combination of stator and rotor tooth angles. In the literature, optimization processes have been used to fit these undefined parameters. However, using an optimization algorithm in the pre-processing of the simulation is not in the interest of this research.

Among other analytical functions, we selected the exponential function for its simplicity and proven adaptability and accuracy for other machine types [4]. Thus, the analytical function that calculates the value of the airgap variable permeance connecting the node $i$ on the stator-airgap boundary to the node $j$ on the rotor-airgap boundary can be expressed as:

$$P_{g_{i,j}} = \begin{cases} P_{g_{m_{i,j}}} & \theta_{i,j} \le \beta_{m_{i,j}} \\ P_{g_{m_{i,j}}} \exp\left( -\left[ \dfrac{\theta_{i,j} - \beta_{m_{i,j}}}{\beta_{Z_{i,j}} - \beta_{m_{i,j}}} \right]^2 \right) & \theta_{i,j} > \beta_{m_{i,j}} \end{cases} \tag{2.10}$$

where $P_{g_{m_{i,j}}}$ is the maximum value of the airgap permeance between node $i$ on the stator-airgap boundary to the node $j$ on the rotor-airgap boundary. This value can be calculated based on the formula of the cylindrical permeance in the orthoradial direction. Also, $\theta_{i,j}$ is the relative position between the node $i$ on the stator-airgap boundary and the node $j$ on the rotor-airgap boundary. This parameter can be calculated as

$$\theta_{i,j} = \theta + \sigma_{i,j} \tag{2.11}$$

where $\theta$ is the rotor position, and $\sigma_{i,j}$ is the initial relative position between the node $i$ on the stator-airgap boundary and the node $j$ on the rotor-airgap boundary. For instance, the initial relative position between the nodes at the center of stator tooth 1 and rotor tooth 2 is 45°, as shown Figure 2.17 ($\sigma_{1,2} = 45^{\circ}$ in Figure 2.17).

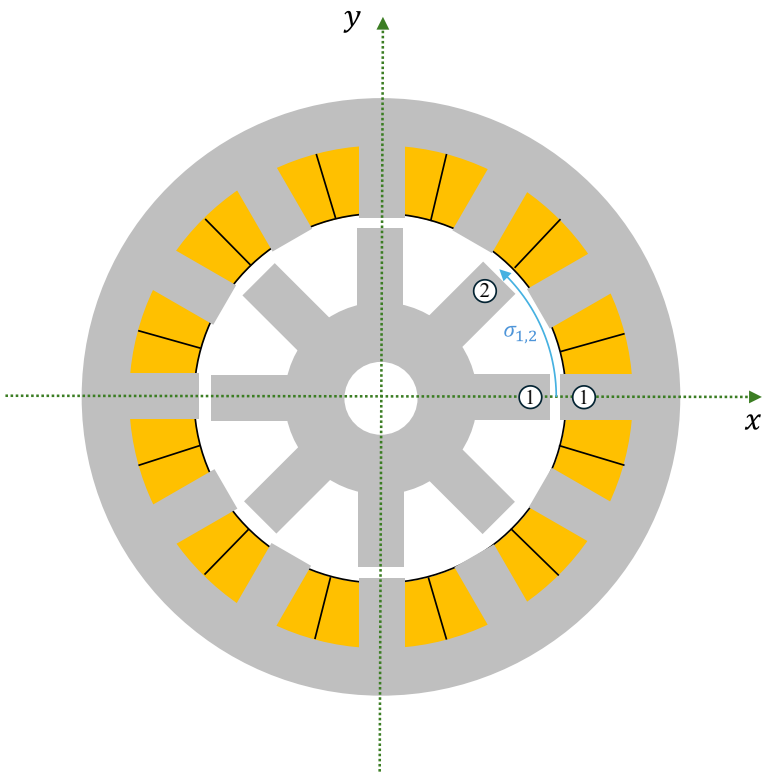


Figure 2.17 Relative position between the stator and rotor teeth

Moreover, this analytical function includes two parameters, $\beta_m$ and $\beta_z$, whose values are determined by the rotor and stator tooth angles. The parameter $\beta_m$ accounts for the positions corresponding to the overlap between the stator and rotor teeth as

$$\beta_m = \frac{\left|\beta_{t_r} - \beta_{t_s}\right|}{2} \tag{2.12}$$

where $\beta_{t_r}$ and $\beta_{t_s}$ are the rotor and stator tooth angles, respectively.

Also, $\beta_z$ models the opening shape of the exponential function as

$$\beta_Z = k_c \frac{\left|\beta_{t_r} + \beta_{t_s}\right|}{2} \tag{2.13}$$

To see the effect of $\beta_z$ on the shape of the exponential function, we changed the factor $k_c$ from 1 to 0.25. Figure 2.18 shows the effect of $\beta_z$ on the shape of the exponential function.

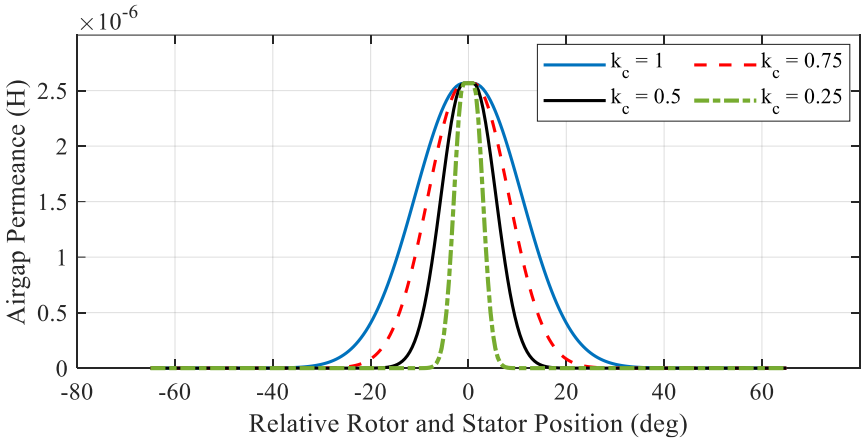


Figure 2.18 Effect of $\beta_Z$ on the airgap permeance values

After many attempts and tests, we modified the calculation of this parameter as:

$$\beta_Z = \frac{\alpha_s}{\alpha_r} \frac{\left|\beta_{t_r} + \beta_{t_s}\right|}{2} \tag{2.14}$$

where $\alpha_s$ and $\alpha_r$ are the stator and rotor pole pitch, respectively.

Figure 2.19 presents the airgap permeance values calculated by the proposed exponential function (equations (2.10) to (2.14)) and the TCM. In this figure, the exponential function is named as Exp. As can be seen, the exponential function demonstrates good accuracy in approximating the airgap permeance values, matching those calculated by TCM.

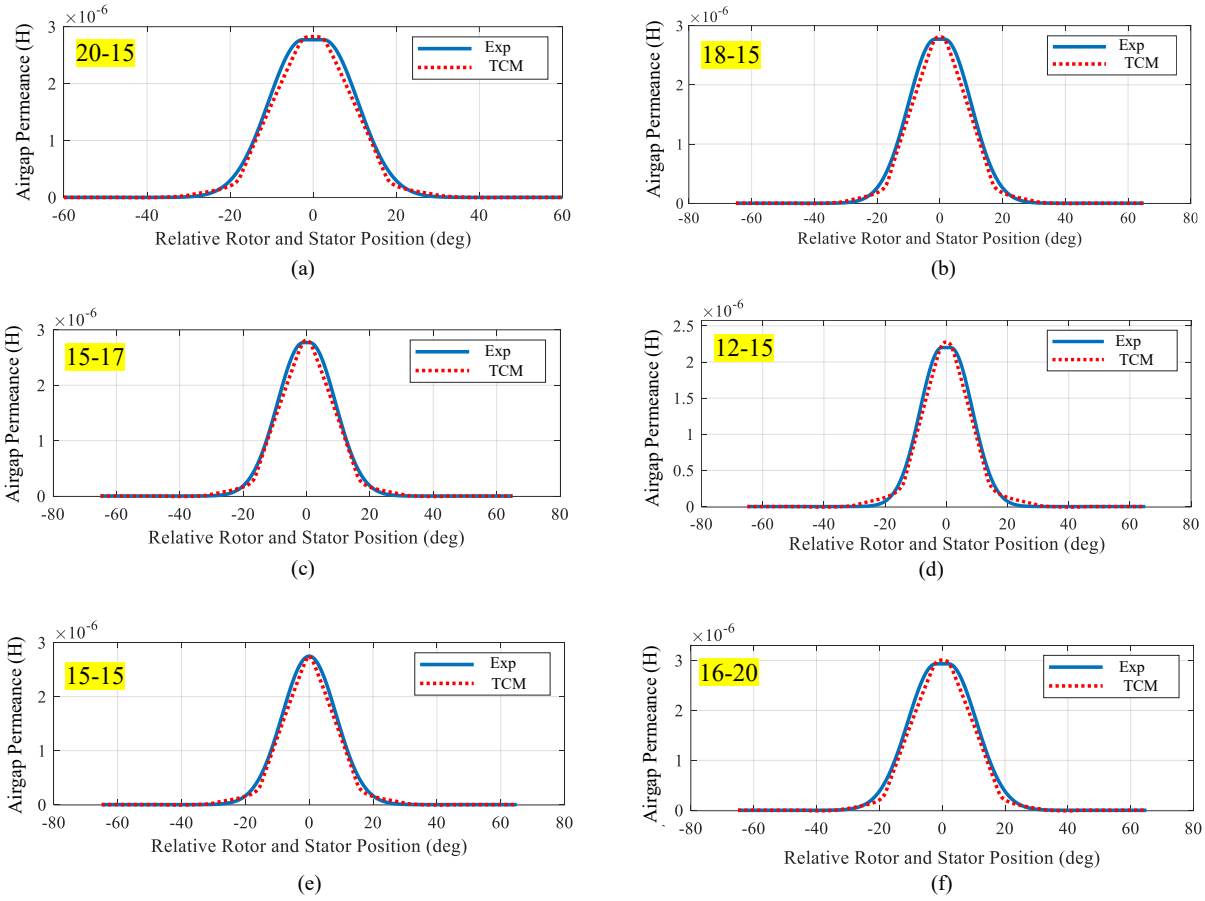


Figure 2.19 Airgap permeance calculated by the TCM and exponential function for various rotor and stator teeth angles (a) $\beta_{t_r} = 20^\circ$ and $\beta_{t_s} = 15^\circ$, (b) $\beta_{t_r} = 18^\circ$ and $\beta_{t_s} = 15^\circ$, (c) $\beta_{t_r} = 15^\circ$ and $\beta_{t_s} = 17^\circ$, (d) $\beta_{t_r} = 12^\circ$ and $\beta_{t_s} = 15^\circ$, (e) $\beta_{t_r} = 15^\circ$ and $\beta_{t_s} = 15^\circ$, (f) $\beta_{t_r} = 16^\circ$ and $\beta_{t_s} = 20^\circ$

### 2.1.1.4 Using Symmetry in Magnetic Circuits

Computational time is an important factor in EMT simulations. Thus, researchers and engineers are making many efforts to accelerate the EMT simulation process. In the context of EMT modeling of electromagnetic devices by using magnetic circuits, reducing the study domain is an effective approach to accelerate the EMT simulation process.

In the case of electric machines, the study domain can be either the full geometry of the electric machine or a quarter of it. The full geometry should be modeled when simulating transient phenomena occurring inside the machine, such as a short circuit in the windings. However, to analyze the transient phenomena happening outside of the machine, the domain can be reduced to a quarter of the electric machine's geometry to speed up the simulation.

To reduce the study domain to a quarter of the electric machine's geometry, symmetry must be utilized. Based on the machine's geometry and winding patterns, the boundary condition of symmetry can be periodic or antiperiodic. As an example, various winding patterns for the 12/8 SRM are illustrated in Figure 2.20. To model a quarter of the 12/8 SRM with the winding pattern in Figure 2.20 (a), periodic boundary conditions should be applied, whereas antiperiodic boundary conditions are required for the winding pattern shown in Figure 2.20 (b).

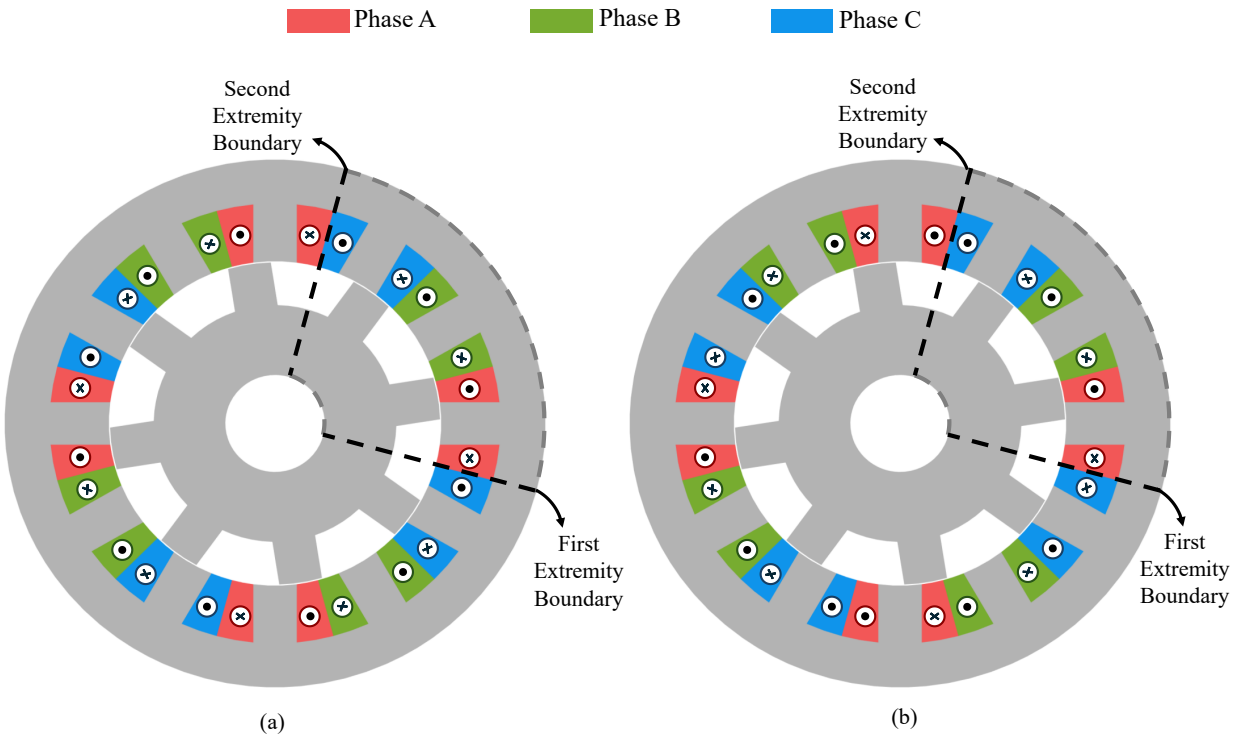


Figure 2.20 12/8 SRM with the different winding patterns requiring (a) periodic and (b) antiperiodic boundary conditions

Figure 2.21 (a) shows a magnetic circuit within a quarter of the studied SRM, where the symmetry is applied. Independent of the magnetic circuit configuration within a quarter of the electric

machine, the nodes on the first extremity boundary should be connected to the nodes on the second extremity boundary in a way that satisfies the following equations [52]:

$$F'_{bound} = \pm F_{bound} \tag{2.15}$$

$$\varphi'_{bound} = \pm \varphi_{bound} \tag{2.16}$$

where $F_{bound}$ is the magnetic potential of the nodes on the first boundary, $F'_{bound}$ represents the magnetic potential of the nodes on the second boundary, $\varphi_{bound}$ is the flux passing through the nodes on the first boundary, and $\varphi'_{bound}$ is the flux passing through the nodes on the second boundary. The positive sign must be used for periodic boundary conditions, while the negative sign must be used for antiperiodic boundary conditions. Independent of the magnetic circuit. The equations (2.15) and (2.16) can be simulated by an ideal transformer as shown in Figure 2.21 (b). The turn ratio of the ideal transformer (indicated as $T$ in Figure 2.21 (b)) is 1 for periodic and -1 for antiperiodic boundary conditions.

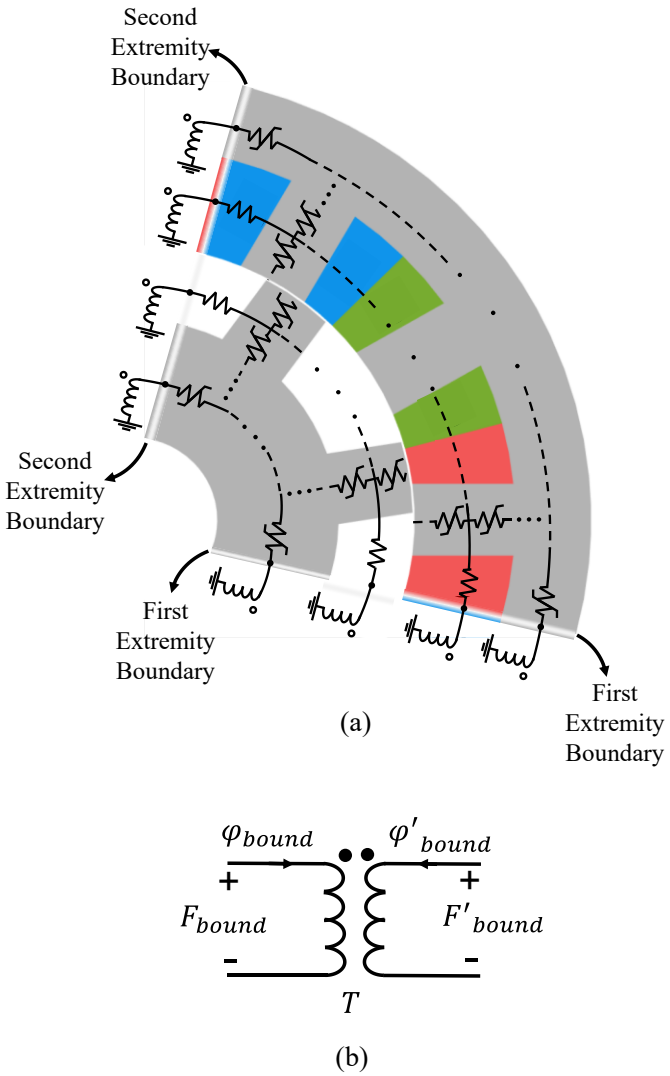


Figure 2.21 Implementation of the boundary condition due to the symmetry by using ideal transformers

### 2.1.2 Coupling of Magnetic and Electric Circuit

As mentioned in the previous sections, the value of MMF in the magnetic circuit depends on the current passing through the electric circuit and the number of winding turns. To seamlessly couple magnetic and electric circuits, the mutator is used. Figure 2.22 shows a mutator with its electrical terminals labeled as $k_e$ and $m_e$ while $k_m$ and $m_m$ respectively represent the positive and negative pins in the magnetic side. In this figure, the electric and magnetic sides of the mutator are in blue and black, respectively.

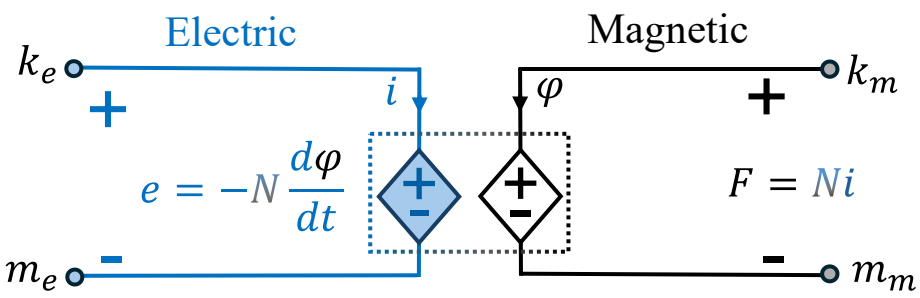


Figure 2.22 Mutator

According to Faraday's law, the mutator enables the seamless coupling between the electrical and magnetic circuits by transferring current into the magnetic circuit as a source of MMF, and by converting the magnetic flux into the electrical circuit as an electromotive force (EMF) source. The transformation ratio of this mutator is denoted as $N$. The MMF and EMF of the mutator can be calculated as [21], [60], [61][22]

$$F = Ni \tag{2.17}$$

$$e = -N\frac{d\varphi}{dt} \tag{2.18}$$

where $F$ represents the MMF of the mutator, $e$ is the EMF of the mutator, $i$ is the current in the electric circuit, $\varphi$ is the flux passing through the magnetic circuit, the gain of the mutator is represented by $N$.

In the mesh-based permeance network, the coil region is subdivided into smaller mesh elements. Each element associated with the coil consists of mutators. To have a more detailed description, the coupled magnetic and electric circuit within a pole pitch of the stator with a concentrated coil wound over the stator tooth is shown in Figure 2.23 (a). In this figure, the magnetic circuit is in black while the electric circuit is in blue. In this figure, $R_{coil}$ represents the coil resistance, and the induced EMF of the coil is represented by $e_{coil}$.

As shown in Figure 2.23 (a), the electric and magnetic circuits are connected through mutators. The induced EMF of the coil is equal to the sum of the EMF of each mutator as [62]

$$e_{coil} = \xi \sum_{x=1}^{n_m} e_x \tag{2.19}$$

where $e_{coil}$ is the induced EMF of the coil, $e_x$ is the EMF of each mutator, $n_m$ is the total number of mutators within a coil ($n_m = 6$ in Figure 2.23 (a)), and $\xi$ is the symmetry factor ($\xi = 4$ in case of modeling a quarter of machine and $\xi = 2$ in case of modeling half of machine).

The gain of mutators in each mesh element can be calculated by applying Ampere's law. Figure 2.23 (b) illustrates the gain of the mutators over the stator spatial position $\delta$ within a stator pole pitch. In this figure, $N_t$ is the total number of turns in the coil [64] [63] [64].

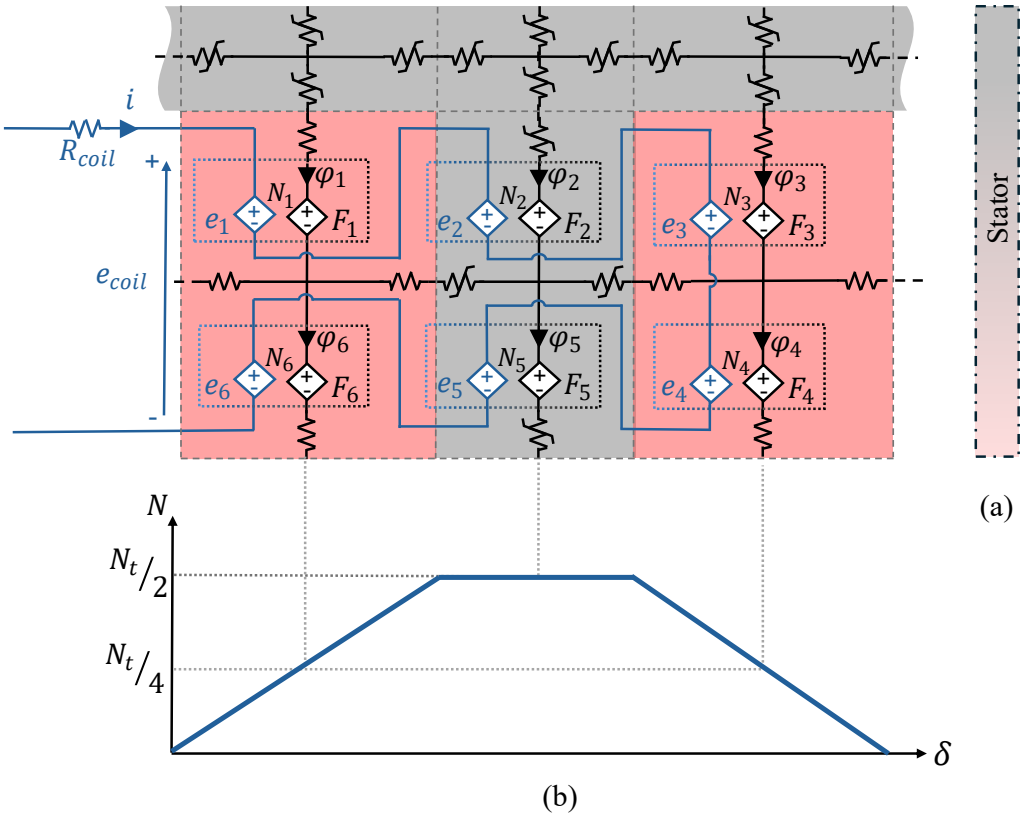


Figure 2.23 Description of mutators and their connection, (a) coupled magnetic and electric circuits within a stator pole pitch, and (b) mutator gain over stator spatial position

### 2.1.3 Mechanical Equivalent Circuit

As previously mentioned, the proposed EMT model of the machine consists of the coupled magnetic, electric, and mechanical circuits. Recall that Figure 2.2 shows the diagram of the machine's EMT model, which consists of the coupled electric, magnetic, and mechanical circuits.

In this section, the derivation of the equivalent circuit representation of the machine's mechanical equations is presented.

The mechanical equations of the machine are written as [65]

$$T_e - T_L = J_m \frac{d\omega_r}{dt} + D_m \omega_r \tag{2.20}$$

$$\omega_r = \frac{d\theta}{dt} \tag{2.21}$$

where $T_e$ is the electromagnetic torque, $T_L$ is the load torque, $J_m$ represents the moment of inertia, $D_m$ is the damping factor, and the machine speed is expressed as $\omega_r$.

The value of the electromagnetic torque at each simulation time-step can be calculated based on the co-energy method as [66]

$$T_e = \xi \sum_{n=1}^{n_g} \frac{dP_{g_n}}{d\theta} \frac{F_{P_{g_n}}{}^2}{2} \tag{2.22}$$

where $n_g$ is the total number of airgap variable permeances, $F_{P_g}$ is the MMF of each airgap permeance, and $\xi$ is the symmetry factor. In this equation, $P_g$ is the function that calculates the value of the airgap permeances at each simulation time step.

In the circuit-based representation, the moment of inertia $J_m$ and damping factor $D_m$ can be modeled by an inductor and a resistor, respectively. Also, we can conclude that the machine's speed can be served as the current passing through the inductor and resistor that representing the moment of inertia $J_m$ and damping factor $D_m$. Additionally, equation (2.21) is representing a capacitor with the capacitance of 1 F where the rotor position $\theta$ and $\omega_r$ respectively serve as the voltage and current of this capacitor. To connect this capacitor with the equivalent circuit representing equation (2.20), we can use a current-controlled current source with the gain of 1.

As presented in equation (2.22), the value of the electromagnetic torque $T_e$ depends on the MMF of the airgap's variable permeances and the rotor position. These MMFs and rotor position are the node voltages in the magnetic and mechanical circuits, respectively. In this context, a voltage-controlled voltage source can be used to implement equation (2.22) using the circuit-based

approach. Additionally, the load torque can be modeled using a controlled voltage source, where the control signal depends on the type of load. In this regard, the circuit-based representation of the mechanical equations is shown in Figure 2.24. In this figure, MMFs of airgap permeances are depicted as $F_{P_{g1}}$ to $F_{P_{gng}}$ and a speed-dependent load torque is assumed [51].

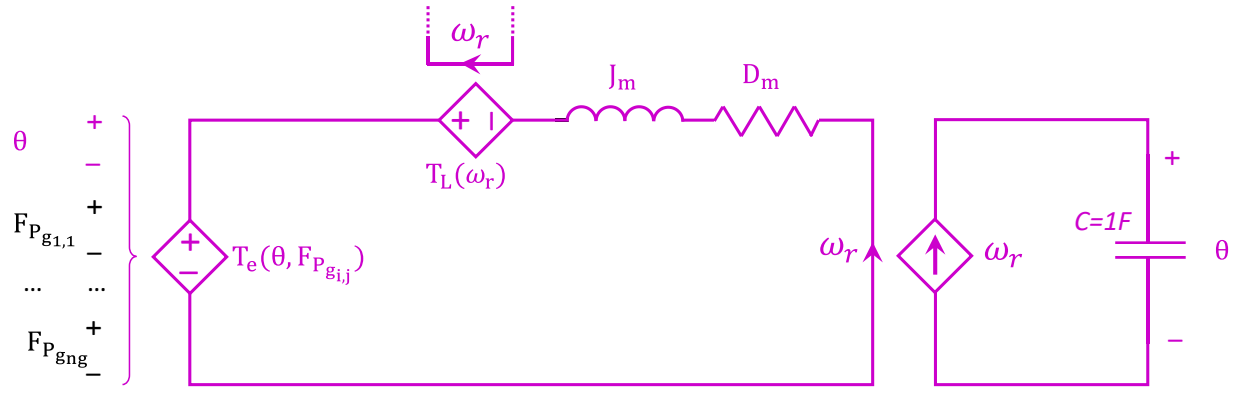


Figure 2.24 Equivalent circuit of the mechanical equations

## 2.2 Circuit-Based EMT model of Power Electronics Components

As shown in figure Figure 2.1, the power system of EV includes batteries and power electronics converters. The batteries are connected to the DC link through a bidirectional DC-DC converter. Figure 2.25 shows the schematic diagram of a bidirectional DC-DC converter.

An asymmetric bridge converter feeds and controls the SRM. The schematic diagram of the asymmetric bridge converter is shown in Figure 2.26.

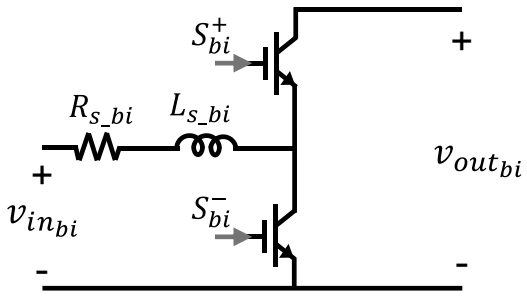


Figure 2.25 Schematic diagram of the bidirectional DC-DC converter

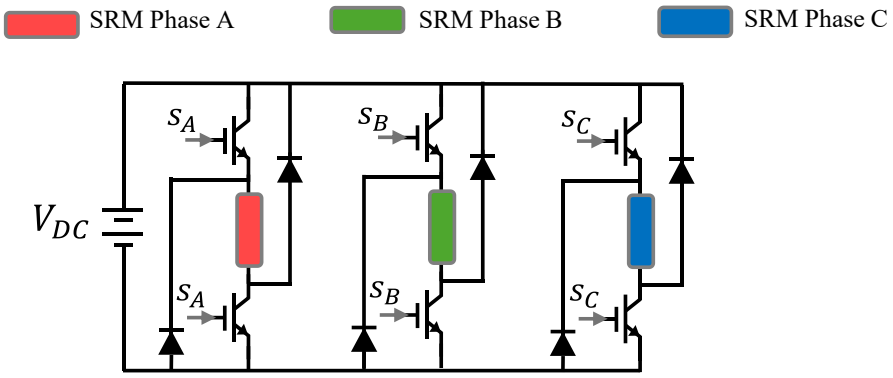


Figure 2.26 Schematic diagram of the asymmetric bridge converter

As shown in Figure 2.25 and Figure 2.26, the bidirectional DC-DC converter and asymmetric bridge converter consist of IGBTs and diodes.

### 2.2.1 Diode

To model the nonlinear I-V characteristics of the diode, a nonlinear resistance can be used. Figure 2.27 (a) shows the schematic diagram of the diode while the nonlinear resistance representing the nonlinear behavior of the diode is shown in Figure 2.27 (b) [67].

(a) (b)

Figure 2.27 Diode, (a) schematic diagram, (b) detailed circuit-based EMT model

### 2.2.2 IGBT

The schematic diagram and detailed circuit-based EMT model of IGBT is shown in Figure 2.28 (a) and Figure 2.28 (b), respectively. As shown in this figure, the detailed circuit based EMT model of IGBT consists of controlled switch, diodes, and an RLC branch modeling the snubber [67].

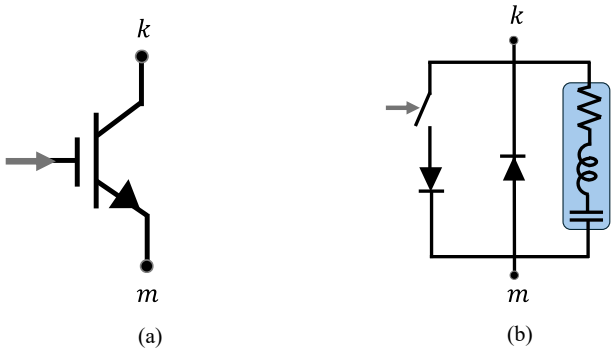


Figure 2.28 IGBT, (a) schematic diagram, (b) detailed circuit-based EMT model

## 2.3 Circuit-Based EMT model of Battery

The battery can also be modeled by the circuit-based approach. Figure 2.29 shows the schematic diagram of a battery. The battery is represented by a controlled voltage source while its voltage and state of charge (SOC) are calculated by control blocks as shown in Figure 2.29 (b). In this figure, $R_s$ and $R_p$ are the series and parallel resistance of the battery. Also, the output voltage and SOC of battery can be calculated by the analytical function related to the battery type. Further details regarding the detailed modeling of the battery are available in [68]. In this thesis, the detailed circuit-based representation of the lithium-ion (Li-Ion) battery, provided in EMTP®, is used.

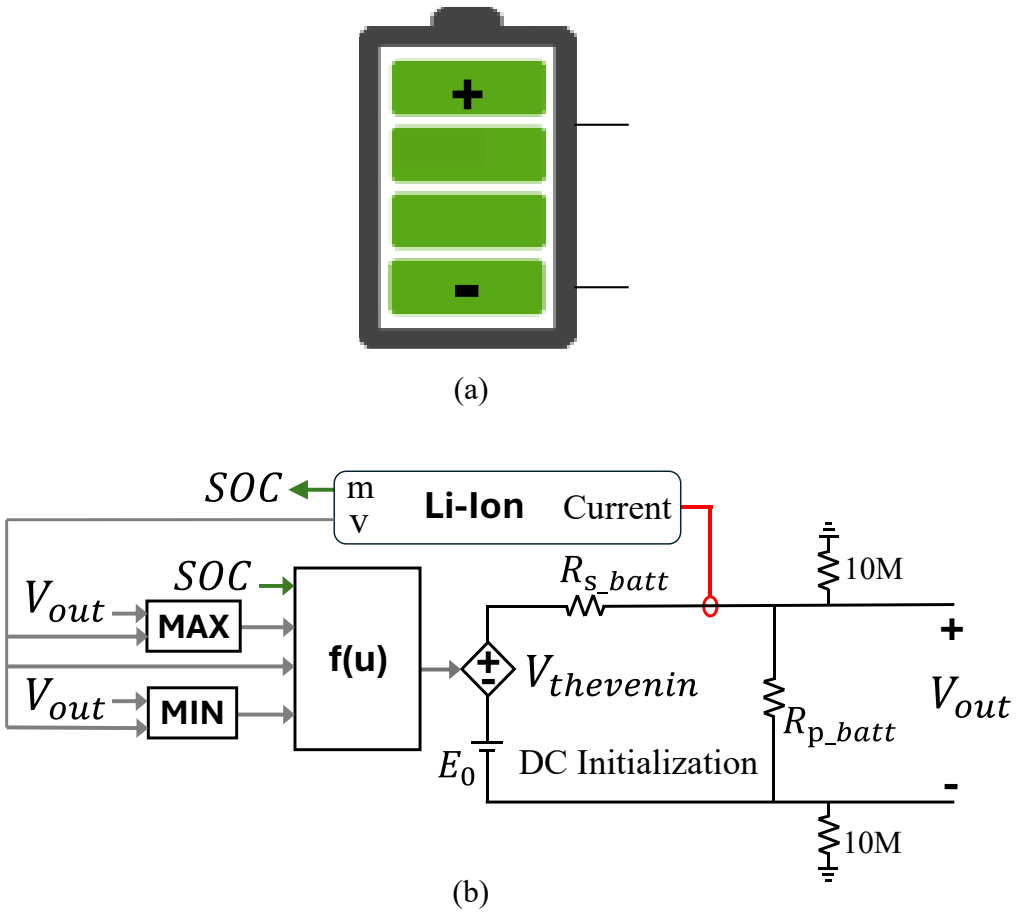


Figure 2.29 EMT modeling of battery, (a) schematic diagram, (b) circuit-based model

## 2.4 Conclusion

In this chapter, the basic principles of using circuit-based approach for system-level modeling of the SRM drive system and its external power system were introduced. The machine model consists of the seamlessly coupled magnetic, electric, and mechanical circuits.

To illustrate the concept of magnetic circuits, the magnetic circuit of a simple gapped core and an electric machine were presented. The calculation of the permeance's value with rectangular and cylindrical shapes is demonstrated. To account for the nonlinear behavior of the ferromagnetic core, nonlinear permeances are utilized, and the derivation of the Norton companion model for nonlinear permeances was provided. The machine's airgap was modeled using a non-meshed approach, which maintains the same circuit topology during the simulation. The values of airgap permeances were calculated by the TCM method and analytical functions. Furthermore, the

seamless coupling of magnetic and electric circuits, torque calculation, circuit-based representation of machine's mechanical dynamics behavior, and the application of symmetry to reduce the study domain were also investigated in this chapter. Additionally, the detailed circuit-based EMT model of the power electronics devices and battery are presented in this chapter.

# CHAPTER 3 PROPOSED MAGNETIC CIRCUITS FOR THE SRM EMT MODEL

In the previous chapter, the principle of using the circuit-based approach to represent the transient behaviour of SRM drive system and its external power system is presented. In this chapter, we use the circuit-based methodology to propose EMT models of the SRM that can be used for various transient studies.

We start developing the circuit-based EMT model of SRM with a basic model that neglects the nonlinear magnetic behavior of the ferromagnetic core, space harmonics of the machine, and mutual coupling between the phase windings. Then, step by step, space harmonics, magnetic nonlinearities, and mutual coupling are added to the circuit-based EMT model of the SRM to develop a model that accounts for all the detailed magnetic phenomena occurring within the machine. These steps are organized as presented in Table 3-1, and for each step a circuit-based EMT model is proposed with its name provided.

Table 3-1 Progressive development of the circuit-based EMT model of the SRM

| Step | Modeling Enhancement | Delivered model |
|---|---|---|
| 1 | Developing the most basic model | type-1 lumped model |
| 2 | Adding the space harmonics | type-2 lumped model |
| 3 | Adding the local airgap permeances | type-2 lumped model |
| 4 | Incorporating the nonlinear magnetic behavior | type-3 lumped model |
| 5 | Considering the mutual coupling between phases | Topological model |
| 6 | Accounting for the leakage flux in stator and rotor slots | Simplified distributed model |

| | | |
|---|---|---|
| 7 | Considering all detailed magnetic phenomena | Distributed model |

At each step, we add more detailed to the circuit-based EMT model of SRM, which is expected to improve accuracy while increasing computational burden, as illustrated in Figure 3.1.

All proposed model consists of seamlessly coupled magnetic, electric, and mechanical equivalent circuits. The mechanical equivalent circuit is similar in all models. Recall that the mechanical equivalent circuit is presented in section 2.1.3 in Chapter 2

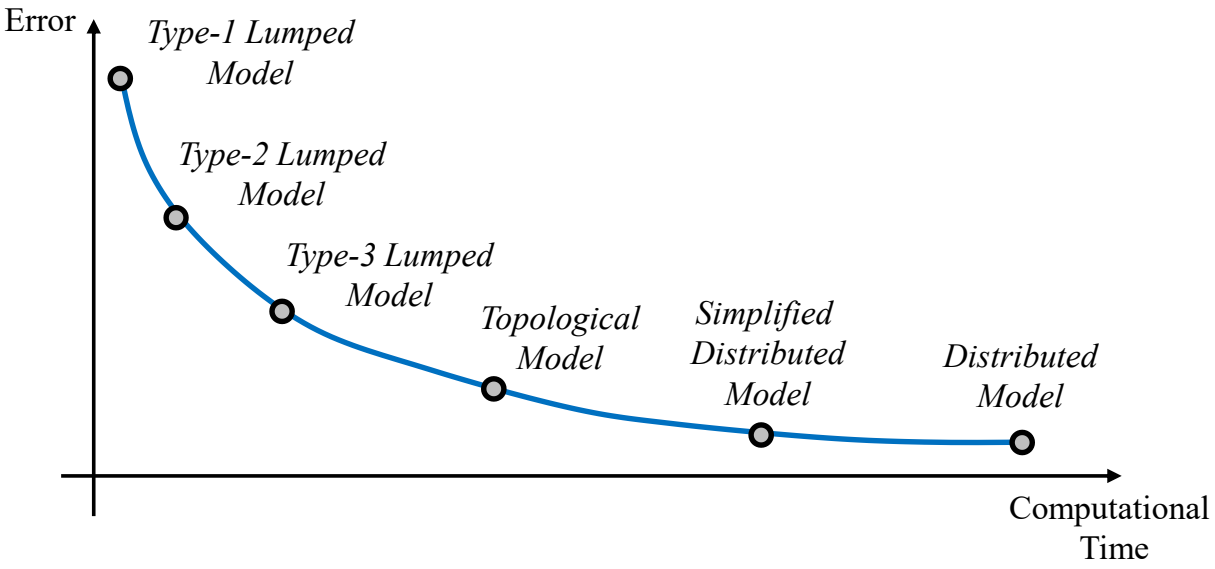


Figure 3.1 Expected computational time and accuracy of models

## 3.1 The most basic model (type-1 lumped model)

As mentioned, we start developing the circuit-based EMT model of the SRM by neglecting the effect of space harmonics, saturation, and mutual coupling between phases. In this regard, the inductance of the SRM only depends on the rotor position. Thus, it can be concluded that the phase flux linkage of SRM can be calculated as

$$\Phi_a\left(\theta, i_a\right) = L_a\left(\theta\right) \times i_a \tag{3.1}$$

where $\Phi_a$ is the phase A flux linkage, $L_a$ is the inductance of phase A, $\theta$ is the rotor position, and $i_a$ is the phase A current. Thus, the time derivative of the phase flux linkage can be calculated as

$$\frac{d\Phi_a(\theta,i_a)}{dt}=\frac{d\left(L_a(\theta)\times i_a\right)}{dt} \tag{3.2}$$

$$\frac{d\Phi_a(\theta,i_a)}{dt}=\frac{dL_a(\theta)}{dt}\times i_a+L_a(\theta)\times\frac{di_a}{dt} \tag{3.3}$$

$$\frac{d\Phi_a(\theta,i_a)}{dt}=\frac{dL_a(\theta)}{d\theta}\times\frac{d\theta}{dt}\times i_a+L_a(\theta)\times\frac{di_a}{dt} \tag{3.4}$$

In the above-mentioned equations, the time derivative of the rotor position corresponds to the machine speed, expressed as

$$\frac{d\theta}{dt}=\omega_e \tag{3.5}$$

where $\omega_e$ is the electrical speed of the machine.

Thus, we can rewrite the (3.4) as

$$\frac{d\Phi_a(\theta,i_a)}{dt}=e_a(i_a,\theta,\omega_e)+L_a(\theta)\times\frac{di_a}{dt} \tag{3.6}$$

$$e_a(i,\theta,\omega)=\frac{dL_a(\theta)}{d\theta}\times\omega_e\times i_a \tag{3.7}$$

Therefore, the electrical equation in phase A of SRM can be written as

$$v_a-R_a i_a=\frac{d\Phi_a}{dt} \tag{3.8}$$

where $v_a$ is the terminal voltage of the phase A and $R_a$ is the phase A resistance. The electrical circuit of SRM's phase A is shown in Figure 3.2.

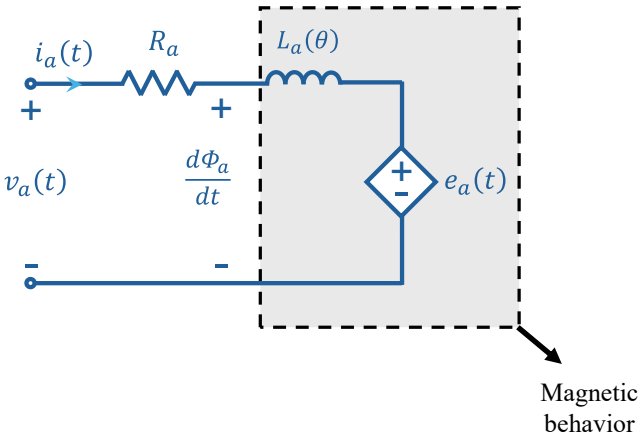


Figure 3.2 Phase domain electrical circuit of SRM

The electrical circuit shown in Figure 3.2 is a conventional representation of the SRM's electrical circuit for each phase [69]. However, in this circuit, there is not a seamless coupling between the electrical and magnetic circuits and it is not an EMT model.

To implement the EMT model of this circuit, the magnetic and electric behavior can be represented by their equivalent circuit-based representation. For ease of explanation, we develop the circuit-based EMT representation of SRM's phase circuit for an arbitrary SRM shown in Figure 3.3.

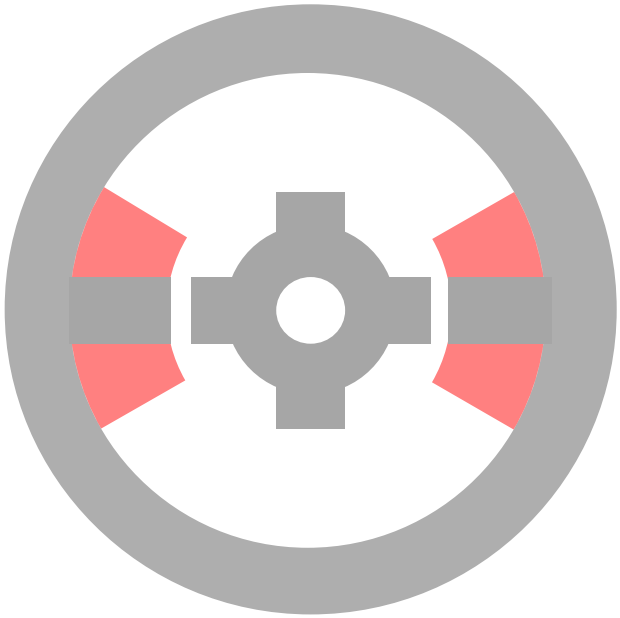

Figure 3.3 An arbitrary SRM

The coupled magnetic and electric circuit of this SRM is shown in Figure 3.4. This figure shows the coupled magnetic and electric circuit of SRM's phase A. In this figure, the electric and magnetic circuits are in blue and black, respectively. As shown in this figure, the mutator connects the magnetic and electric circuits. In this figure, two mutators are used, each corresponding to one winding of the phase-A coil shown in Figure 3.3. The back-EMF of each mutator can be calculated as

$$e_{c1_a} = e_{c2_a} = -N\frac{d\varphi_a}{dt} \tag{3.9}$$

where $e_{c1_a}$ and $e_{c2_a}$ are the back-EMF corresponds to the first and second winding of phase A.

Also, the magnetic circuit consists of variable permeances modeling the dependency of phase flux linkage on the rotor position.

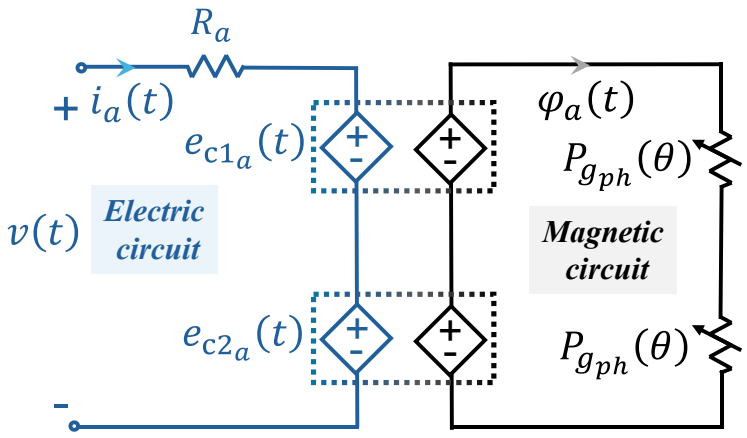


Figure 3.4 The most basic circuit-based EMT model

The domain of study can be reduced to one stator pole per phase of the SRM as shown in Figure 3.5.

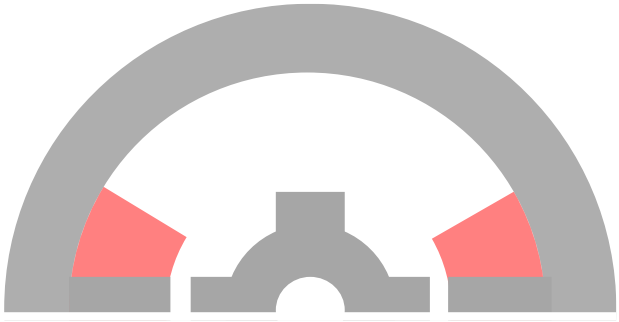

Figure 3.5 Reducing the study domain of the arbitrary SRM using symmetry

To implement the symmetry condition in the circuit shown in Figure 3.4, one stator pole within a phase of SRM should be considered in the circuit-based model as shown in Figure 3.6. This circuit is named type-1 lumped circuit-based EMT model in this thesis. As shown in this figure, only one mutator is used since we modeled one stator pole within a phase of SRM. In this circuit, the value of the back-EMF in the electric circuit can be calculated as

$$e_{c1_a} = -N\xi \frac{d\varphi_a}{dt} \tag{3.10}$$

where $\xi$ is the symmetry factor. For this arbitrary SRM, the symmetry factor is equal to two, whereas for the case study presented in this thesis, it is equal to four.

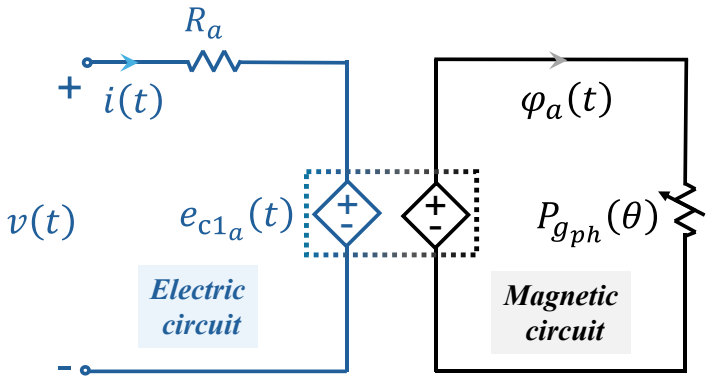


Figure 3.6 The most basic (type-1) circuit-based EMT model of SRM with symmetry

Due to neglecting the effects of the magnetic core and the machine's space harmonics, the variable permeance $P_{g_{ph}}$ models the airgap variation using a cosine function, as [70]:

$$P_{g_{ph}}(\theta) = H_0 + H_1 \cos\left(N_r\theta + \delta_p\right) \tag{3.11}$$

$$H_0 = \frac{P_{g\max} + P_{g\min}}{2} \tag{3.12}$$

$$H_1 = \frac{P_{g\max} - P_{g\min}}{2} \tag{3.13}$$

where $\theta$ is the rotor position, $N_r$ is the rotor teeth number, and $\delta_p$ is the phase shift, $P_{g\max}$ and $P_{g\min}$ represent the value of the airgap permeance in the aligned and unaligned positions, respectively. In this thesis, we named $P_{g_{ph}}$ the global airgap permeance. Figure 3.7 plots the global airgap permeance function illustrated in equation (3.11) for a machine with four rotor poles ( $N_r = 4$ ).

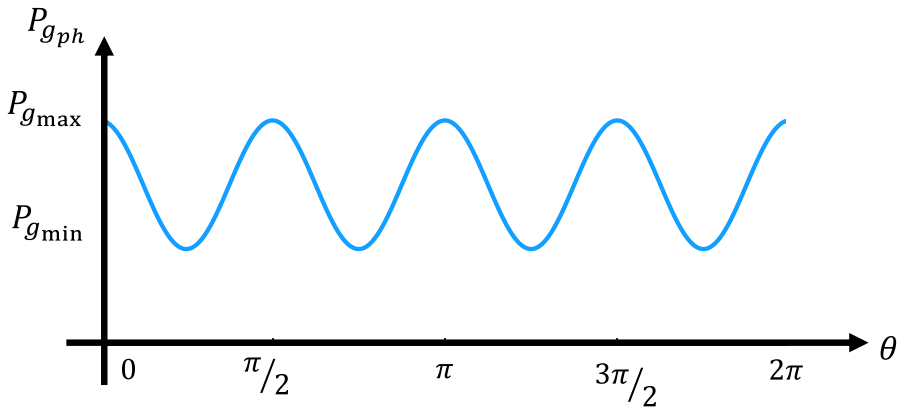


Figure 3.7 Airgap permeance characteristic of type-1 lumped circuit-based EMT model

The calculation of $P_{g\max}$ and $P_{g\min}$ is investigated in the following parts of this section.

To have a better explanation about the airgap permeance function presented in this section, we present the link between the conventional phase-domain electrical circuit of the SRM in Figure 3.2 and the proposed type-1 circuit-based EMT shown in Figure 3.6. To this aim, Figure 3.8 illustrates the same conventional circuit implemented using the methodology of type-1 lumped circuit-based EMT model. In this electric circuit, the inductance of the phase A can be written as:

$$L_a(\theta) = L_0 + L_1 \cos\left(N_r\theta\right) \tag{3.14}$$

It is worth mentioning to recall that

$$\frac{d\Phi_a(\theta,i_a)}{dt}=\frac{d\left(L_a(\theta)\times i_a\right)}{dt} \tag{3.15}$$

Thus, by substituting the equation (3.14) into the equation (3.4), the time derivative of the phase A flux linkage is expressed as

$$\frac{d\Phi_a(\theta,i_a)}{dt}=-L_1\times N_r\times\sin\left(N_r\theta\right)\times\omega_e\times i_a+\left(L_0+L_1\cos\left(N_r\theta\right)\right)\times\frac{di_a}{dt} \tag{3.16}$$

This equation can be written as

$$\frac{d\Phi_a(\theta,i_a)}{dt}=\underbrace{-L_1\times N_r\times\sin\left(N_r\theta\right)\times\omega_e\times i_a}_{e_{c1_a}}+L_0\times\frac{di_a}{dt}+L_1\cos\left(N_r\theta\right)\times\frac{di_a}{dt} \tag{3.17}$$

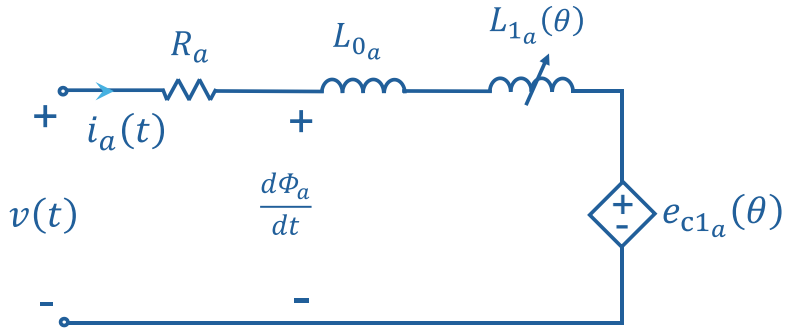


Figure 3.8 Purely electric circuit corresponds to the proposed type-1 lumped circuit-based EMT model

It is worth noting that the electric circuit in Figure 3.8 is not an EMT model. This circuit is presented to show the correspondence between the conventional phase electrical circuit of SRM and the proposed type-1 lumped circuit-based EMT model.

After explanation of the proposed type-1 lumped circuit-based EMT model of SRM and its correspondence with the conventional phase electric circuit of SRM, we must calculate $P_{g_{\max}}$ and $P_{g_{\min}}$. Thus, the following part of this section presents the calculation of these parameters.

### 3.1.1 Calculation of Minimum and Maximum values of Airgap Permeances

The value of $P_{g\max}$ and $P_{g\min}$ can be calculated by analytical or numerical methods.

#### 3.1.1.1 Analytical Method

The airgap permeance of the SRM in the aligned and unaligned positions can be calculated by analytical functions. For instance, the analytical formulas for calculating the airgap permeance values in the aligned and unaligned positions are derived in [59] and [71] using flux tubes. In this method, defining the flux path, typically performed by using FEM models, is the first step [72], [73], [74]. This step aims to identify the flux lines in the airgap in the aligned and unaligned positions. Then, based on the yielded flux lines in the aligned and unaligned positions, the proper flux tube can be developed to calculate the equivalent permeances representing those flux lines.

Figure 3.9 shows the flux tubes of the airgap in aligned and unaligned positions which are derived from flux lines yielded from FEM simulations.

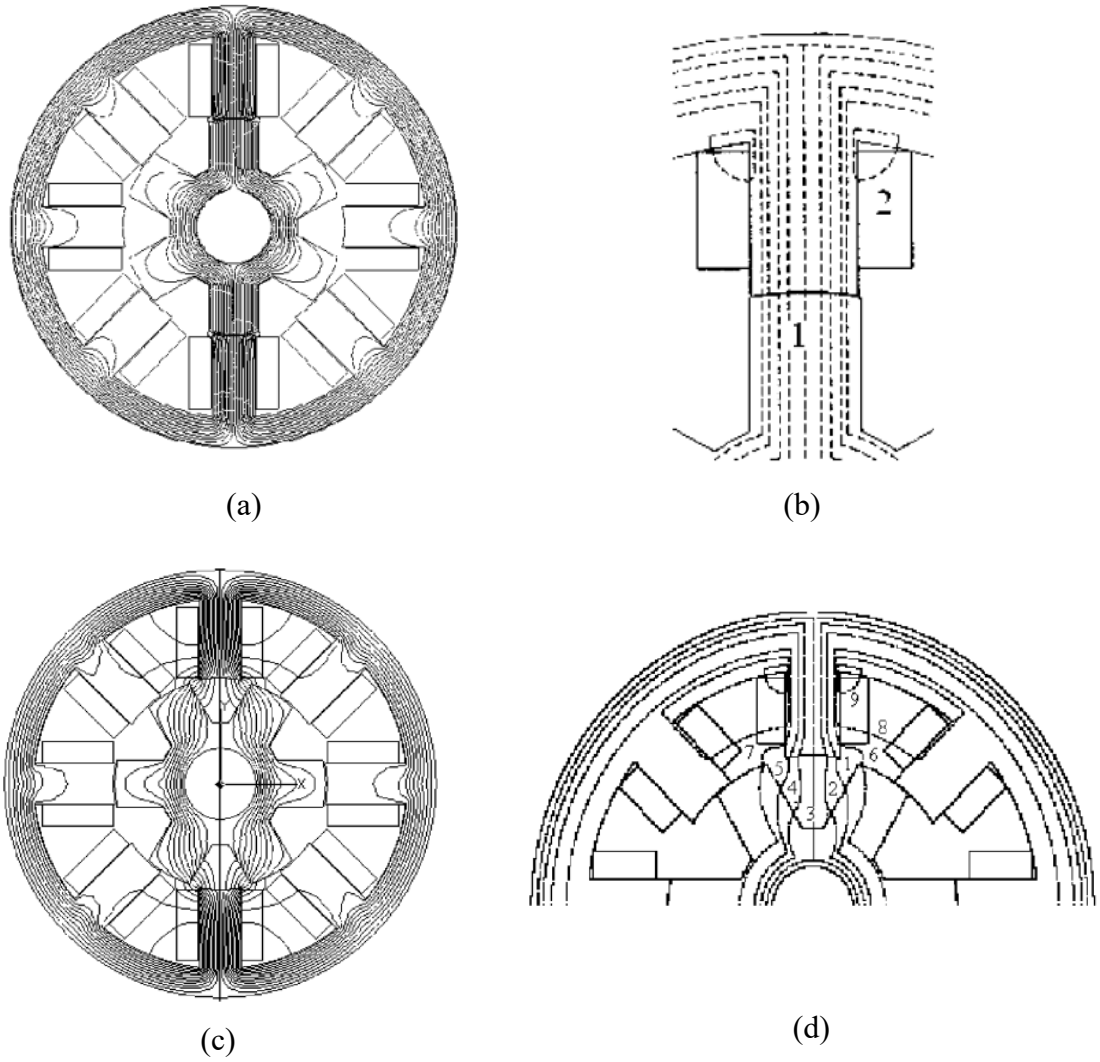


(a) (b)

(c) (d)

Figure 3.9 The flux lines and flux tubes in various positions, (a) flux lines in aligned position, (b) flux tubes in aligned position, (c) flux line in unaligned position, and (d) flux tubes in unaligned position [75]

This method lacks generality, as it relies on predefining the flux path within the machine.

### 3.1.1.2 Numerical Method

The value of $P_{g\max}$ and $P_{g\min}$ can be calculated by TCM. As mentioned in Section 2.1.1.3 in Chapter 2, TCM can be implemented by FEM or its circuit-based representation. In this work, we use the tool we developed for the implementation of circuit-based TCM in EMT-type software. In this regard, TCM must be implemented to calculate the value of the airgap permeances in the aligned and unaligned positions. Figure 3.10 shows the meshed study domain of the circuit-based

TCM for calculating these parameters. To calculate the value of $P_{g_{max}}$, the energized tooth of the stator and rotor tooth should be in the aligned position, as shown in Figure 3.10 (a). Figure 3.10 (b) shows the circuit-based TCM study domain in which the energized stator tooth and rotor tooth are in the unaligned position to calculate the value of $P_{g_{min}}$.

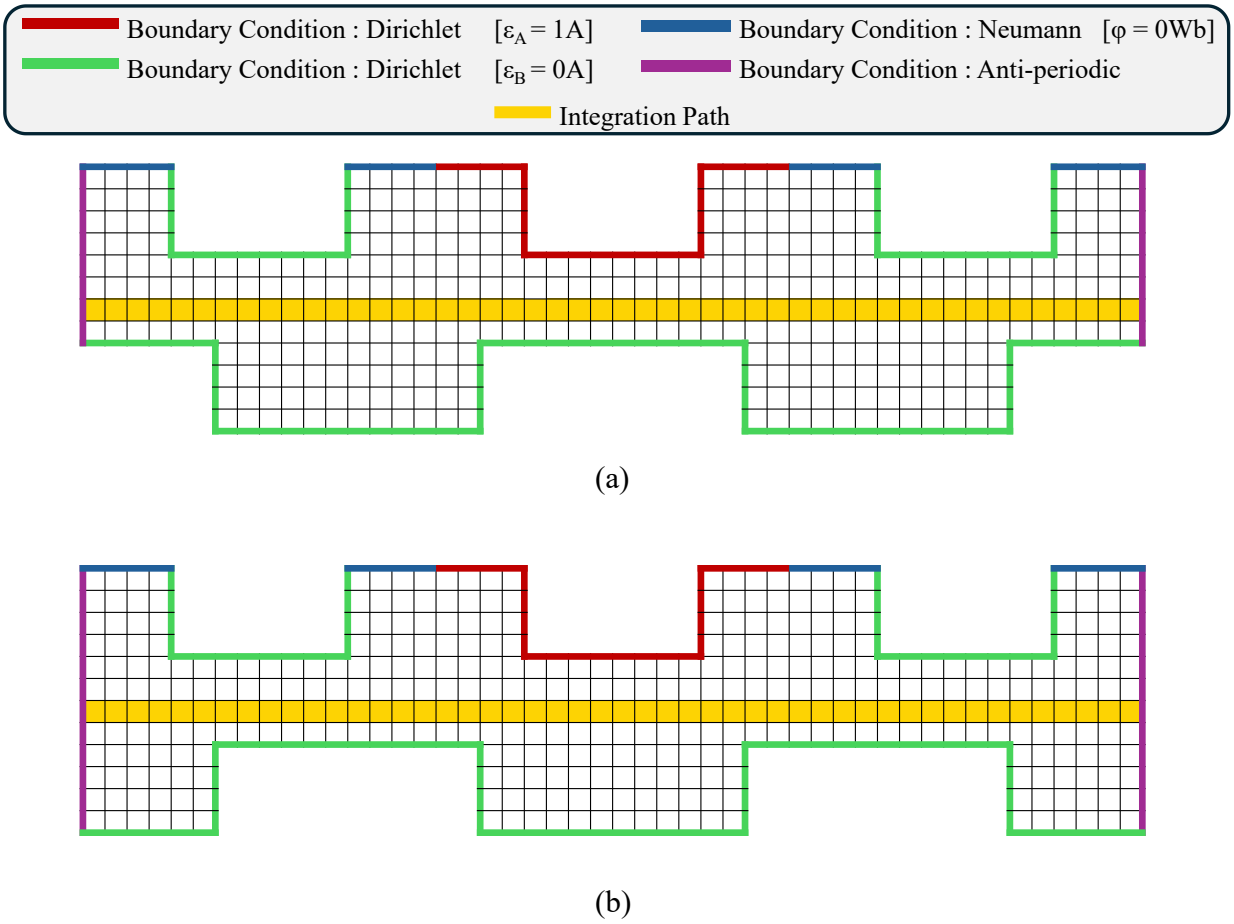


Figure 3.10 Using circuit-based representation of TCM to calculate parameters of airgap cosine function, (a) aligned position, (b) unaligned position

## 3.2 Adding space harmonic (type-2 lumped model)

In this step, the space harmonics caused by the doubly salient structure of SRM are considered while the effect of the nonlinear magnetic behavior of the ferromagnetic core is neglected. The coupled magnetic and electric circuit is shown in Figure 3.11.

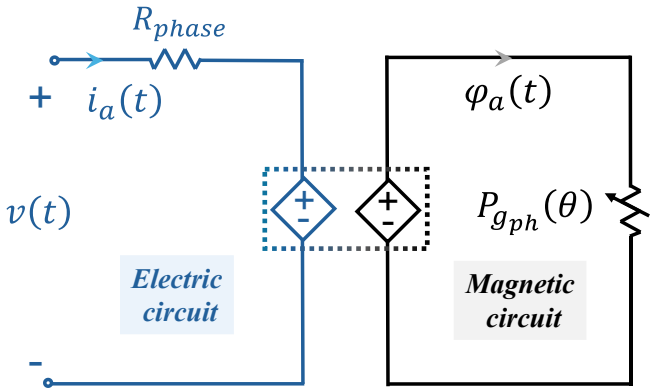


Figure 3.11 Type-2 lumped circuit-based EMT model of SRM

This circuit is similar to the type-1 lumped circuit-based model while the value of the airgap variable permeance is not calculated by the cosine function. To incorporate the effect of space harmonics, we must simulate the TCM in various rotor positions, from the aligned to unaligned position, as shown in Figure 3.12. The global airgap permeance of the type-2 lumped model for a SRM with four poles is shown in Figure 3.13. The global airgap permeances of the type-2 lumped circuit-based EMT model can be described as

$$P_{g_{ph}}(\theta) = H_0 + \sum_{n=1} H_n \cos\left(nN_r\theta + \delta_p\right) \tag{3.18}$$

where $n$ is the harmonic order.

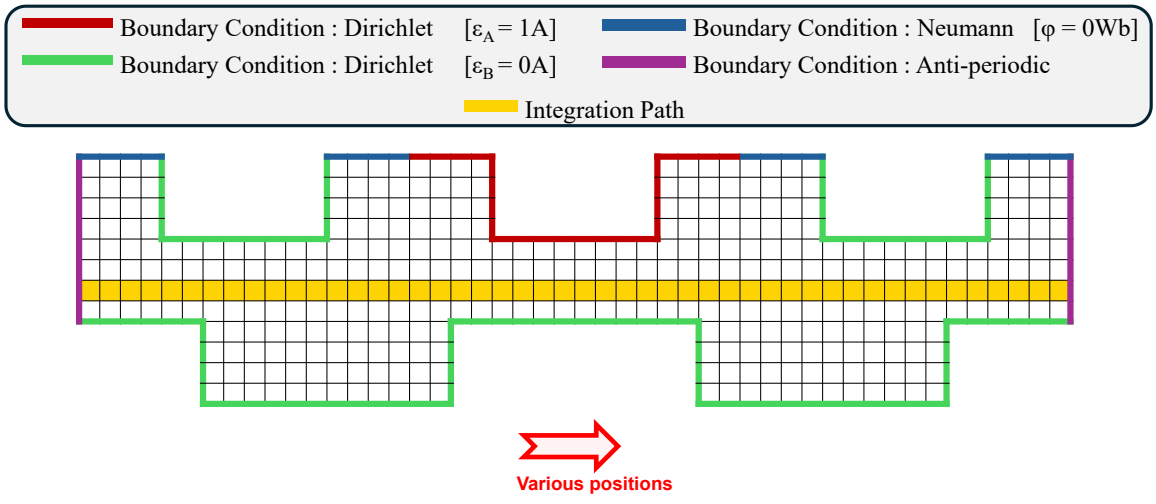


Figure 3.12 Using circuit-based representation of TCM for incorporating the space harmonics into the phase airgap permeance

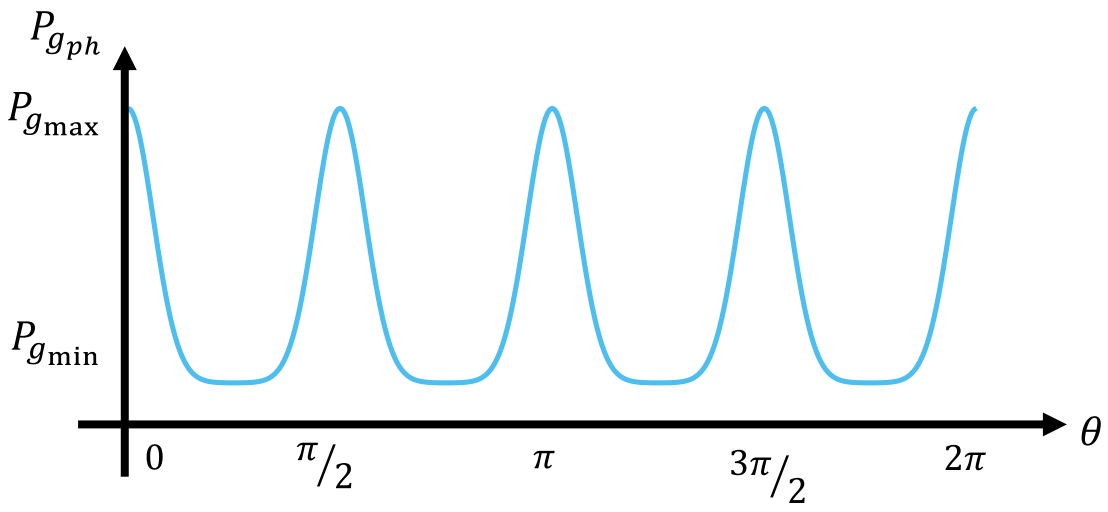


Figure 3.13 Global airgap permeance function

## 3.3 Adding the local airgap permeances

As presented in the previous sections, the global airgap permeance represents the effect of all the rotor teeth together on one stator pole. However, it is also possible to account for space harmonics by using multiple variable permeances that connect the stator teeth of that phase to all rotor teeth, as shown in Figure 3.14 [70]. In this figure, the airgap permeances between the first stator tooth associated with the phase A and rotor teeth are represented by $P_{g11}$ to $P_{g14}$. Also, $P_{g21}$ to $P_{g24}$ represents the airgap permeances between the second stator tooth associated with the phase A and rotor teeth. The value of each airgap permeance can be calculated by either the circuit-based representation of TCM, as presented in Figure 3.15, or analytical function presented in section 2.1.1.3 in Chapter 2.

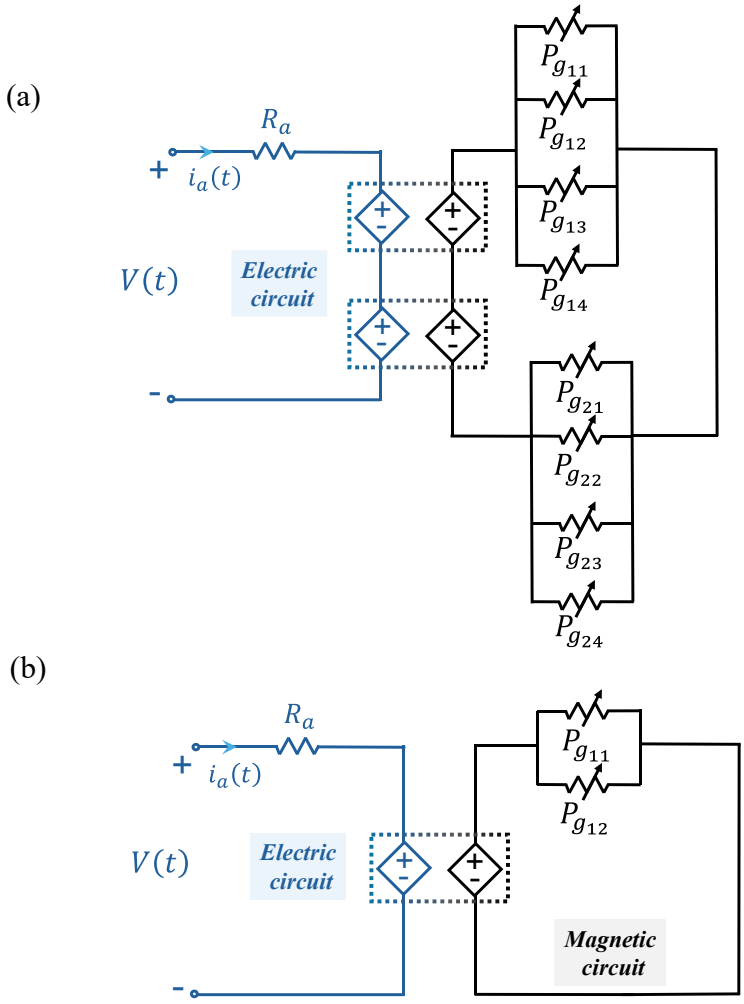


Figure 3.14 Type-2 lumped model, (a) without symmetry, (b) with symmetry

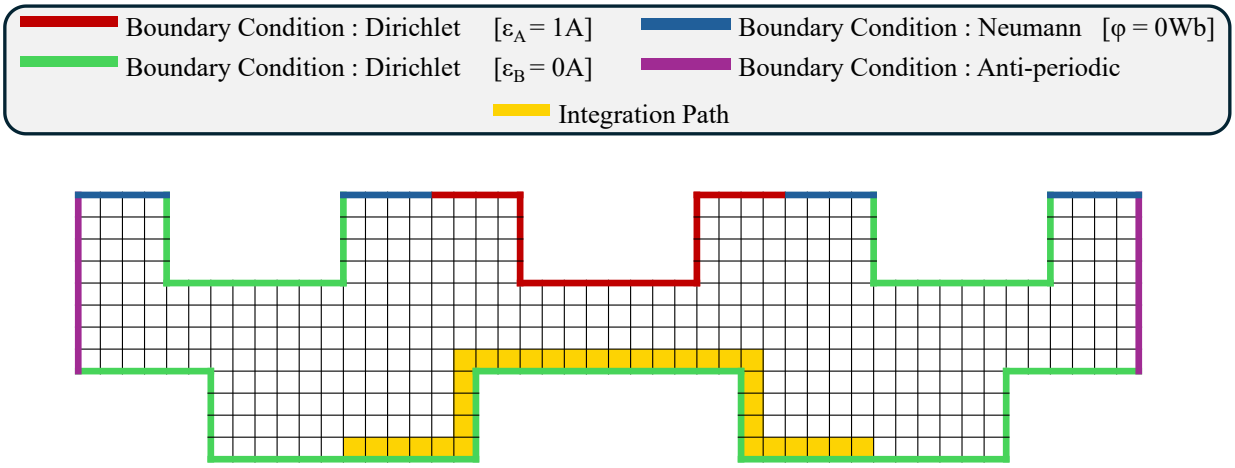


Figure 3.15 Using circuit-based TCM for airgap calculation for type-2 lumped model

In the time domain simulations, the value of the airgap permeances is calculated using analytical functions as presented in section 2.1.1.3 in Chapter 2.

Figure 3.16 shows the airgap permeance function of phase A for a four poles SRM. The airgap permeance connecting stator tooth to the fourth tooth of the rotor is shown in Figure 3.16 (a) while Figure 3.16 (b) shows all airgap permeacnes connecting stator tooth to all rotor teeth. As shown in this figure, four permeances, $P_{g11}$ to $P_{g14}$, are contributing in the airgap permeance function. The value of each airgap permeance $P_{g11}$ to $P_{g14}$ can be calculated by TCM equivalent circuit or analytical function presented in section 2.1.1.3 in Chapter 2.

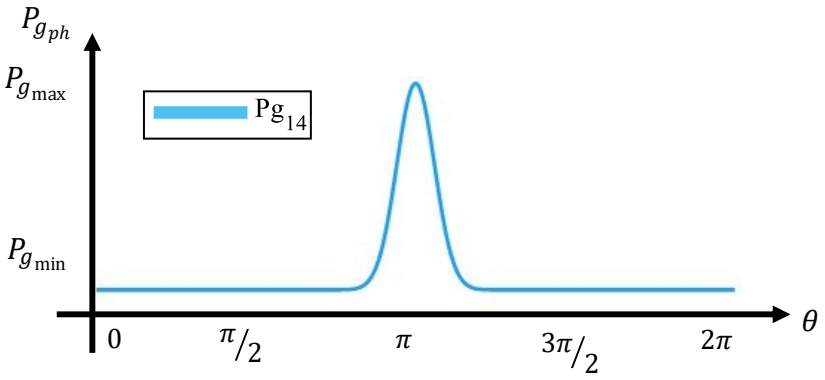


(a)

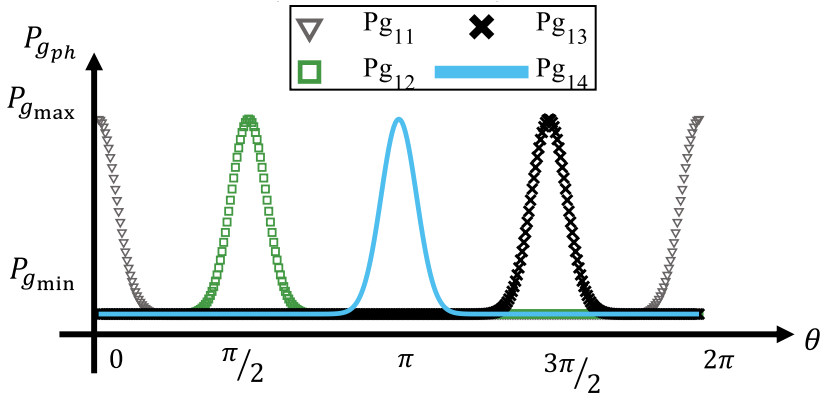


(b)

Figure 3.16 Characteristics of the local airgap permeance of type-2 lumped circuit-based EMT model

## 3.4 Adding the nonlinear magnetic behavior of the ferromagnetic core (type-3 lumped model)

In this section, we want to include the effect of the nonlinear magnetic behavior of the ferromagnetic core in the circuit-based EMT model proposed in the type-2 lumped EMT model. To this aim, the electrical equations for phase A of SRM should be rewritten while considering the saturation. In this case, the inductance is dependent on the rotor position and phase current. Thus, the flux linkage can be calculated as

$$\Phi_a(\theta,i_a)=L_a(\theta,i_a)\times i_a \tag{3.19}$$

The time derivative of the above equation can be expressed as

$$\frac{d\Phi_a(\theta,i_a)}{dt}=\frac{d\left(L_a(\theta,i_a)\times i_a\right)}{dt} \tag{3.20}$$

$$\frac{d\Phi_a(\theta,i_a)}{dt}=\frac{dL_a(\theta,i_a)}{dt}\times i+L_a\times\frac{di_a}{dt} \tag{3.21}$$

$$\frac{d\Phi_a(\theta,i_a)}{dt}=\frac{\partial L_a(\theta,i_a)}{\partial t}\times\frac{d\theta}{dt}\times i_a+\frac{\partial L_a(\theta,i_a)}{\partial i_a}\times\frac{di_a}{dt}\times i_a+L_a(\theta,i_a)\times\frac{di_a}{dt} \tag{3.22}$$

It is worth mentioning that

$$\frac{d\theta}{dt}=\omega_e \tag{3.23}$$

Thus, the equation (3.22)

$$\frac{d\Phi_a(\theta,i_a)}{dt}=\frac{\partial L_a(\theta,i_a)}{\partial t}\times\omega_e\times i_a+\frac{\partial L_a(\theta,i_a)}{\partial i_a}\times\frac{di_a}{dt}\times i_a+L_a(\theta,i_a)\times\frac{di_a}{dt} \tag{3.24}$$

$$\frac{d\Phi_a(\theta,i_a)}{dt}=\underbrace{\frac{\partial L_a(\theta,i_a)}{\partial t}\times\omega_e\times i_a}_{e_{1_a}}+\underbrace{\frac{\partial L_a(\theta,i_a)}{\partial i_a}\times\frac{di_a}{dt}\times i_a}_{e_{2_a}}+L_a(\theta,i_a)\times\frac{di_a}{dt} \tag{3.25}$$

where $e_{1_a}$ and $e_{2_a}$ are the back-EMF due to the electromechanical energy conversion and saturation, respectively. Therefore, the equation (3.25) is written as

$$\frac{d\Phi_a(\theta,i_a)}{dt} = e_{1_a}(\theta,i_a) + e_{2_a}(\theta,i_a) + L_a(\theta,i_a)\times\frac{di_a}{dt} \tag{3.26}$$

Also, the back-EMF of phase A is equal to

$$e_a(\theta,i_a) = e_{1_a}(\theta,i_a) + e_{2_a}(\theta,i_a) \tag{3.27}$$

Thus

$$\frac{d\Phi_a(\theta,i_a)}{dt} = e_a(\theta,i_a) + L_a(\theta,i_a)\times\frac{di_a}{dt} \tag{3.28}$$

Therefore, the phase electrical circuit of the phase A shown in Figure 3.2 can be modified by considering the effect of saturation as shown in

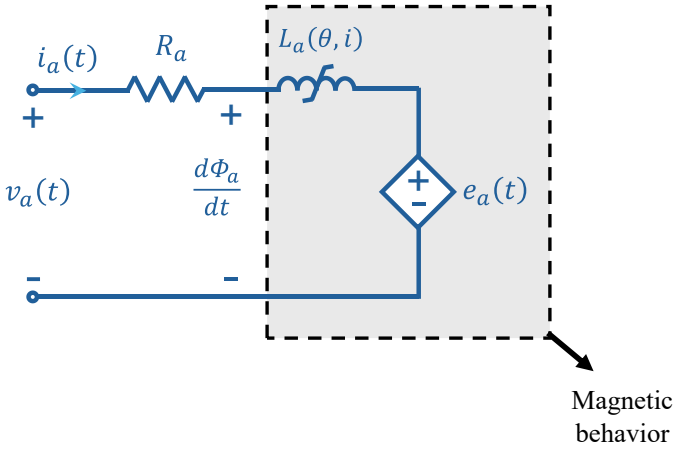


Figure 3.17 Phase domain electrical circuit of SRM considering saturation

The next two sections review existing methods for modeling nonlinear magnetic behavior and space harmonics in the SRM. Subsequently, the proposed approach for considering the effect of nonlinear magnetic behavior in the circuit-based EMT model of SRM is presented.

### 3.4.1 Analytical Approach

In [59] and [71], the flux paths within the electric machine are represented by flux tubes. As mentioned in Section 3.1.1.1, in this approach, the first step is to identify the flux tubes associated with the machine's flux lines. Therefore, a detailed numerical model, such as FEM, must be run to determine the appropriate flux tubes for the machine's flux lines. Figure 3.18 shows the flux tubes

associated with the flux lines within the airgap of an SRM in the aligned and semi-aligned positions.

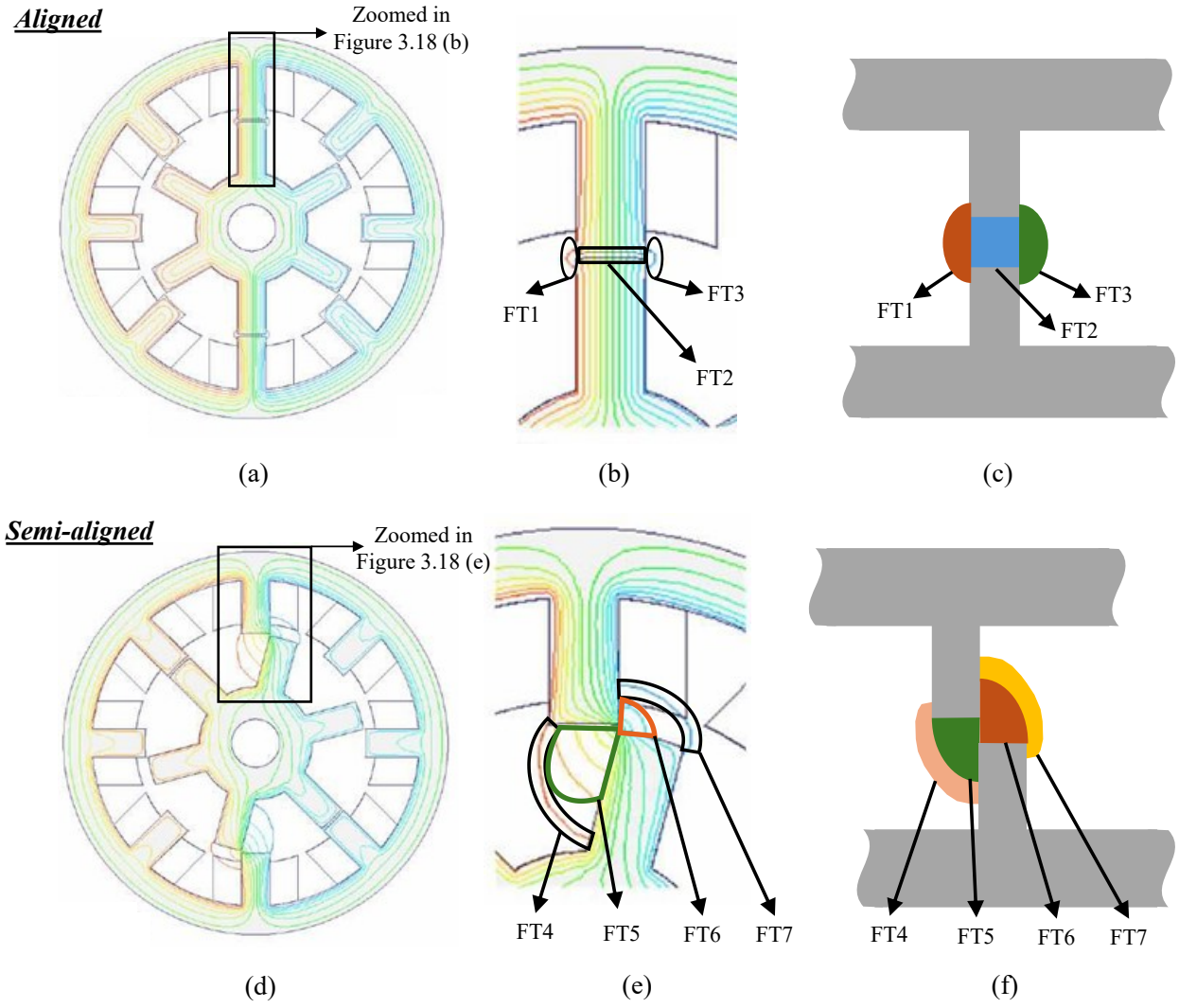


Figure 3.18 Flux tubes of within airgap of a SRM in various relative positions between rotor and stator teeth, (a) aligned, and (b) semi-aligned [59]

Figure 3.18 (a) and Figure 3.18 (b) show the flux lines in the aligned position. The airgap flux tubes in the aligned position are shown in Figure 3.12 (c). These flux tubes are named as FT1, FT2, and FT3 in this figure. Moreover, the flux lines in the unaligned position are shown in Figure 3.18 (d) and Figure 3.18 (e) while the flux tubes of the airgap in the semi-aligned position are illustrated in Figure 3.18 (f). In this figure, the flux lines of the airgap in the semi-aligned position are named as FT4 to FT7.

As shown in Figure 3.18, to account for the rotation of the rotor in the flux-tube based magnetic circuits, the circuit topology should be changed during simulation. Thus, various magnetic circuits should be derived for aligned, semi-aligned, and unaligned positions. However, changing the circuit topology during simulation makes the flux-tube based method unsuitable for EMT studies. Moreover, this method requires predefining the flux path which increase complexity of the model. Although this is an analytical model while implementation of the saturation requires a numerical method.

### 3.4.2 Lookup Table-Based Approach

In many articles, lookup tables are employed to include the effect of the nonlinear magnetic behavior of the SRM in its model. This method aims to account for the magnetic saturation and its relation with the rotor position. As an example, Figure 3.19 shows that the flux linkage of the SRM exhibits higher nonlinear behavior as the rotor and stator teeth move toward alignment.

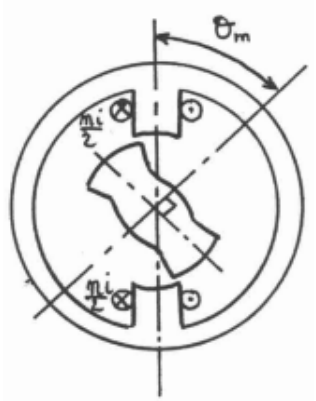


(a)

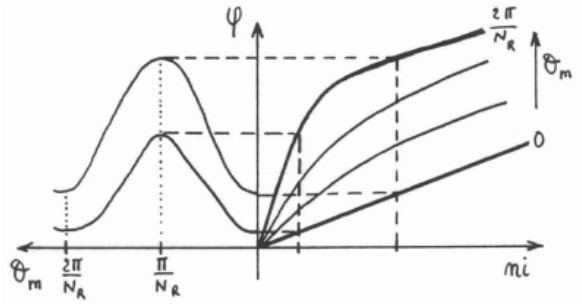


(b)

Figure 3.19 Illustration of SRM's nonlinear characteristics, (a) an arbitrary SRM, (b) the nonlinear characteristics of the SRM's flux linkage [76]

The lookup table method is based on importing the machine's nonlinear characteristics, such as flux linkage and torque, into the drive model using lookup tables [77], [78], [79]. These characteristics, including phase flux linkage, inductance, and torque at various stator currents and rotor positions, are typically obtained through experimental measurements [80], [81] or FEM simulations [82], [83]. The obtained static results are stored and then imported into the drive system model for time-domain simulations. During these simulations, interpolation is used at each time step to estimate values between the available data points. Figure 3.20 shows the lookup tables presenting flux linkage and torque of SRM.

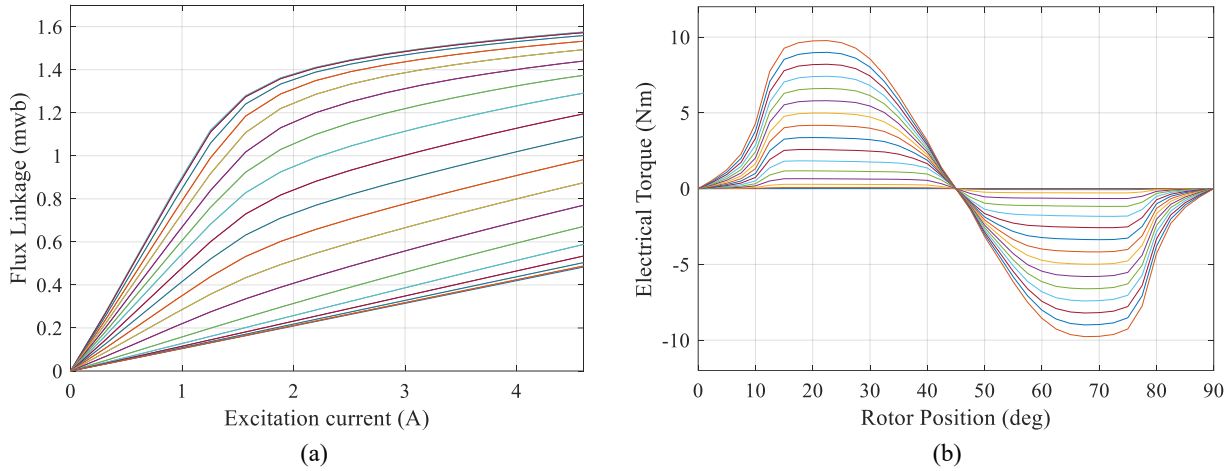


Figure 3.20 Characteristics of a SRM at various rotor position and current values, (a) flux linkage, (b) static torque

Alternatively, some other papers use analytical functions to include the nonlinear magnetic characteristics of SRM. Similar to the lookup table-based model, first, the nonlinear characteristics of the SRM should be derived from an accurate numerical model or experimental test. Then, an analytical function can be fitted to represent these nonlinear characteristics in the drive system model.

As an example, the phase flux linkage profile is represented by various piecewise functions, including the parabolic function [84]. In [85] and [86], different types of 2D polynomials, such as bivariate and bi-cubic spline polynomials, are employed to model the machine's flux linkage and torque. Moreover, other nonlinear functions, including Gaussian functions [87], piecewise Frohlich functions [88], and exponential functions [89], [90] can be used to estimate flux linkage characteristics. In some other articles, the nonlinear inductance characteristics of SRM are

represented by Fourier series whose coefficients are determined by FEM [91], [92], weighting functions [93], [94], parameter identification techniques [95], [95], etc.

Although representing the nonlinear characteristics of SRM through lookup tables or fitted functions in the drive system model is widely used in the simulations of motor drive systems, any change in machine parameters requires new FEM simulations to regenerate new lookup tables or fit new coefficients.

### 3.4.3 Proposed Circuit-Based Approach

To tackle the drawbacks of the above-mentioned approaches, the coupled magnetic and electric circuit is proposed as the circuit-based EMT model. Figure 3.21 (a) shows the magnetic circuit for a phase of SRM. This magnetic circuit is commonly used in literature and developed using flux tubes [96]. In this figure, the MMF drop is presented in reluctance and we used the same name as the original article [96]. We simplified this magnetic circuit to the circuit shown in Figure 3.21 (b). In this circuit, $R_r$ and $R_s$ are the reluctances representing the MMF drop within the rotor and stator teeth, respectively. Also, the MMF drop in the yoke of the rotor and stator are modeled by $R_{rc}$ and $R_y$. The airgap is also modeled by $R_g$.

The circuit-based EMT model that accounts for the nonlinear behavior of the ferromagnetic core can be developed by combination of the same methodology proposed in [96] and type-2 lumped model. In this regard, Figure 3.21 (c) shows the circuit-based EMT model of SRM accounting for the nonlinear magnetic behavior and space harmonics. In this figure, the modeling of space harmonics and machine's rotation is similar to type-2 model. Also, the MMF drop caused by the ferromagnetic core is represented by nonlinear permeances. In this figure, $P_{t_s}$ and $P_{t_r}$ represent the MMF drop across the stator and rotor teeth, respectively, while the MMF drop in the stator and rotor yokes are modeled by $P_{y_s}$ and $P_{y_r}$, respectively. This circuit is named type-3 lumped model in this thesis.

In Figure 3.21, we used colorful shapes in both presented circuit to have a better illustration of the difference and similarity of the type-3 lumped model and phase domain magnetic circuit of SRM proposed in [96]. In Figure 3.21 (b) the MMF drop in the rotor and stator teeth are represented by $R_r$ and $R_s$, respectively. In the proposed type-3 lumped model, $P_{t_r}$ and $P_{t_s}$ respectively model the

MMF drop in the rotor and stator. The MMF drop in the yoke of rotor and stator are modeled by $R_{rc}$ and $R_y$ in Figure 3.21 (b) while the yokes of rotor and stator are represented by $P_{y_r}$ and $P_{y_s}$ in the proposed type-3 lumped circuit-based EMT model (see Figure 3.21 (c)). In the magnetic circuit proposed in [96] (Figure 3.21 (a) and (b)), there is not coupling between magnetic and electric circuits whereas the magnetic and electric circuits are seamlessly coupled through the mutator in the proposed type-3 lumped model (see Figure 3.21 (c)). The magnetic circuit presented in Figure 3.21 (b) simulating SRM in specific position however the rotation of the SRM is considered in the proposed type-3 lumped model (see Figure 3.21 (c)) by using variable permeances.

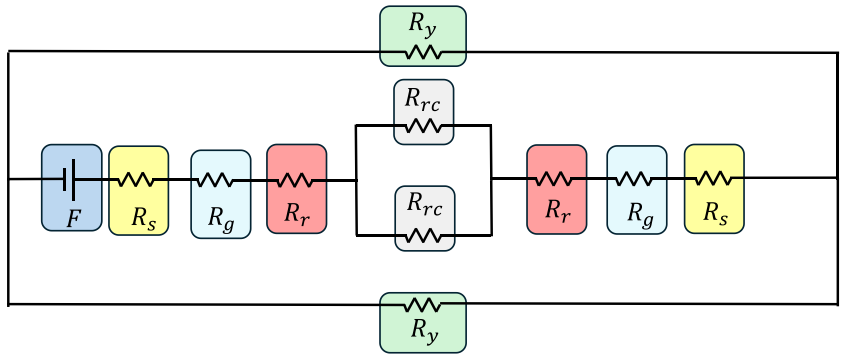


(a)

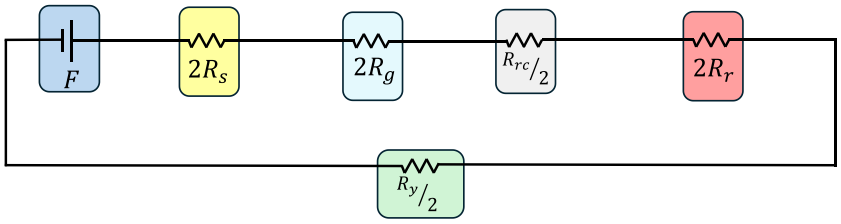


(b)

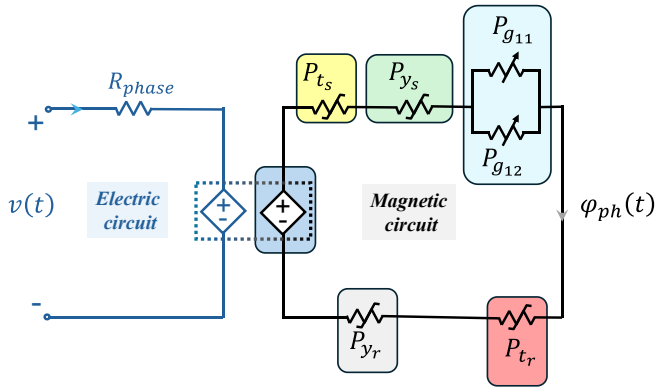


(c)

Figure 3.21 Accounting for nonlinear behavior in the magnetic circuit, (a) magnetic circuit presented in [96], (b) simplified magnetic circuit presented in [96], (c) proposed type-3 lumped circuit-based EMT model

## 3.5 Adding the mutual coupling (Topological model)

In the circuit-based models proposed in the previous sections of this chapter, the mutual coupling between phases of SRM is neglected. Neglecting the mutual coupling between SRM phases is a reasonable assumption since this coupling is low in SRMs. However, incorporating the mutual coupling between SRM phases enhances the accuracy and general applicability of the proposed circuit-based models. Thus, in this section, we add the effect of mutual coupling between phases of SRM while considering the nonlinear magnetic behavior of the SRM.

To this aim, Figure 3.22 shows the electrical circuit of SRM in phases A, B, and C. As shown in this figure, the mutual coupling is added by mutators.

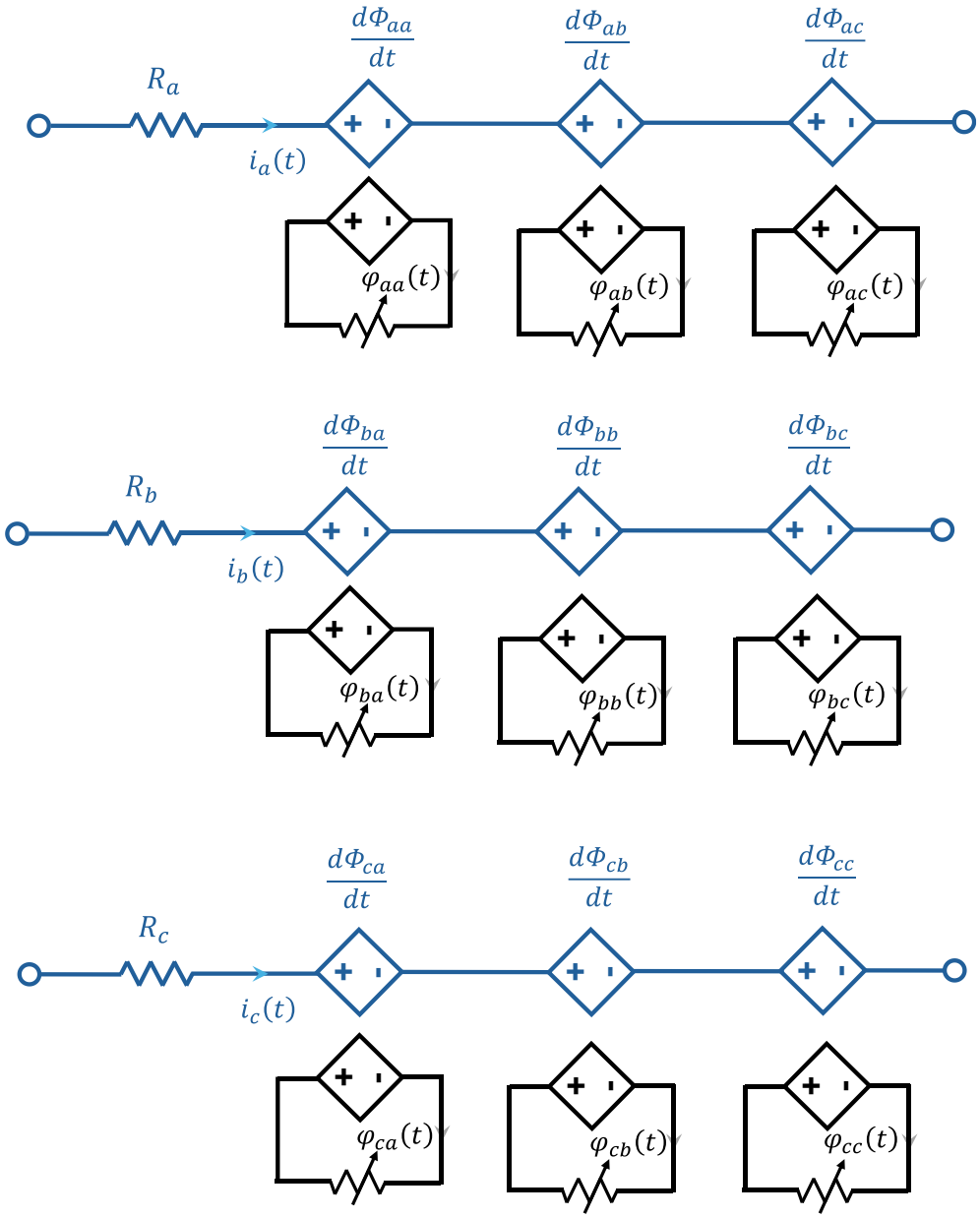


Figure 3.22 Adding the effect of mutual coupling in the circuit-based EMT model

To have a better explanation, Figure 3.23 shows the mutual fluxes in an arbitrary SRM. The mutual flux at each tooth can be calculated by the equivalent circuit representation of as shown in Figure 3.24.

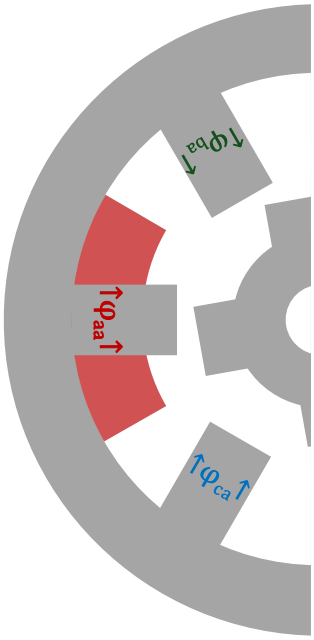


Figure 3.23 Mutual flux

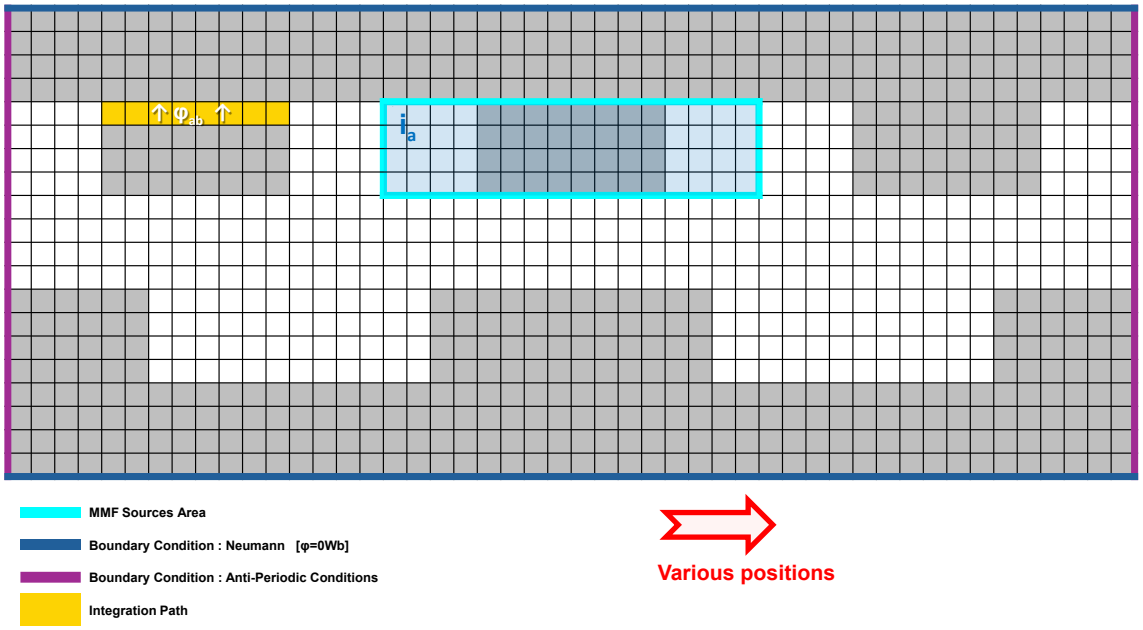


Figure 3.24 Calculation of mutual flux using equivalent circuit

As shown in Figure 3.22, the mutual coupling can be modeled using mutators, but this approach is not applicable under nonlinear conditions because the superposition theorem cannot be used in such cases.

In this regard, to account for mutual coupling while considering the nonlinear magnetic behavior and space harmonics, a more detailed model must be employed. In this regard, the topological model is proposed in this section.

Figure 3.25 illustrates the magnetic circuit of the topological model, which is seamlessly coupled to the electric circuit via mutators. As illustrated in this figure, each tooth and each yoke segment connecting two adjacent teeth in both the stator and rotor are represented by a single nonlinear permeance, which accounts for the corresponding MMF drop [97]. As shown in this figure, the MMF drop and flux line in the slots of the rotor and stator are neglected. This model can be categorized as a model with a very coarse mesh in both the rotor and stator while the mesh granularity cannot be adjusted. Thus, the topological model requires predefining the flux path and lacks flexibility in balancing model accuracy and computational time. Therefore, in this thesis, it is referred to as the topological model.

The modeling of the airgap permeances in topological model is similar to the approach proposed in the section 2.1.1.3, in Chapter 2. Equations (2.10) to (2.14) are used to calculate the value of airgap permeances at each simulation time step. Also, the antiperiodic boundary condition is implemented through an ideal transformer with the transformation ratio of -1. The detail of using symmetry in magnetic circuits is presented in section 2.1.1.4 in Chapter 2.

As shown in Figure 3.25, only one mutator exists in the radial direction within each stator tooth to represent the effect of the coil in the permeance network of the topological model. The gain of each mutator is equal to the total number of its related coil.

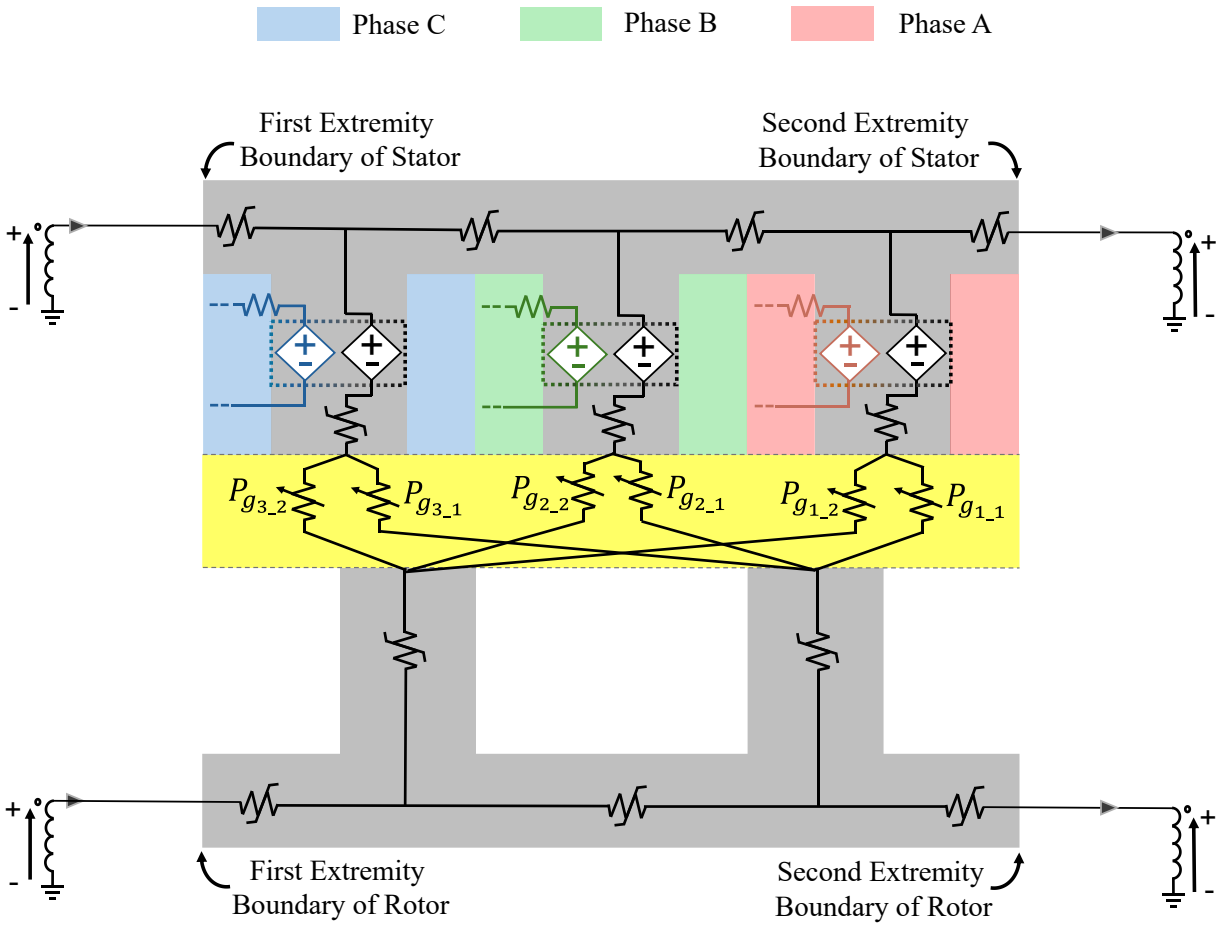


Figure 3.25 Topological circuit-based model, permeance network coupled with electric circuits

In contrast with the type-1, type-2, and type-3 lumped models, the topological model considers the effect of mutual coupling between phases while taking the nonlinear magnetic behavior of the machine's ferromagnetic core into account, as shown in Figure 3.25. As shown in this figure, there is not any assumption, like superposition, for modeling the mutual coupling while the nonlinear magnetic behavior of the teeth and yokes is modeled by the nonlinear permeances.

## 3.6 Adding leakage flux (simplified distributed model)

In the previous section, the mutual coupling was considered to the circuit-based EMT model by proposing the topological model. However, the leakage flux passing through slots of the stator and rotor is neglected in the proposed topological model.

In this section, the effect of leakage flux in the slots of the rotor and stator is added to the circuit-based EMT model. In this regard, the simplified distributed model is proposed to enhance the

accuracy and generality of the topological model. This allows the model to be employed for a wider range of transient studies. To this aim, in the proposed simplified distributed magnetic circuit, the mesh-based permeance network is used to automatically generate the equivalent magnetic circuit in the rotor and stator. Using the mesh-based approach provides flexibility to balance between the model accuracy and its computational time. Also, the airgap of the SRM is modeled by the non-meshed approach. Figure 3.26 shows the simplified distributed magnetic circuits within a quarter of the SRM's geometry. As shown in Figure 3.26, the MMF drop within the rotor and stator slots is taken into account in the proposed simplified distributed magnetic circuit. However, the slots are not modeled in the topological magnetic circuit. In addition, the proposed simplified distributed magnetic circuit models the flux path in both the radial and orthoradial directions within all parts of the stator and rotor, while the topological magnetic circuit only represents the orthoradial flux in the yokes and the radial flux in the teeth.

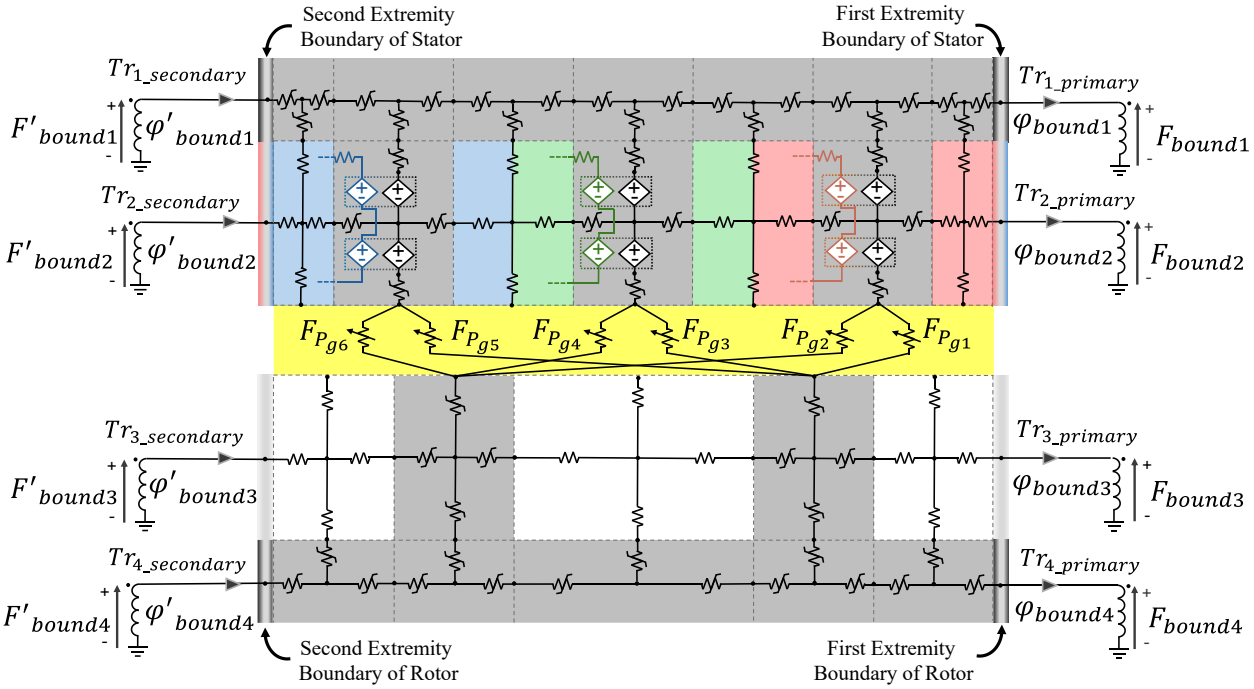


Figure 3.26 Coupled magnetic and electric circuit of the simplified distributed model of the machine

### 3.6.1 Mesh Elements Used in Simplified Distributed Magnetic Circuit

In the proposed simplified distributed model, the number of mesh divisions within the radial direction can be increased to any number. However, the number of mesh divisions in the orthoradial

direction within each tooth and slot of the rotor and stator is set to one, as shown in Figure 3.27. In this regard, this model is named the simplified distributed model.

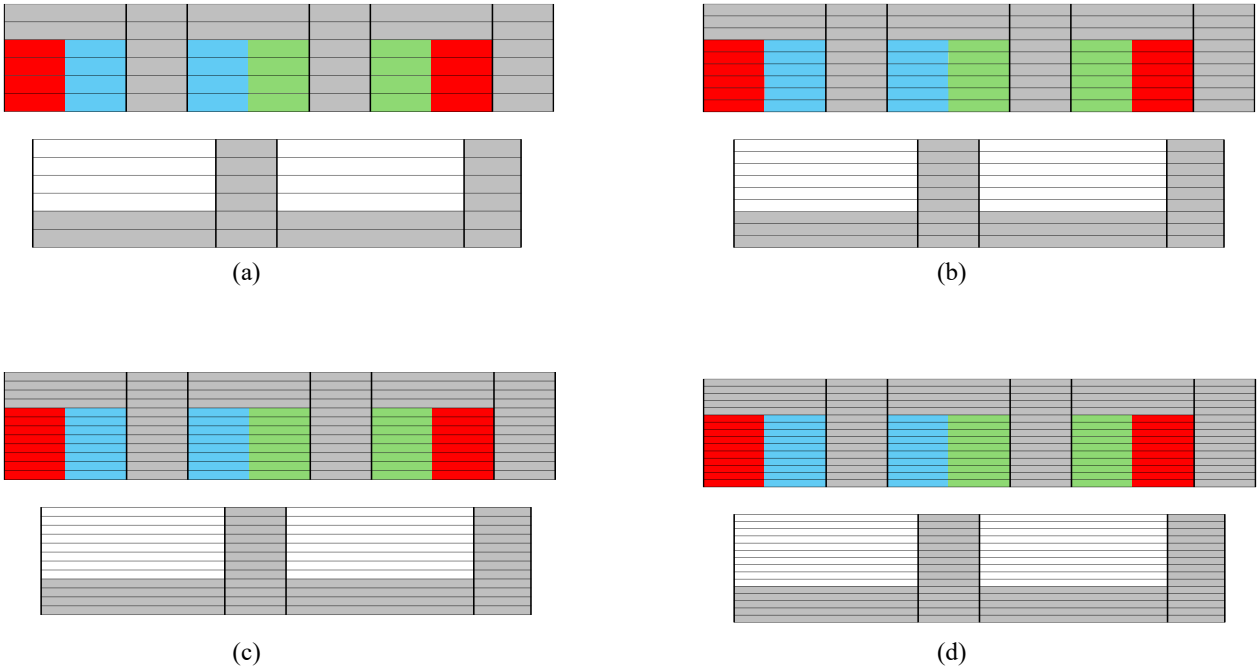


Figure 3.27 Various mesh divisions in the radial direction of the proposed simplified distributed model

As shown in Figure 3.26, nonuniform meshes are applied to the various parts of the rotor and stator. The accuracy and computational speed of the proposed simplified distributed model depend on the number of meshes. In the next chapter, we will analyze the effect of the number of meshes on the accuracy and computational performance of the proposed model.

As illustrated in Figure 3.26, the flux paths in the radial and orthoradial directions within each mesh element are modeled by four permeances connected perpendicularly at the element's centroid. The values and types of these permeances depend on the mesh element's geometrical parameters and the physical characteristics of the related area [98].

### 3.6.1.1 Values of the Permeances within Mesh Elements

Based on the machine's geometry, mesh elements with rectangular and cylindrical shapes are employed in the proposed permeance network of this machine. The rectangular mesh elements are related to the rotor and stator teeth. Figure 3.28 shows a rectangular mesh. In this figure, the flux

path in the orthoradial direction are modeled by $P_{1_{rct}}$ and $P_{3_{rct}}$ while $P_{2_{rct}}$ and $P_{4_{rct}}$ represent the flux path in the radial direction. The value of each permeance in radial and orthoradial directions of the rectangular mesh element can be calculated as [49]

$$P_{1_{rct}} = P_{3_{rct}} = \mu_{mesh} L_{stk} \frac{\left| r_{o_{mesh}} - r_{i_{mesh}} \right| / 2}{W_{mesh}} \tag{3.29}$$

$$P_{2_{rct}} = P_{4_{rct}} = \mu_{mesh} L_{stk} \frac{W_{mesh}}{\left| r_{o_{mesh}} - r_{i_{mesh}} \right| / 2} \tag{3.30}$$

where, $\mu_{mesh}$ is the permeability of the mesh element, $L_{stk}$ represents the machine stack length, $r_{i_{mesh}}$ express the inner radius of the mesh element, $r_{o_{mesh}}$ is the outer radius of the mesh element, and $W_{mesh}$ represents the mesh element width.

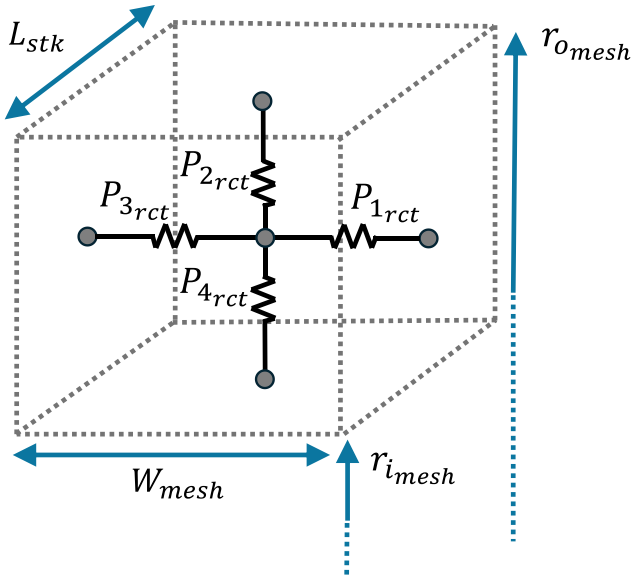


Figure 3.28 Rectangular mesh element in the proposed permeance network

The mesh elements associated with the slots and yokes of the rotor and stator have a cylindrical shape. Figure 3.29 shows a cylindrical mesh element where its angle is represented by $\theta_{mesh}$. Each permeance of this mesh element can be calculated as [21]

$$P_{1_{cyl}} = P_{3_{cyl}} = \mu_{mesh} L_{stk} \frac{\ln\left(\frac{r_{o_{mesh}}}{r_{i_{mesh}}}\right)}{0.5\theta_{mesh}} \tag{3.31}$$

$$P_{2_{cyl}} = \mu_{mesh} L_{stk} \frac{\theta_{mesh}}{\ln\left(\frac{r_{o_{mesh}}}{r_{avg_{mesh}}}\right)} \tag{3.32}$$

$$P_{4_{cyl}} = \mu_{mesh} L_{stk} \frac{\theta_{mesh}}{\ln\left(\frac{r_{avg_{mesh}}}{r_{i_{mesh}}}\right)} \tag{3.33}$$

$$r_{avg_{mesh}} = \frac{r_{o_{mesh}} + r_{i_{mesh}}}{2} \tag{3.34}$$

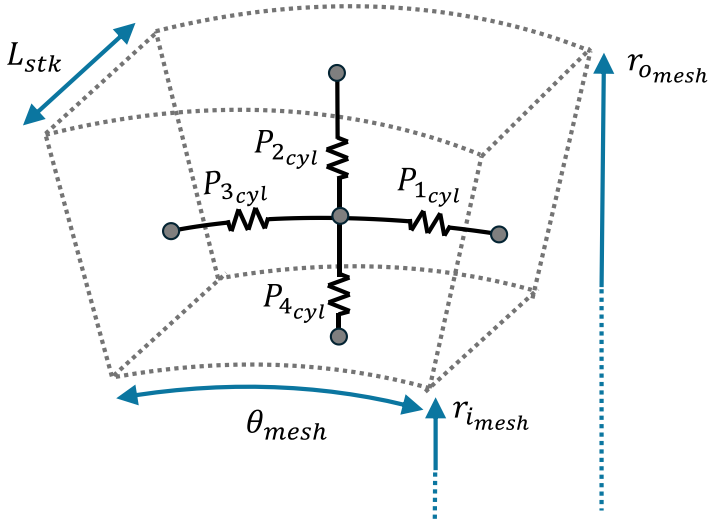


Figure 3.29 Cylindrical mesh element in the proposed permeance network

### 3.6.1.2 Types of Mesh Elements

As shown in Figure 3.26, three types of mesh are employed in the permeance network of the proposed simplified distributed model. Figure 3.30 shows these three types of mesh. The permeability of the rotor and stator slots is equal to the air permeability, which is a constant value. Thus, the mesh elements associated with the slots consist of linear permeances, as shown in Figure 3.30 (a).

The mesh elements within the yoke of the stator and rotor, as well as the rotor teeth, consist only of nonlinear permeances, as shown in Figure 3.30 (b). These nonlinear permeances are implemented by their Norton companion model presented in section 2.1.1.2 in Chapter 2. The length and surface area of each nonlinear permeance within a mesh element depend on the geometrical characteristics of that mesh element. It is worth noting that the shape of mesh elements within the teeth of the stator and rotor is rectangular, while those in the yoke of the stator and rotor are cylindrical.

The effect of the MMF produced by the stator coils is considered through mutators located in the radial direction within the mesh elements associated with the stator teeth, as shown in Figure 3.30 (c). It is worth noting that the mesh elements in the stator teeth have a rectangular shape.

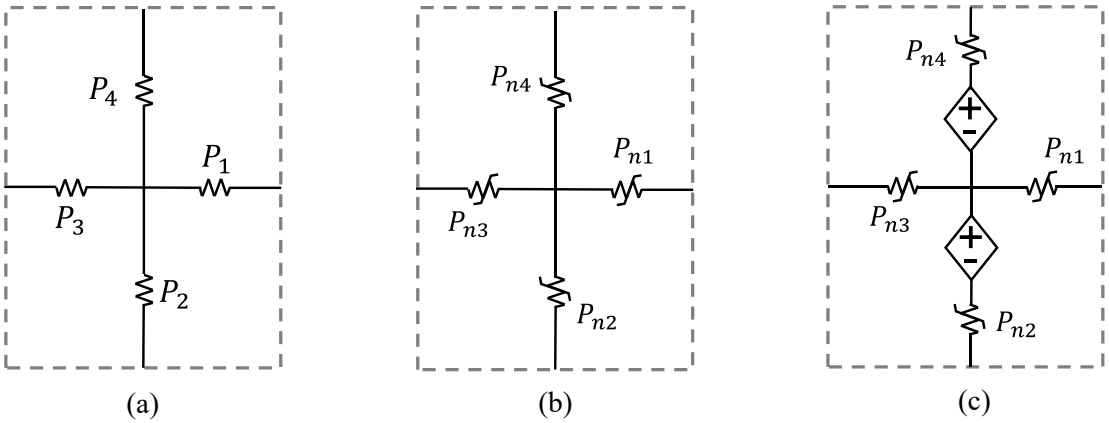


Figure 3.30 Various type of mesh elements used in the permeance network of the proposed simplified distributed model, mesh elements within (a) rotor and stator slots, (b) stator and rotor yokes and rotor teeth, (c) stator teeth

As shown in Figure 3.26, the proposed simplified distributed magnetic circuit uses the non-meshed to model the airgap. In this regard, the value of the airgap permeances at each simulation time step can be calculated by equations (2.10) to (2.14). Further details are presented in Section 2.1.1.3 in Chapter 2.

## 3.7 Adding all local magnetic phenomena (distributed model)

In the previous section, the simplified distributed model was proposed. In this model, using the mesh-based permeance network enabled flexibility to balance between the model accuracy and its computational time. It also achieves higher accuracy compared to the topological and lumped

models. However, in some transient studies, a more detailed magnetic model of the electric machine is required. For example, studying transient phenomena happening inside the machine or assessing their impact on local magnetic behavior, like local saturation, necessitates a more detailed magnetic model that can account for all details of the machine's magnetic behavior. Such magnetic details can be considered by dividing various parts of the machine into finer elements than those used in the simplified distributed model. To this end, the distributed magnetic circuit model is proposed in this section.

The distributed magnetic circuit model uses the same methodology as the simplified distributed model. In both models, the magnetic behavior of the rotor and stator is represented by a mesh-based permeance network, while the airgap is modeled using a non-meshed approach. Similar to the simplified distributed model, any number of mesh divisions can be used in the radial direction. However, in contrast to the simplified distributed model, the distributed model allows using any number of mesh divisions in the orthoradial direction, whereas in the simplified distributed model, this number was limited to one within each tooth and slot. For instance, Figure 3.31 shows the discretized geometry of the SRM with various mesh divisions in the orthoradial direction. In this figure, the teeth, slots, and yokes of the rotor and stator are divided into three divisions in the radial direction. In the next chapter, the effect of mesh divisions in the radial and orthoradial directions on the model's accuracy and computational speed is analyzed.

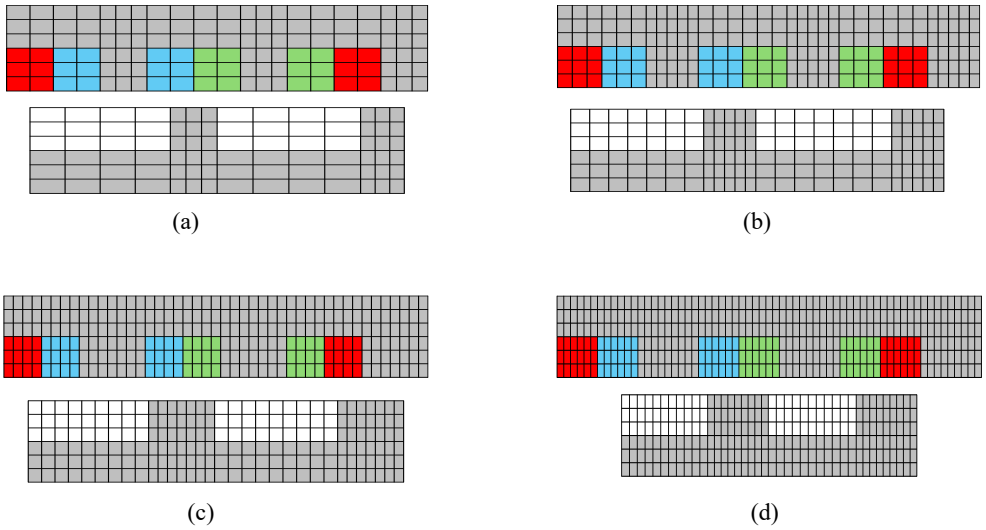


Figure 3.31 Various mesh divisions in the orthoradial direction of the proposed distributed model

To have a more detailed illustration of the proposed distributed model, Figure 3.32 (a) shows the meshed geometry of the studied 12/8 SRM, while the coupled electric and magnetic circuits within meshes in stator and rotor teeth and their adjacent slots meshes are shown in Figure 3.32 (b). In this figure, the magnetic and electric circuits are in black and purple, respectively. As shown in this figure, the mesh elements consist of four permeances perpendicularly connected at the element centroid, similar to the simplified distributed model.

As shown in Figure 3.32, four types of mesh elements are utilized in the permeance network of the proposed distributed model. The mesh elements that relate to the rotor slots consist of linear permeances, as shown in Figure 3.33 (a). The mesh elements within the stator slots include linear permeances, while the effect of the coil's MMF is represented through mutators in the radial direction of each mesh element, as illustrated in Figure 3.33 (b). Figure 3.33 (c) shows the mesh elements associated with the stator and rotor yokes, which include nonlinear permeances to account for the nonlinear behavior of the ferromagnetic core. Finally, the mesh element within the stator teeth consists of the nonlinear permeance in radial and orthoradial directions and mutators in the radial direction, as shown in Figure 3.33 (d).

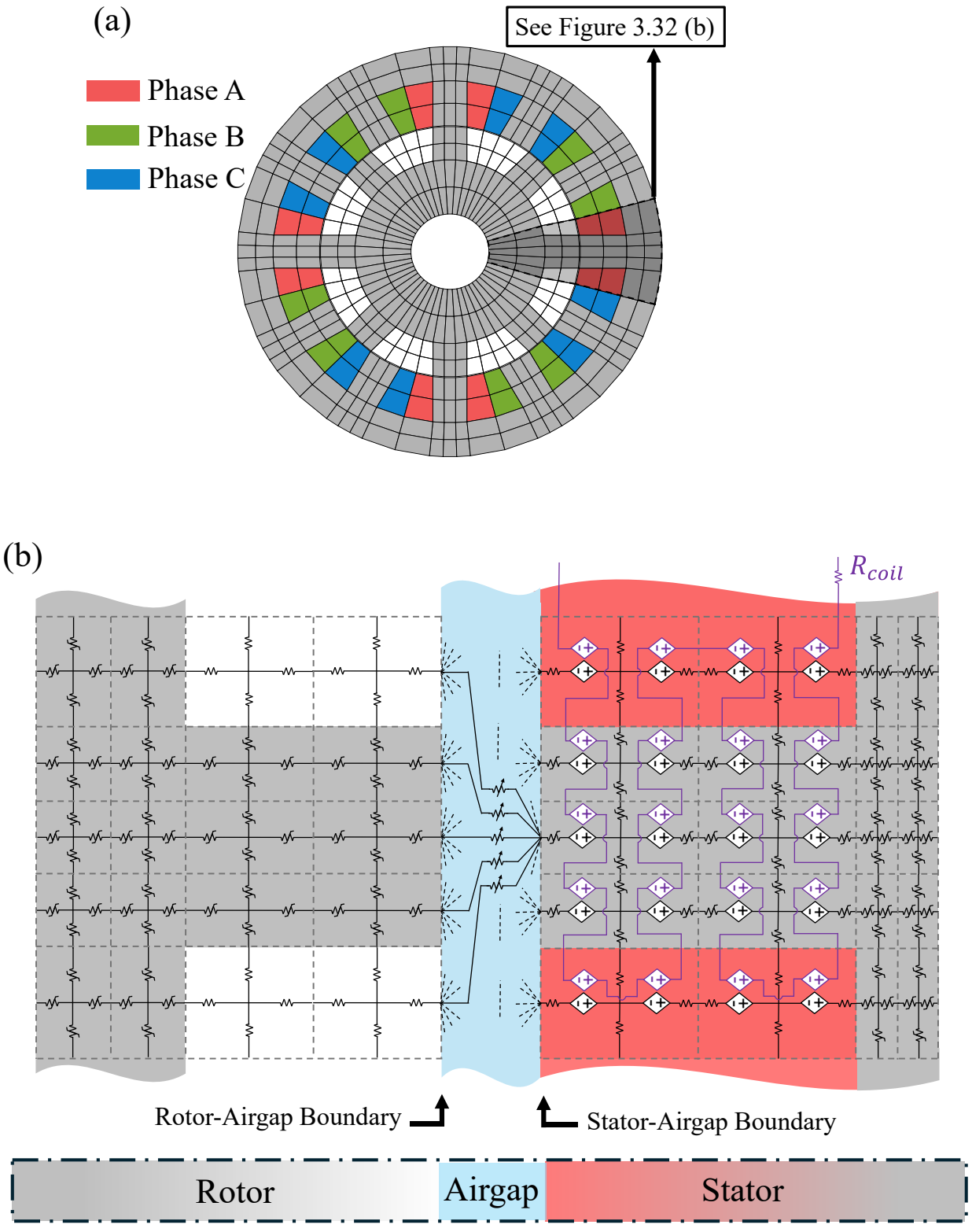


Figure 3.32 Distributed circuit-based EMT model of a 12/8 SRM, (a) meshed geometry, (b) coupled magnetic and electric circuit

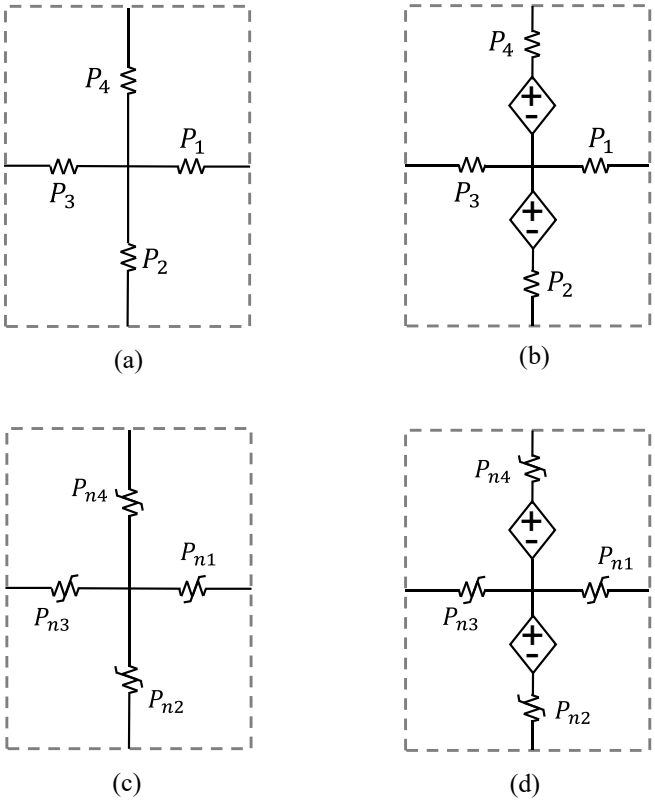


Figure 3.33 Various type of mesh elements used in the permeance network of the proposed distributed model, mesh elements within (a) rotor slots, (b) stator slots, (c) stator and rotor yokes and rotor teeth, (d) stator teeth

## 3.8 Conclusion

In this chapter, the circuit-based EMT models of SRMs are proposed. We start from the most basic model that neglects the space harmonics, nonlinear magnetic behavior of the machine, and mutual coupling between phase windings. Step by step, we added space harmonics, nonlinear magnetic behaviors, and mutual coupling effect while we finally proposed a circuit-based EMT model that accounts for all detailed magnetic phenomena. At each step, a circuit-based EMT model is proposed. The most basic model is named type-1 lumped model. By adding the effect of space harmonics using variable permeances, type-2 lumped model was developed. In type-3 lumped model, the effect of nonlinear magnetic behavior of the ferromagnetic core is considered while the modeling of airgap is similar to type-2 lumped model. To consider the effect of mutual coupling, topological model was proposed. In the topological model, the effect of flux in the machine's slots is neglected. To enhance the accuracy, the simplified distributed model was proposed. In this

model, the mesh-based permeance network is used to represent the magnetic behavior of the stator and rotor while the airgap was modeled by the non-meshed approach. In this model, the number of mesh divisions in the orthoradial direction was limited. However, to account for all detailed and local magnetic phenomena happening inside the machine, the distributed model is proposed. It used the same methodology as the simplified distributed model but it does not have limitation in number of mesh divisions. This allows to account all details of the machine.

# CHAPTER 4 VALIDATION AND COMPARISON OF THE PROPOSED MODELS

In the previous section, various circuit-based EMT models for the studied SRM was proposed. In this section, the proposed models is verified by the FEM-based model. Furthermore, the performance of the proposed models is compared in terms of computational time and accuracy.

To this end, all proposed lumped models are used to simulate the case study SRM. It is useful to recall that the case study is a 3-phase SRM with 12 stator teeth and 8 rotor teeth. The cross-sectional view of this machine is shown in Figure 1.3. The SRM models are integrated into the detailed circuit-based representation of the asymmetric bridge converter and its control system, with a simultaneous solution.

The description regarding the EMT solver and also the FEM-based model is described in section 1.3.3 in Chapter 1.

## 4.1 Verification of Lumped models

This section aims to compare the performance of the proposed lumped models. To assess the accuracy of the proposed models, the error between electromagnetic torque obtained by FEM-based and circuit-based models are calculated. This error is defined as the difference between the absolute values of the mean electromagnetic torque, computed over the entire signal, obtained using the FEM-based method and the proposed circuit-based method. Throughout this thesis, the error between the circuit-based model and the FEM-based model is calculated in the same way.

Figure 4.1 compares the performance of the proposed lumped circuit-based models. As shown in this figure, the type-1 lumped model is the fastest, with a CPU time of 3.02 seconds. However, its accuracy is not acceptable, as the average torque calculated by this model differs 18.2% from the value obtained using the FEM-based model. By accounting for the machine's space harmonics, caused by the stator and rotor slots, within the magnetic circuit through the use of variable permeances that accurately model the saliency effects in both the stator and rotor, the accuracy of the type-2 lumped model has been enhanced compared to the type-1 model. In the case of the type-2 lumped model, the calculated average torque shows a difference of 8.4% compared with the result obtained from the FEM-based model. However, this improvement increased the CPU time to 4 seconds. Finally, the type-3 lumped model, which incorporates both the nonlinear behavior of the

ferromagnetic core and the machine's saliency, demonstrates acceptable accuracy. The average torque calculated by this model differs 4.64% from the value obtained using the FEM-based model. It is worth noting that, based on engineering judgment and experience, an error below 5% between the FEM-based models and the proposed models is acceptable.

Among the proposed lumped models, the type-3 model is the slowest in terms of computational performance. The higher computational time of the type-3 lumped model rather than the other proposed lumped models was expected, as the nonlinear behavior of the ferromagnetic core is represented by nonlinear permeances, which require an iterative solution process for the main system equations.

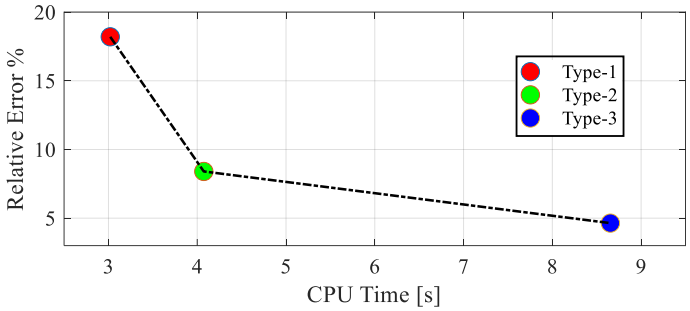


Figure 4.1 Comparison of the performance of the proposed lumped circuit-based models

Also, Figure 4.2 shows the comparison of the accuracy and computational time of the proposed lumped models in the bar chart.

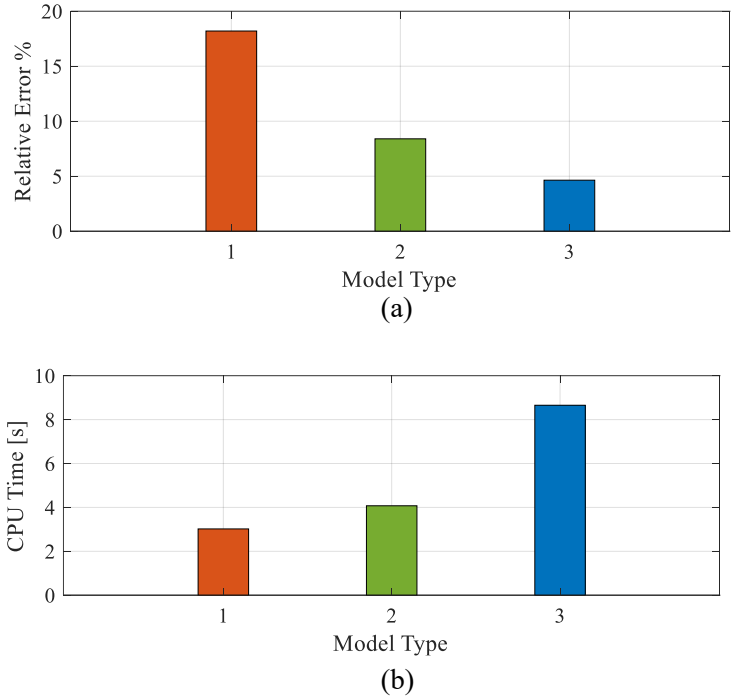


Figure 4.2 Comparison of the performance of the proposed lumped circuit-based models by bar chart, (a) relative error in average torque, (b) CPU time

As shown in the comparison study, among the proposed lumped models, type-3 lumped model is the only model that provides an acceptable accuracy. In this regard, we used this model to simulate the case-study SRM operating at 2500 rpm, with the reference peak phase current $I_{ref}$ set to 20 A.

Figure 4.3 shows the phase current of the studied SRM as calculated by the proposed type-3 lumped model and the FEM-based model. In the figure's legends, the FEM-based model is referred to as CoSim-FEM. As illustrated in the figure, the type-3 lumped circuit-based model demonstrates acceptable accuracy.

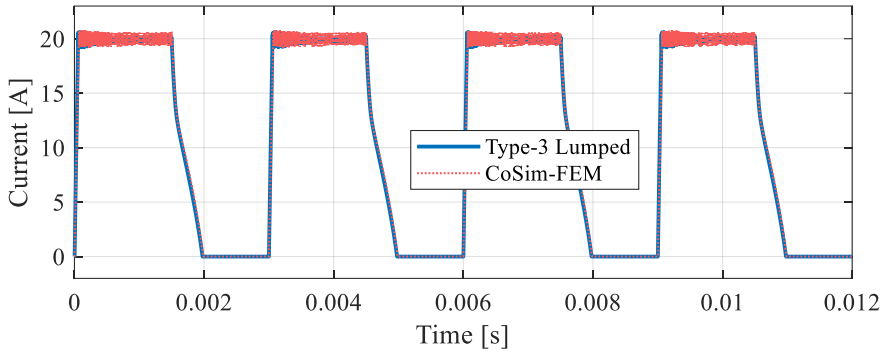


Figure 4.3 The phase current of the studied SRM simulated by the type-3 lumped circuit-based model and FEM-based model

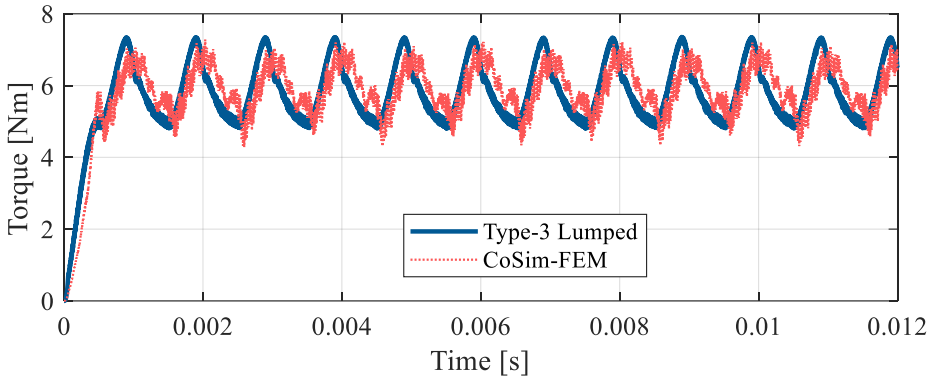


Figure 4.4 The electromagnetic torque of the studied SRM simulated by the type-3 lumped circuit-based model and FEM-based model

The electromagnetic torque of the studied SRM, calculated by the proposed type-3 lumped circuit-based model and the FEM-based model, is shown in Figure 4.4. As illustrated in this figure, the type-3 lumped circuit-based model provides acceptable accuracy, with a 4.64% difference in the average torque compared to the FEM-based model. However, it can be observed that this model does not capture the torque ripple and oscillations with high accuracy. The deviation of the torque calculated by the type-3 lumped model from the FEM-based model was expected, as the type-3 model employs a significantly lower number of magnetic equivalent elements than those used in the FEM-based model.

## 4.2 Topological Model

To evaluate the performance of the topological circuit-based model shown in Figure 3.25, we compared the phase current and torque of the studied SRM calculated by the proposed topological model and the FEM-based model.

Figure 4.5 presents a comparison between the current of phase A obtained from the proposed topological model and the FEM-based model. The phase current follows the corresponding control commands (phase pulses) while the inductive nature of the SRM caused a tracking error at the turn-off angle in both models. The currents in phases B and C exhibit the same waveform as phase A, with electrical phase shifts of 120° and 240°, respectively.

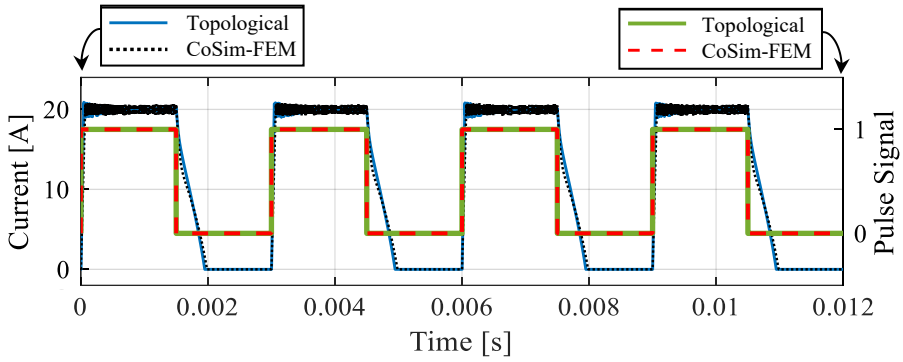


Figure 4.5 SRM's phase A current calculated by the proposed topological model and FEM-based model

The electromagnetic torque calculated by the proposed topological model and the FEM-based model are compared in Figure 4.6. As shown, the proposed topological model achieves acceptable accuracy. The average torque calculated by the topological model differs by 4.15% from that obtained from the FEM-based model. However, the torque waveform calculated by the FEM-based model exhibits more high-frequency oscillations. This discrepancy can be attributed to two factors. First, the proposed topological model uses the co-energy method to calculate the torque, while the FEM-based method uses the Maxwell Stress Tensor method. Second, the FEM-based method uses a meshed approach in all parts of the machine, while the proposed circuit-based topological model uses a limited number of magnetic equivalent elements.

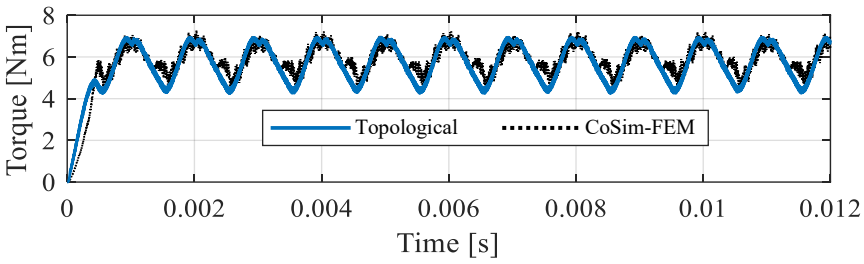


Figure 4.6 Electromagnetic torque of the studied SRM calculated by the proposed topological model and FEM-based model

## 4.3 Simplified Distributed Magnetic Circuit

As mentioned, the accuracy and computational time of the proposed simplified distributed model depend on the mesh granularity of the permeance network within the stator and rotor. Thus, we analyze the effect of the mesh numbers on the computational time and accuracy of the proposed simplified distributed model

### 4.3.1 Mesh Analysis

To analyze the effect of mesh divisions, the average torque value and the magnetic flux density at the center of the stator tooth aligned with the rotor tooth serve as the metrics for the mesh assessment. The effect of mesh element numbers on the computational time and relative error of the selected metrics is shown in Figure 4.7. In this assessment, SRM rotates at a fixed speed for 12 ms, using a time step of 1 $\mu$s. As illustrated in Figure 4.7, increasing the number of mesh elements reduces the relative error in both the average torque and the magnetic flux density, but it significantly increases the computational time. Therefore, based on the required computational speed and accuracy in this study, 72 mesh elements are used in the following analysis to achieve a well-balanced trade-off between computational time and accuracy.

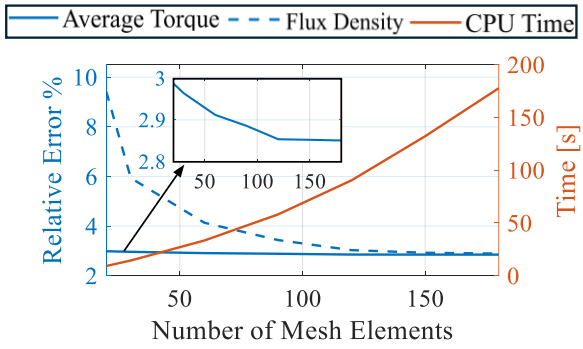

Figure 4.7 Effect of mesh elements number on the computational time and accuracy of simplified distributed model

### 4.3.2 Effect of Using Symmetry

In the proposed simplified model, we used symmetry in which the antiperiodic boundary condition is applied. Thus, this subsection aims to evaluate the effect of using symmetry in speeding up the simulation process in the simplified distributed model and FEM-based model. In this regard, Figure 4.8 shows the effect of using symmetry (modeling a quarter of the machine) on the computational time of the proposed simplified distributed circuit-based EMT model and FEM-based model. In this figure and other figures in this thesis, the simplified distributed model is referred to as S-CBEMT.

As illustrated in Figure 4.8, simulating only a quarter of the machine reduces the computational time of the proposed simplified distributed model by more than 14 times compared to modeling the full geometry. However, in the case of the FEM-based model, using symmetry only speeds up the simulation by about 1.3 times compared to modeling the full geometry. Therefore, modeling a quarter of the machine significantly accelerates the proposed simplified distributed model simulation compared to the FEM-based model.

The smaller speed-up in computational time for the FEM-based model is due to the computational burden caused by remeshing at each time step and co-simulation, as using symmetry does not eliminate these computational burdens. In contrast, the proposed simplified distributed model benefits from a simultaneous solution of the drive system components and maintaining the same magnetic circuit topology throughout the entire simulation, thanks to the non-meshed approach in the airgap.

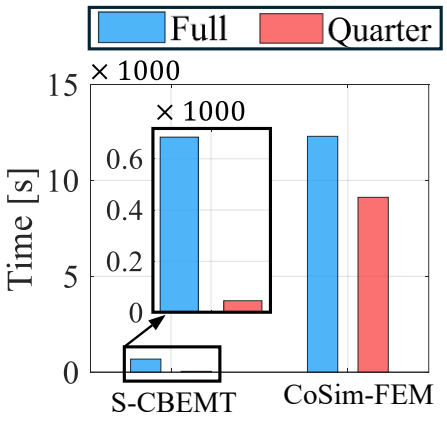

Figure 4.8 Effect of using symmetry on the computational time of simplified distributed circuit-based model and FEM-based model

### 4.3.3 Verification

In this part, we analyze the performance of the studied SRM while it is rotating at a fixed speed of 2500 rpm, and the hysteresis current control maintains the phase current at 20 A. Figure 4.9 shows the pulse and current of phase A. As shown in this figure, in both models, the phase current follows the phase pulses, but both models show tracking error at the turn-off angle $\theta_{off}$ because of the SRM's inductive nature. It is worth mentioning that the currents of phases B and C are similar to the current of phase A with 120 and 240 electrical phase shifts.

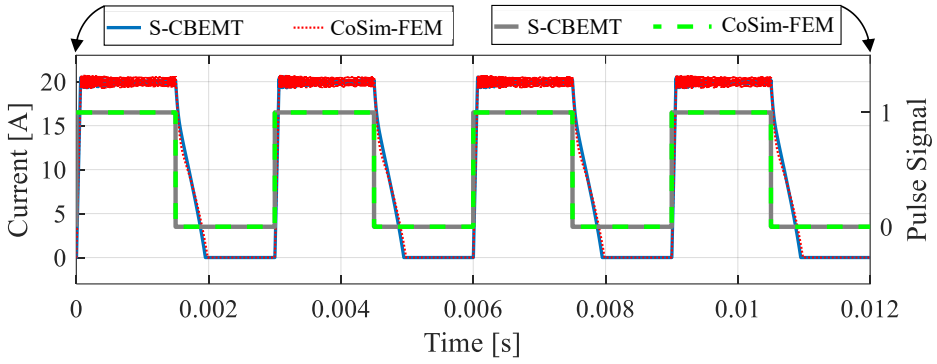


Figure 4.9 SRM's phase pulse and phase current obtained by simplified distributed model and FEM-based model while SRM rotates at 2500 rpm

Figure 4.10 shows the electromagnetic torque of the SRM obtained from both the proposed simplified distributed model and the FEM-based model. The results indicate that the simplified distributed circuit-based EMT model delivers acceptable accuracy. The FEM-based model, as previously discussed, displays more high-frequency oscillations.

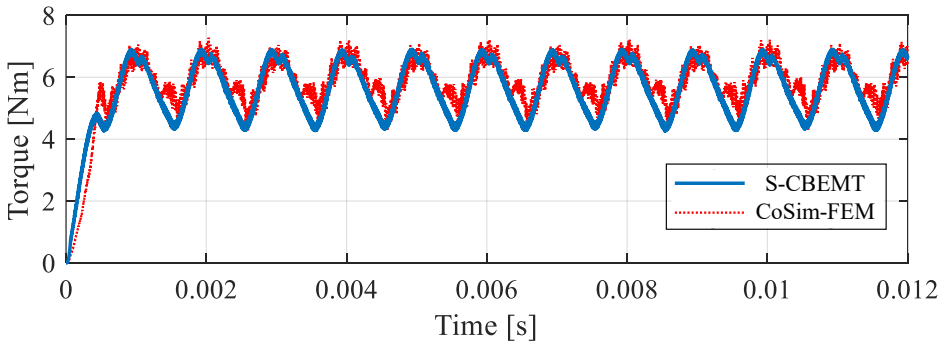

Figure 4.10 SRM's electromagnetic torque obtained by by simplified distributed model and FEM-based model while SRM rotates at 2500 rpm

## 4.4 Distributed Magnetic Circuit

In this section, we aim to verify the proposed distributed circuit-based model as well as analyzing the effect of using various analytical function for airgap permeances and number of mesh divisions on the model's performance.

### 4.4.1 Airgap Modeling

As shown in Figure 3.32, each node on the stator-airgap boundary is connected to all nodes on the rotor-airgap boundary through variable permeances in airgap. Similar to the all other proposed models in the previous chapter, the value of airgap permeances within the distributed model is calculated by an analytical functions at each simulation time-step. However, due to the higher number of mesh elements within the orthoradial direction of the SRM, high fringing and leakage flux will be accurately modeled in the proposed distributed circuit-based model. In this regard, the effect of using various analytical functions available in the literature, including cosine [49], [53] exponential [51], [4], [54], linear functions [55], [56], [57], and bell-shaped [52], [58] functions, on the accuracy of the proposed distributed magnetic circuit is evaluated. To this aim, the inductance-angle characteristics of the studied SRM in 10 A and 20 A phase currents are shown in Figure 4.11 (a) and Figure 4.11 (b), respectively. In these figures, the inductance-angle characteristics are calculated by the proposed distributed model and verified by the FEM-based model. As presented in Figure 4.11 (a) and Figure 4.11 (b), using all the mentioned airgap functions result in accurate results in the non-overlapped regions, while the exponential and bell-shaped functions provided higher accuracy in the partially and fully overlapped regions. Moreover, the phase inductance at the fully aligned position (22.5º) decreases with increasing phase current due to saturation of the ferromagnetic core. Thus, in the following studies in this thesis, the value of the airgap permeance the partial and non-overlapped regions are calculated using exponential functions in the distributed model.

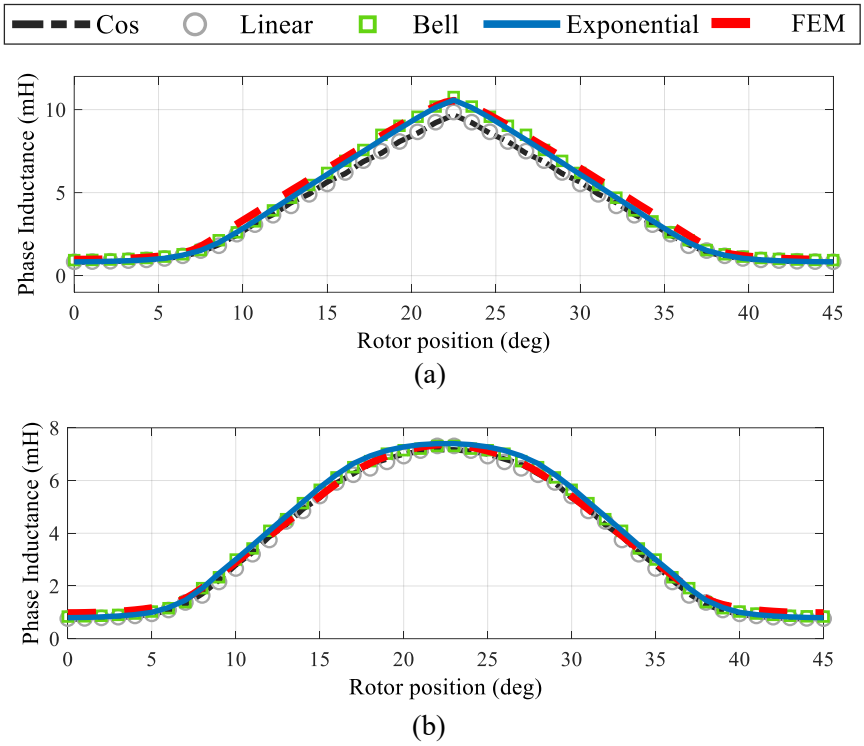


Figure 4.11 Phase inductance profile: comparison of the effect of using various airgap analytical functions on the phase inductance profile and validation by FEM, (a) at 10 A and (b) at 20 A

### 4.4.2 Mesh Analysis

The first step in carrying out the time-domain study involves defining an appropriate number of mesh divisions of the proposed distributed circuit-based model. This step is crucial, as the granularity of the mesh affects the model's accuracy and computational time. In this context, a comprehensive mesh analysis is performed to see the effect of mesh divisions on the model's accuracy and computational time. In this regard, we selected various cases with different numbers of mesh divisions in radial and orthoradial directions. In this regard, we selected six groups of cases to evaluate the effect of the number of mesh divisions in the orthoradial direction. The number of mesh divisions in the orthoradial direction increases progressively from Group 1 to Group 6. Group 1 has the fewest number of mesh divisions in the orthoradial direction, while Group 6 has the highest number of mesh divisions in the orthoradial direction. To assess the effect of the number of mesh divisions in the radial direction, each group consists of four cases. In these cases, the number of mesh division in the radial direction within the teeth and yoke of the rotor and stator are

set to 1, 2, 3, and 4 in Case 1, Case 2, Case 3, and Case 4, respectively. The selected six groups are shown in Figure 4.12 to Figure 4.17. As shown in this figure, each group consists of four cases.

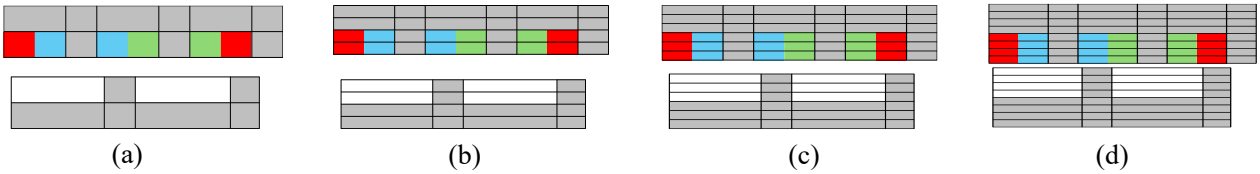


Figure 4.12 Meshed geometry of group 1, (a) case 1, (b) case 2, (c) case 3, and (d) case 4

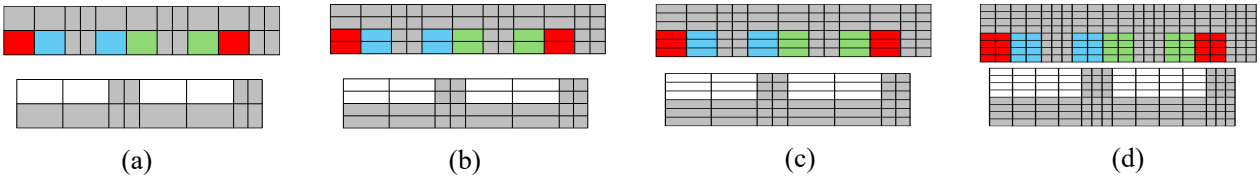


Figure 4.13 Meshed geometry of group 2, (a) case 1, (b) case 2, (c) case 3, and (d) case 4

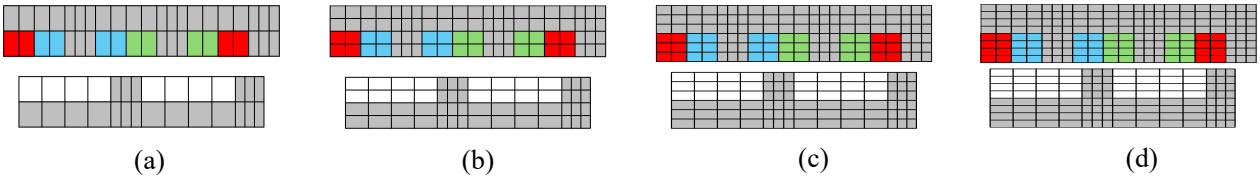


Figure 4.14 Meshed geometry of group 3, (a) case 1, (b) case 2, (c) case 3, and (d) case 4

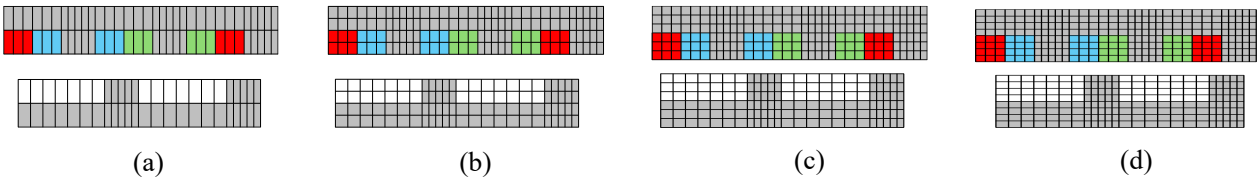


Figure 4.15 Meshed geometry of group 4, (a) case 1, (b) case 2, (c) case 3, and (d) case 4

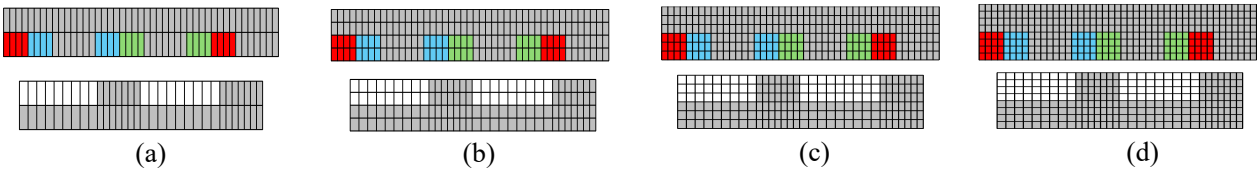


Figure 4.16 Meshed geometry of group 5, (a) case 1, (b) case 2, (c) case 3, and (d) case 4

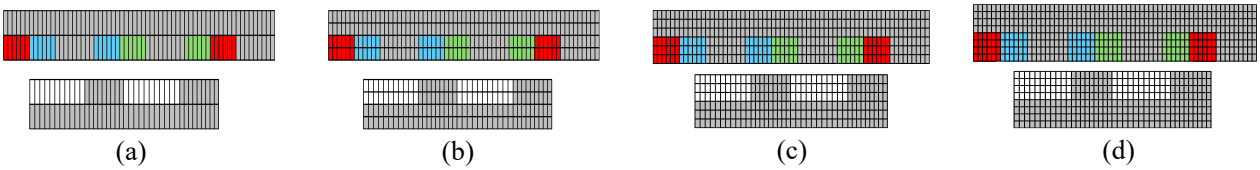


Figure 4.17 Meshed geometry of group 6, (a) case 1, (b) case 2, (c) case 3, and (d) case 4

To assess the accuracy of the proposed distributed circuit-based model with the mesh divisions shown in Figure 4.12 to Figure 4.17, the average value of the electromagnetic torque is used as the reference metric. In this regard, the relative error between the average torque value obtained by the FEM-based model and the proposed distributed circuit-based model is calculated for each case within the defined groups. Figure 4.18 presents the relative error and CPU time for the cases within the six defined groups. For more clarity, Figure 4.19 plots the same data in a logarithmic scale.

As shown in Figure 4.18 and Figure 4.19, the number of mesh divisions in the orthoradial direction has a significant impact on the accuracy of the proposed distributed circuit-based model. As shown, the relative error in group 1 is around 15%, which is not acceptable. By increasing the number of mesh divisions in the orthoradial direction, the relative error is significantly reduced. It decreased to approximately 5% in group 2, between 4% and 3% in groups 3 and 4, and below 2% in groups 5 and 6. Moreover, increasing the number of mesh divisions in the radial direction improved the model's accuracy, whereas its impact is less significant than the impact of the number of mesh divisions in the orthoradial direction. However, its important to have a sufficient number of mesh divisions in the radial direction to achieve acceptable accuracy in the local magnetic behavior of the machine.

To have a more detailed analysis of the impact of mesh division in the orthoradial direction on the model's accuracy, we analyze the torque waveform of the studied SRM calculated by the FEM-based model and the proposed distributed circuit-based model in groups 3 and 6 (see Figure 4.14 and Figure 4.17) while the mesh division in the radial direction within the teeth and the yoke is one. It is worth mentioning that the electromagnetic torque is calculated using co-energy method. The details of torque calculation using co-energy method is presented in Chapter 2, section 2.1.3.

As shown in Figure 4.20 and Figure 4.21, both cases show acceptable accuracy in calculating the average value of the electromagnetic torque. .However, the electromagnetic torque calculated by

the distributed circuit-based model with the fine mesh is more accurate in representing the torque ripple and oscillations.

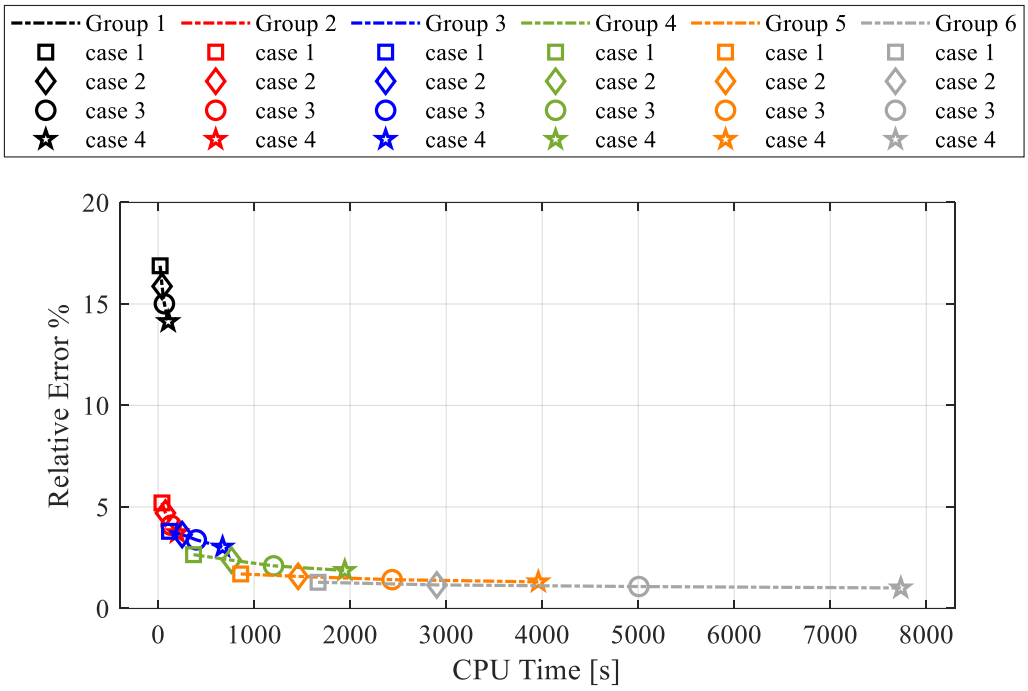


Figure 4.18 Effect of the number of mesh divisions in radial and orthoradial direction on the accuracy and computational time of the proposed distributed circuit-based model

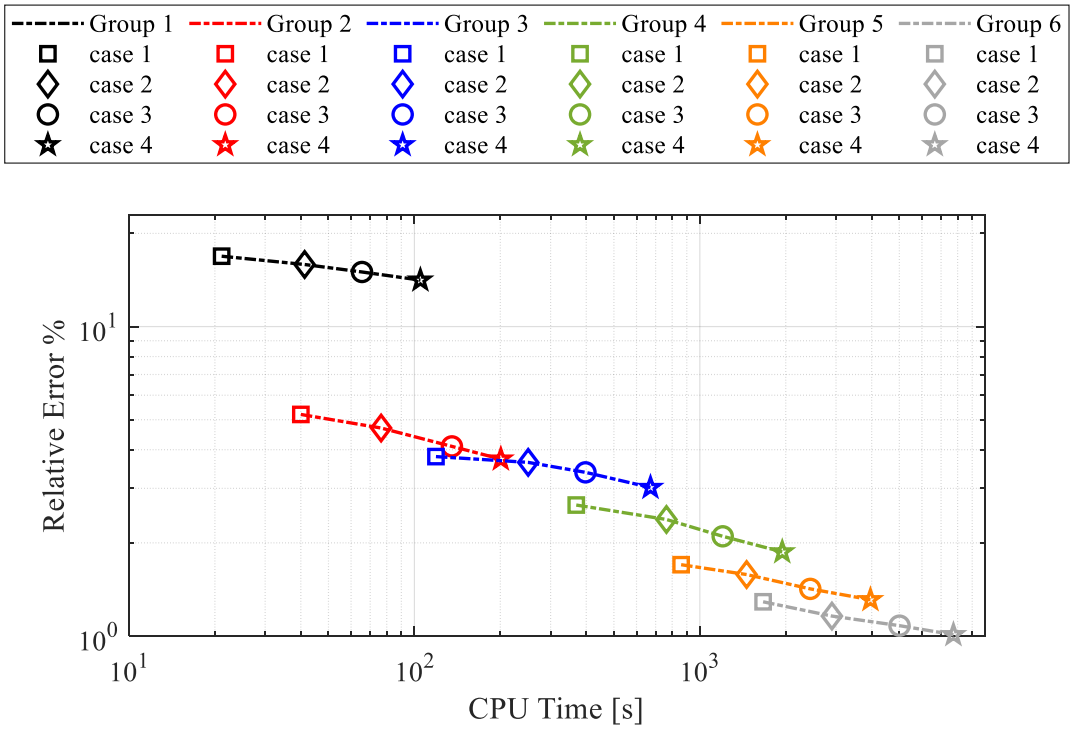

Figure 4.19 Effect of the number of mesh divisions in radial and orthoradial direction on the accuracy and computational time of the proposed distributed circuit-based model shown in logarithmic scale

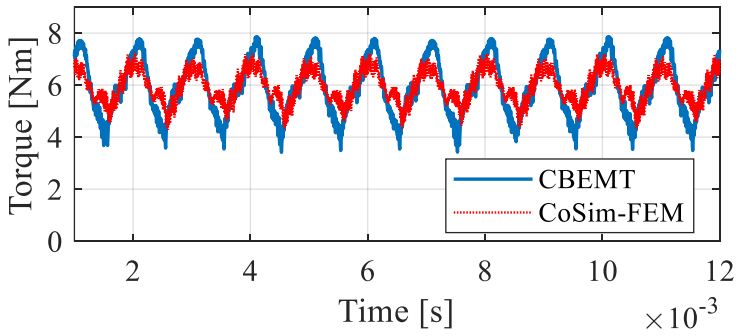


Figure 4.20 Electromagnetic torque calculated by the proposed distributed circuit-based model for group 3, with radial mesh divisions of one within the teeth and the yoke

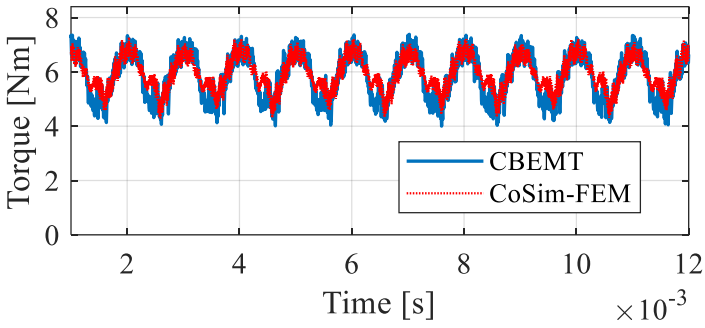


Figure 4.21 Electromagnetic torque calculated by the proposed distributed circuit-based model for group 6, with radial mesh divisions of one within the teeth and the yoke

### 4.4.3 Verification

For the following simulations, we used 980 mesh elements in the proposed distributed circuit-based EMT model, as shown in Figure 4.22. Also, we employed a fine mesh with 12030 triangular elements in CoSim-FEM.

In this analysis, the SRM is rotating at a fixed speed of 2500 rpm. The hysteresis current control is used to maintain the phase current in its reference peak value (20 A). The current and pulses of phases A, B, and C are shown in Figure 4.23 (a), Figure 4.23 (b), and Figure 4.23 (c), respectively. In these figures, the results corresponding to the proposed distributed circuit-based model are labeled as CBEMT.

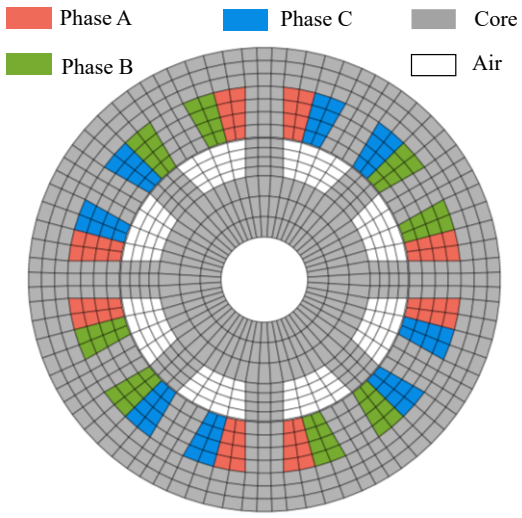


Figure 4.22 Meshed geometry of the studied 12/8 SRM

As illustrated in these figures, the proposed distributed circuit-based model and CoSim-FEM simulate identical phase pulses, resulting in a similar sequence of phase excitations in both models. IGBTs in each phase are closed when their pulse signal is 1. There is a good agreement between the phase currents calculated by the proposed distributed circuit-based model and CoSim-FEM. In both models, the phase currents tracked their control command (phase pulses), which shows the correctness of the coupling between the magnetic, electric, and control circuits. The inductive nature of the SRM caused a tracking error at the turn-off angle $\theta_{off}$ in both models. The close agreement between the current waveforms of the proposed distributed circuit-based model and CoSim-FEM highlights the capability of the proposed distributed circuit-based model to accurately accommodate current transients.

The electromagnetic torque calculated by the proposed distributed circuit-based model and CoSim-FEM are compared in Figure 4.24. This comparison shows that the proposed distributed circuit-based model estimates the torque with satisfactory accuracy.

To evaluate the distribution of the magnetic flux within the machine, the phase peak current is injected into phase A windings and the distribution of the magnetic flux density in the machine's geometry is calculated by the proposed distributed circuit-based model and FEM model. In this regard, Figure 4.25 (a) and Figure 4.25 (b) respectively show the magnetic flux density calculated by the proposed distributed circuit-based model and FEM model. As shown in these figures, there is a close agreement between the magnetic flux density distribution resulting from the proposed

distributed circuit-based model and FEM. The proposed distributed circuit-based model accurately modeled the saturation of the ferromagnetic core. The magnetic flux density distribution differs between the proposed distributed circuit-based model and FEM simulations only at the teeth edges. This discrepancy arises from assuming a rectangular shape for the teeth and utilizing rectangular mesh in the proposed distributed circuit-based model.

In terms of computational performance, both models were simulated for 12 ms with the simulation time-step of 1 μs while the proposed distributed circuit-based model is more than nine times faster than CoSim-FEM. Table 4-1 compares the CPU time of each method.

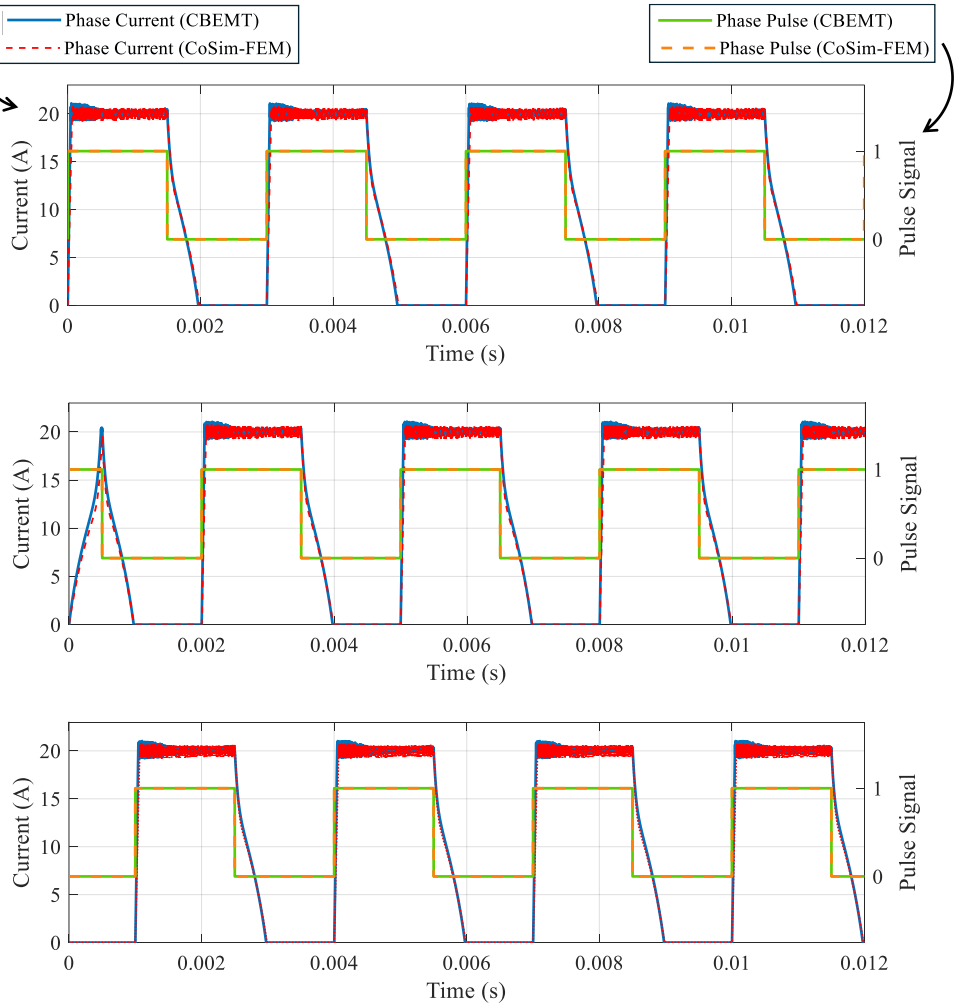


Figure 4.23 Phase pulses and phase currents of the studied SRM motor drive, (a) phase A, (b) phase C, and (c) phase C

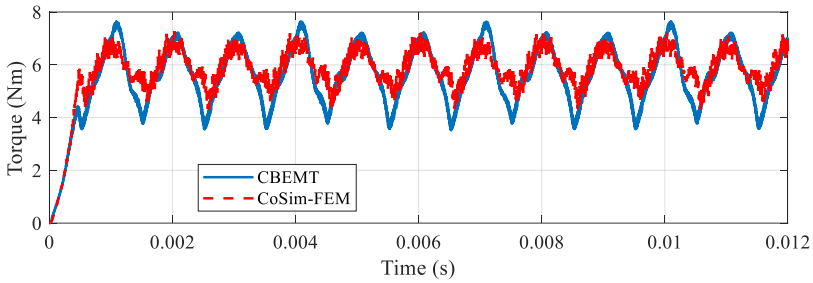


Figure 4.24 Electromagnetic torque of the studied SRM

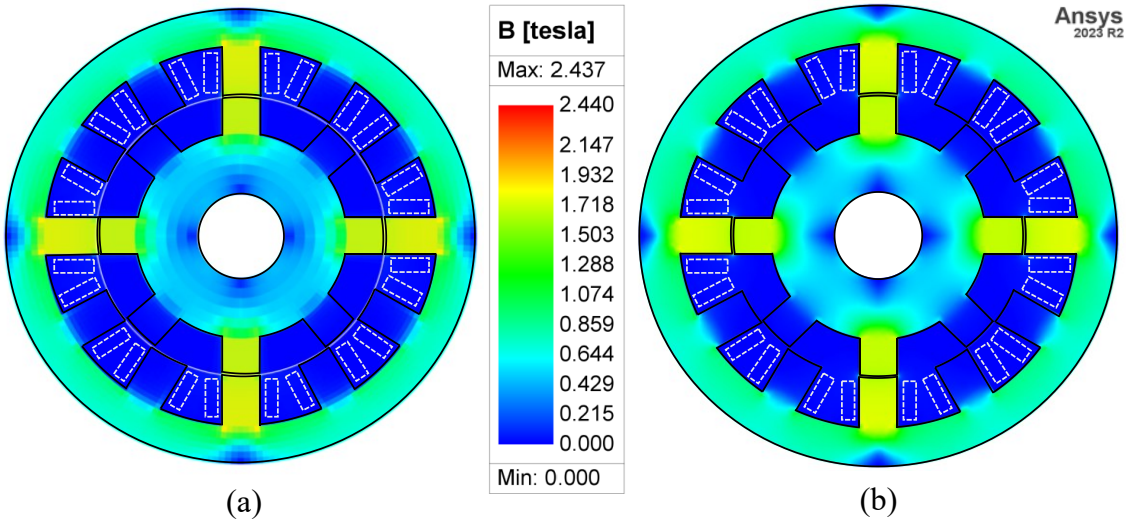


(a) (b)

Figure 4.25 Magnetic flux density distribution of the studied SRM due to the injection of peak current into phase A at the aligned position, calculated by (a) the proposed distributed circuit-based model, and (b) FEM

Table 4-1 Computational performance of the proposed distributed circuit-based model and FEM-based model

| **Model** | **time-step** | **Simulation Time** | **CPU time** |
|---|---|---|---|
| CoSim-FEM | 1$\mu$s | 12 ms | 3h, 25min, 46s |
| CBEMT | 1$\mu$s | 12 ms | 22min, 34s |

## 4.5 Models Comparison

In this section, we present a comprehensive comparison of the circuit-based models of the SRM proposed in this chapters. The models are assessed in terms of accuracy and computational efficiency. Moreover, the most suitable model among the proposed circuit-based models is determined for each type of transient study.

In this regard, the circuit-based models of the SRM are categorized into four groups. The first group consists of lumped circuit-based models, including the type-1, type-2, and type-3 models. The second group is the topological circuit-based model. The third group is the simplified distributed circuit-based model. The fourth group is the distributed circuit-based model.

The equivalent circuit of the type-1, type-2, and type-3 are respectively shown in Figure 3.6, Figure 3.14, and Figure 3.21 (c). Also, Figure 3.25 shows the circuit of the topological circuit-based model. Also, we defined simplified distributed circuit-based model with various mesh divisions as shown in Figure 4.26.

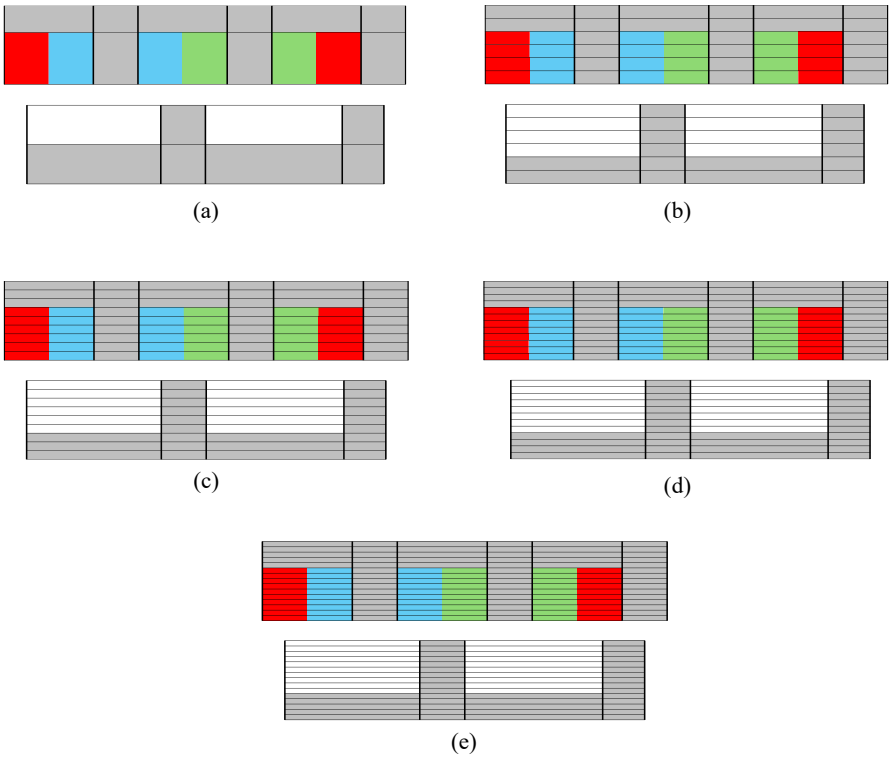


Figure 4.26 Simplified distributed circuit-based model with various mesh divisions, (a) case 1, (b) case 2, (c) case3, (d) case 4, and (e) case 5

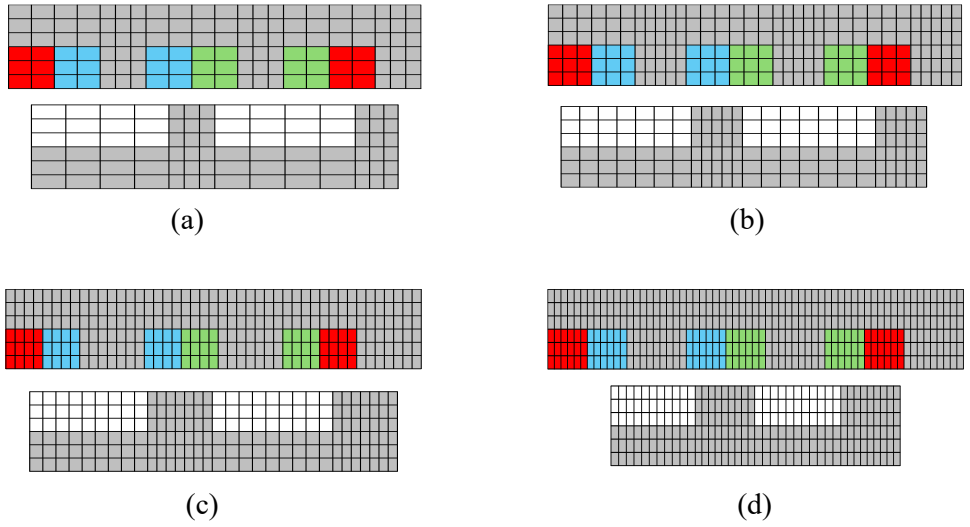


Figure 4.27 Distributed circuit-based EMT model with various mesh divisions, (a) case 1, (b) case 2, (c) case 3, and (d) case 4

For the distributed circuit-based model, four cases have been selected for the comprehensive model comparison presented in this chapter, as shown in Figure 4.27.

All mentioned models are compared in terms of accuracy and computational time. The relative error between the average torque calculated by each model and that obtained from the FEM-based model is used to assess the accuracy of each model. Figure 4.28 shows the relative error of the proposed models versus their computational time. Moreover, to have a more clarified view of the accuracy and computational time of the proposed models, Figure 4.29 presents the relative error of the proposed models versus their computational time on a logarithmic scale.

As shown in Figure 4.28 and Figure 4.29, the lumped models offer considerably faster simulation. However, only the type-3 lumped model provides acceptable accuracy (relative error below 5%). The topological circuit-based model shows comparable performance to the type-3 lumped model in terms of both accuracy and computational time. The relative error of the average torque is 4.15% for the topological model and 4.64% for the type-3 lumped model. In terms of computational time, the topological model takes 10.05 s, while the type-3 lumped model requires 8.454 s. Using a mesh-based approach in both the stator and rotor of the machine improves the model's accuracy, though it leads to higher computational time. In a similar way, increasing the number of mesh divisions

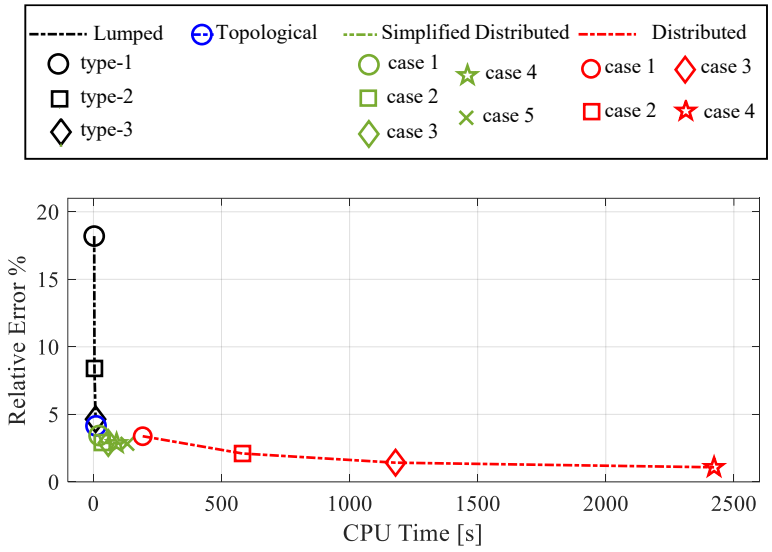


Figure 4.28 Comparison of the proposed models in terms of accuracy and computational time

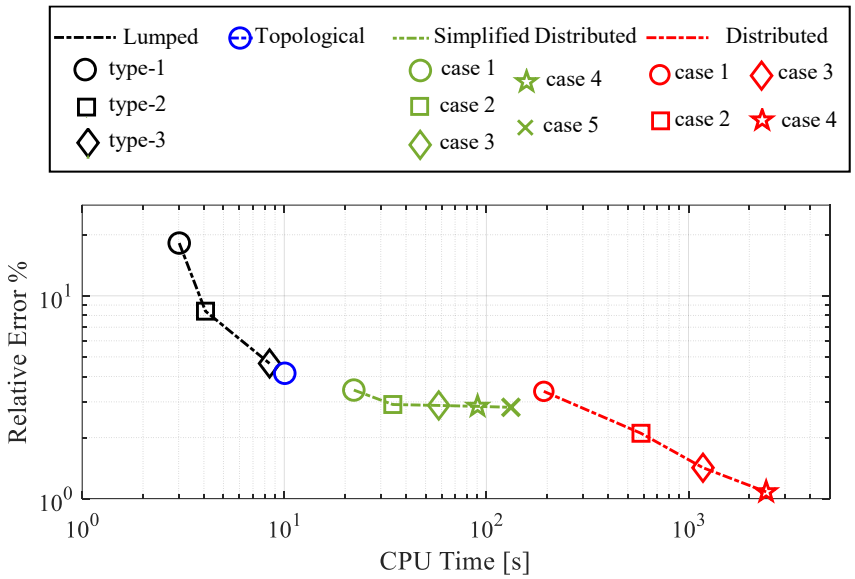


Figure 4.29 Comparison of the proposed models in terms of accuracy and computational time in the logarithmic scale

enhances the accuracy of the model but leads to longer computational time as well. It is worth noting that in the simplified distributed model, the number of mesh divisions can be changed only in the radial direction. However, the number of mesh divisions in the orthoradial direction within each tooth and slot of the machine is equal to one. Distributed circuit-based models offer the highest accuracy among all considered models. However, they are slower than the simplified distributed,

topological, and the lumped models. Additionally, the number of mesh divisions in the orthoradial direction affects the accuracy of the distributed models. Increasing the number of mesh divisions improves accuracy while leading to higher computational time.

## 4.6 Appropriate circuit-based Model Choice for Various EMT Studies

In this section, we aim to define suitable model for various EMT study scenarios. As shown in the previous section, all models except the type-1 and type-2 lumped models provide acceptable accuracy. However, each model has its limitations. Therefore, we highlight the advantages and disadvantages of each model, and based on their advantages and disadvantages, propose which model is appropriate for each EMT study scenario.

It is worth noting that all proposed magnetic circuits in this chapter can be seamlessly connected to electric circuit and mechanical circuit. This advantage makes it possible to integrate the circuit-based EMT model of the electric machine in any large power circuit through a simultaneous solution.

The distributed circuit-based model provides acceptable accuracy. The accuracy of this model improves as the number of mesh divisions in the orthoradial direction increases. It has also been shown that increasing the number of mesh divisions in the orthoradial direction enhances the model's precision in calculating the torque ripples and machine's space harmonics. These models can represent detailed local magnetic behavior of the machine, such as local saturation, and can simulate all transient phenomena happening inside the machine, such as short circuits in the machine's windings. Therefore, we recommend using the distributed circuit-based model for EMT studies involving internal faults within the machine, or for studies in which transient phenomena occur in the external power system, while their impact on the machine's detailed magnetic behavior, such as local saturation, needs to be analyzed and studied. Also, this model can be used in the detailed design procedure. It can also be extended for multi-physics studies.

The simplified distributed circuit-based model demonstrates acceptable accuracy. Increasing the number of mesh divisions in the radial direction improves its accuracy, particularly in calculating the average value of the magnetic flux density. However, since only one mesh division is used in the orthoradial direction, the model is not able to simulate all detailed local magnetic phenomena, such as local saturation and internal winding faults. Similarly, due to the use of only one mesh division in the orthoradial direction within the teeth and slots of the machine, the model cannot

consider all the machine's space harmonics and calculate the torque ripple very accurately. Despite these limitations, the simplified distributed model can provide a reasonable overall estimation of the average magnetic flux density in the teeth and yokes of the machine, as well as an overall view of the flux path in the machine. We suggest using this model for EMT studies that do not contain transient phenomena inside the machine but require acceptable torque estimation and an overall view of the internal magnetic behavior of the machine. This model can also be used for the initial design and sizing of the machine.

The topological model provides a faster solution than the simplified distributed model. However, its accuracy is less than the simplified distributed model and requires predefining the flux path within the machine. Also, it does not offer the flexibility to trade off between accuracy and computational time. We recommend using the topological model in studies where there are no transient phenomena inside the machine and the machine's model is integrated into a large external power circuit. In these case studies, selecting a machine model with both fast computational performance and acceptable accuracy is essential.

Finally, the type-3 lumped model is faster than distributed, simplified distributed, and topological circuit-based models, but it offers lower accuracy. Nevertheless, its overall accuracy is acceptable. This model does not consider the internal behavior of the machine and does not allow for a trade-off between accuracy and computational time. We recommend using this model in studies where there are no transient phenomena in the machine and the main focus is on control aspects.

## 4.7 Conclusion

This chapter focused on the verification and assessment of the proposed circuit-based EMT model of SRM.

The type-1 lumped model is the simplest, ignoring nonlinear magnetic behavior, mutual coupling, and space harmonics. Type-2 lumped model accurately includes machines' saliency by considering the variable permeances connecting all stator teeth to the rotor teeth. In type-3 lumped model the accuracy was improved by considering the MMF drops in the teeth and yokes through nonlinear permeances. Among the proposed lumped models, type-1 was the fastest but had low accuracy, whereas type-3 provided acceptable accuracy with a higher computational time.

The topological model considers more detailed aspects of the machine than the lumped models such as mutual coupling. In the proposed topological models, the MMF drop in the teeth and yokes of both the stator and rotor is modeled using a single nonlinear permeance. However, the effect of rotor and stator slots are neglected in the proposed topological model. This model was more accurate and slower than the lumped models.

The simplified distributed model was more accurate than the lumped and topological models. However, its computational time was higher than the lumped and topological models.

Among the proposed models, the distributed model was the most accurate while it was slower than the other models.

Based on the advantages and disadvantages of each model, recommendations were made for their application in different types of EMT studies.

# CHAPTER 5 SYSTEM-LEVEL EMT STUDIES

In this chapter, we integrate the proposed circuit-based EMT model of the machine into the case study power system shown in Figure 2.1 to perform various transient studies. The appropriate circuit-based model of the machine is selected according to the transient studies to be performed. These transient studies are presented in the following.

## 5.1 Detailed Study of the System's Transient Behavior under Battery Fault

In this part, the effect of a short circuit fault in a battery on the transient behavior of the case study power system (shown in Figure 2.1) and on the internal magnetic behavior of the SRM is studied. In this regard, the distributed circuit-based model of the SRM is used for this study as it enables the detailed modeling of the machine's internal magnetic behavior.

In the studied power system, the asymmetric bridge converter excites the SRM's phase windings while the hysteresis current controller maintains the SRM phase current at the reference peak value $I_{ref}$ within a defined bandwidth $bw$. The asymmetric bridge converter is connected to the batteries via a bidirectional DC-DC converter, which regulates the battery output voltage to maintain a constant DC link voltage $v_{DCLink}$.

The circuit-based representation of the studied power system is shown Figure 5.1. This EMT model benefits from a simultaneous solution among all its components, thanks to the circuit-based representation of each component.

As shown in this figure, the detailed model of the lithium-ion (Li-Ion) battery is implemented in this study. Further details about the battery model are available in [68]. The power electronics switches and diodes are modeled by their detailed circuit-based EMT model proposed in section 2.2. Also, the proposed distributed circuit-based EMT model of SRM is seamlessly integrated within this system, enabling the modeling of the machine's detailed internal behavior within a simultaneous solution with the external power circuit.

The control diagram of the bidirectional DC-DC converter is illustrated in Figure 5.1 (b). As shown in this figure, the converter regulates the battery's output voltage $v_{in_{bi}}$ by adjusting the duty cycle $D$ to maintain the DC link voltage (which is equal to the output voltage of the bidirectional DC-DC converter $v_{out_{bi}}$) at a constant value [99]. The position control of the SRM, shown in Figure

5.1 (c), determines which phase should be excited at each time step. Additionally, the hysteresis current controller of the SRM is shown in Figure 5.1 (d). The working principle of the position and hysteresis current control of SRM is presented in section 1.3.2 in Chapter 1.

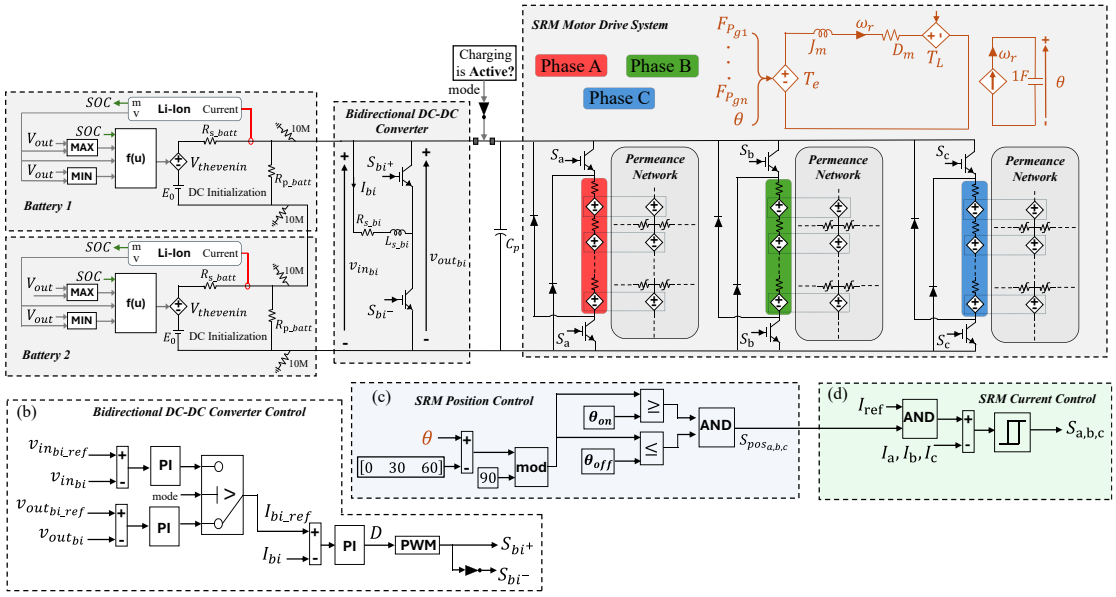


Figure 5.1 Circuit-based EMT model of the studied system, (a) batteries, bidirectional DC-DC converter and the power circuit of SRM's drive system, (b) controller of bidirectional DC-DC converter, (c) position control of SRM, (d) current control of SRM

This system is simulated for 0.9 s with a simulation time-step of 5 $\mu$s. The system is modelled from the start and reaches the steady-state at $t =$ 0.1 s. At $t = 0.15$ s, there is a short circuit to ground fault at the terminal of the second battery (Battery 2 in Figure 5.1 (a)). As shown in Figure 5.2 (a), the voltage of the first battery remains constant while Figure 5.2 (b) shows that the voltage of the second battery drops to zero after the short circuit to ground fault.

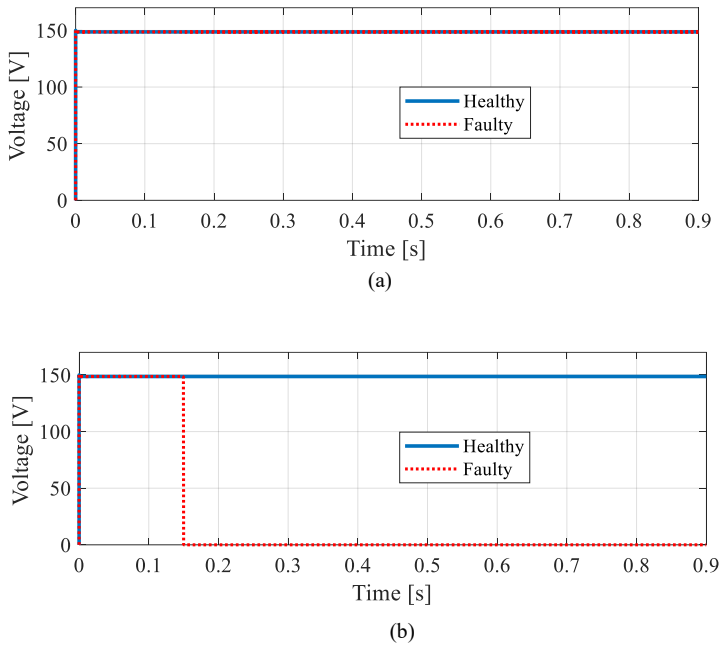


Figure 5.2 Voltage of batteries, (a) battery 1, (b) battery 2

Figure 5.3 (a) and Figure 5.3 (b) show the SOC of the first and second battery, respectively. As shown in these figures, the SOC of both batteries decreases more rapidly after the fault. However, the second battery discharges significantly faster than the first battery due to the short circuit to ground fault at its terminals. After the short-circuit fault, the output voltage of the battery system drops from 300 V to 150 V. This voltage reduction is undesirable in EV's power systems, where a stable DC link voltage is essential. As a result, the controller of the DC-DC converter adjusts its duty cycle to maintain the operation of the motor drive system. Consequently, the first battery must compensate for the contribution lost from the second battery due to the short circuit fault on the terminal of the second battery. This increased load on the first (healthy) battery, resulting in its more rapid discharge.

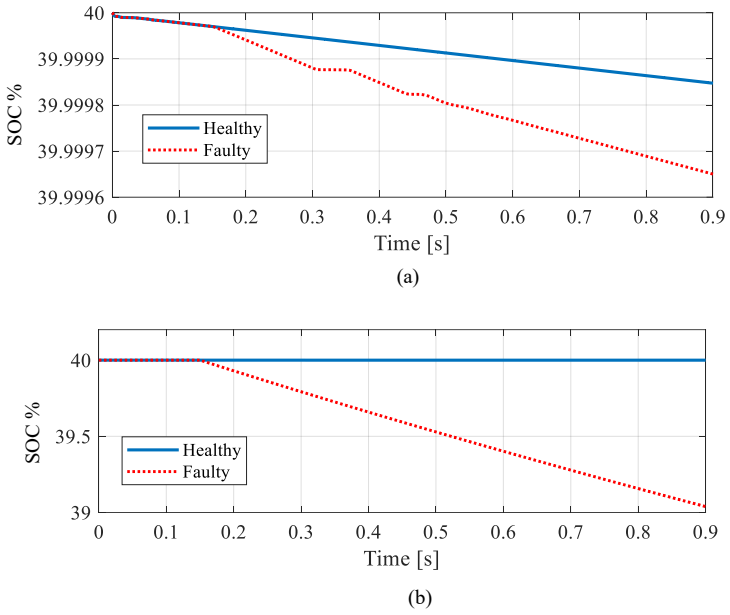


Figure 5.3 SOC of batteries, (a) battery 1, (b) battery 2

Figure 5.4 presents the duty cycle of the bidirectional DC-DC converter. As shown in this figure, the converter's controller reduces the duty cycle to compensate for the voltage drop caused by the short circuit fault at the terminal of the second battery.

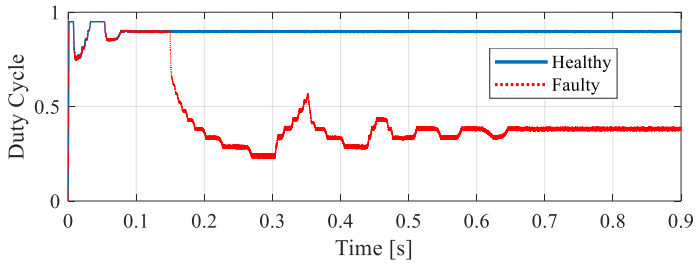


Figure 5.4 Duty cycle of the bidirectional DC-DC converter

Reducing the duty cycle to compensate for the voltage drop caused by the short circuit fault on the terminal of the second battery results in increasing the current of the DC-DC converter, as shown in Figure 5.5. This figure shows the effect of changing the duty cycle of the bidirectional DC-DC converter on its current. As can be seen, the controller system ensured the operation of the motor drive system but it results in the more rapid discharging of the healthy battery, as shown in Figure 5.3 (a).

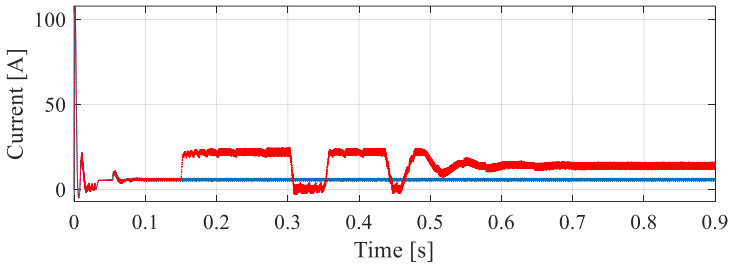


Figure 5.5 Current of the bidirectional DC-DC converter

Figure 5.6 illustrates the DC link voltage $v_{DCLink}$, which is equal to the output voltage of the bidirectional DC-DC converter $v_{out_{bi}}$. Immediately after the fault, the DC link voltage dropped suddenly to 150 V. It experienced a transient behavior while the controller of the bidirectional DC-DC converter adjusted the duty cycle to maintain the DC link voltage at 300 V.

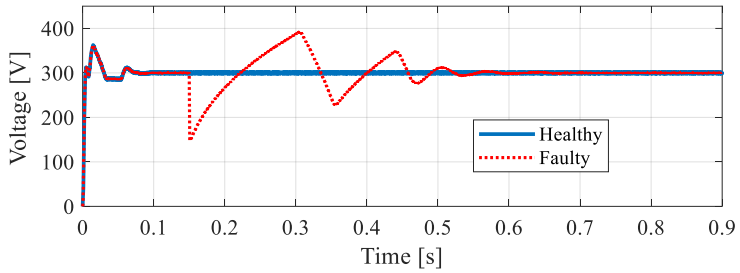


Figure 5.6 DC link voltage

Figure 5.7 presents the effect of the DC link voltage transients, caused by the short circuit in the second battery, on the SRM's speed. As shown in this figure, the sudden drop in DC link voltage from 300 V to 150 V results in a decrease in the machine's speed from 3000 rpm to 2750 rpm. The speed returns to 3000 rpm once the bidirectional DC-DC converter maintains the DC link voltage at 300 V.

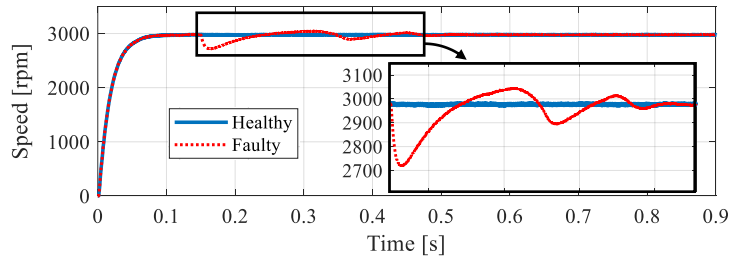


Figure 5.7 SRM's speed

The electromagnetic torque of the SRM for the whole simulation time is shown in Figure 5.8 (a), while Figure 5.8 (b) shows the electromagnetic torque before the fault. The electromagnetic torque immediately after the fault is shown in Figure 5.8 (c). As shown in this figure, there is a sudden reduction in the electromagnetic torque immediately after the fault. Figure 5.8 (d) shows the electromagnetic torque once the system has reached the steady-state after the fault. As shown in these figures, after the transient response and the adjustment of control commands of the DC-DC converter and drive system controllers, the electromagnetic torque returned to its steady-state performance, similar to its behavior before the fault.

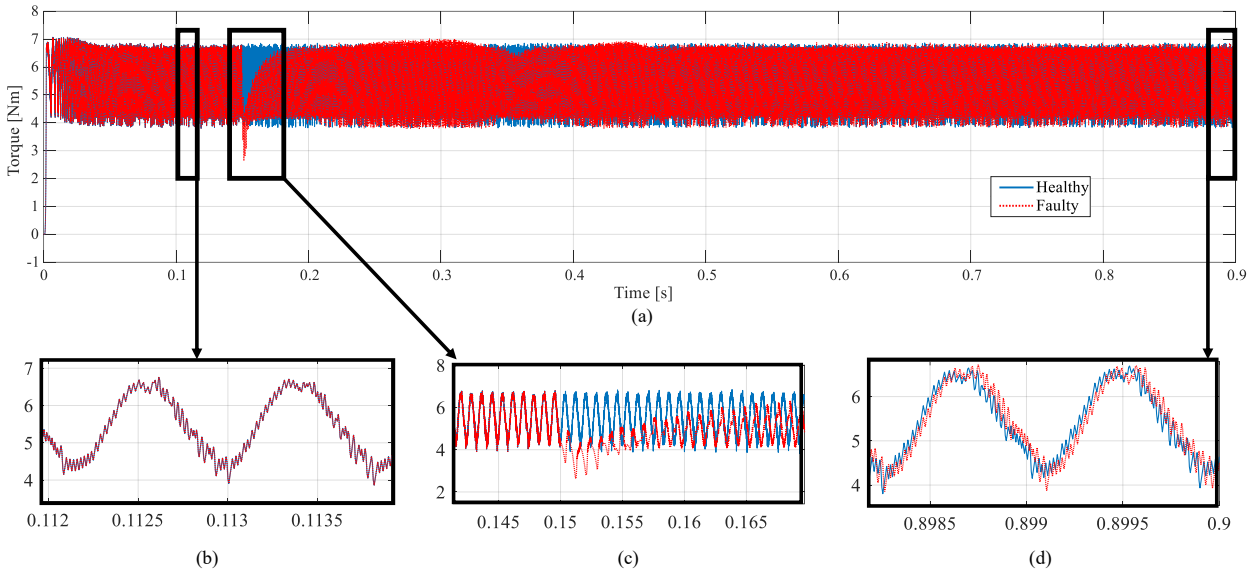


Figure 5.8 Electromagnetic torque of SRM, (a) the whole simulation time, (b) before fault, (c) when fault occurred, (c) steady state performance after fault

The current of SRM's phase A is shown in Figure 5.9. As shown in this figure, the hysteresis current controller maintained the SRM's phase current in the defined reference current $I_{ref}$, before and after the fault. However, the short circuit fault in the second battery caused a sudden decrease in the SRM's phase current immediately after the fault (see Figure 5.9 (c)). Also, Figure 5.10 and Figure 5.11 show the current of phase B and phase C, respectively. As shown in these figures, the current of phase B and C have a same behavior like phase A with 120 degree electrical phase shift.

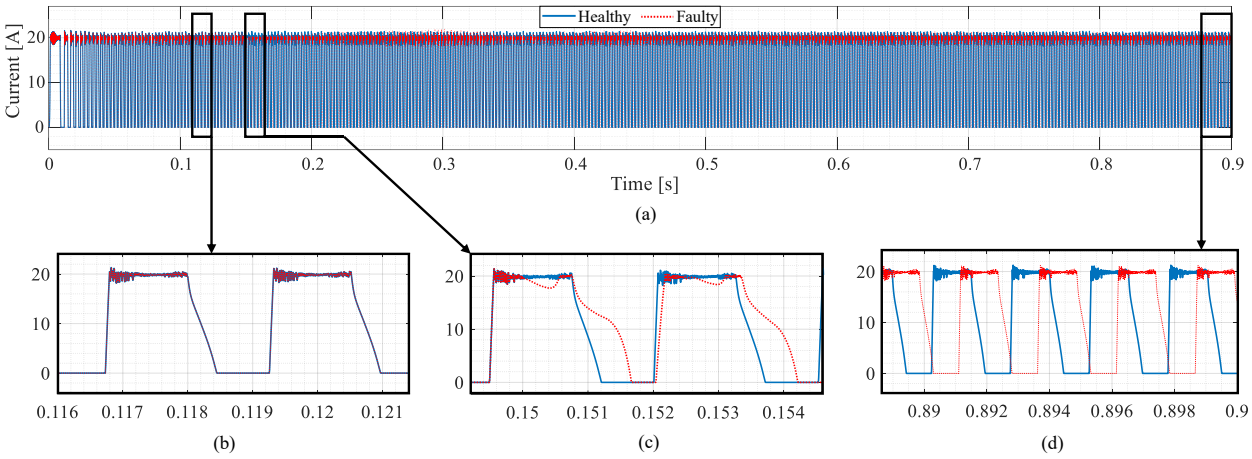


Figure 5.9 Phase A current, (a) the whole simulation time, (b) before fault, (c) when the fault occurred, (c) steady state performance after the fault

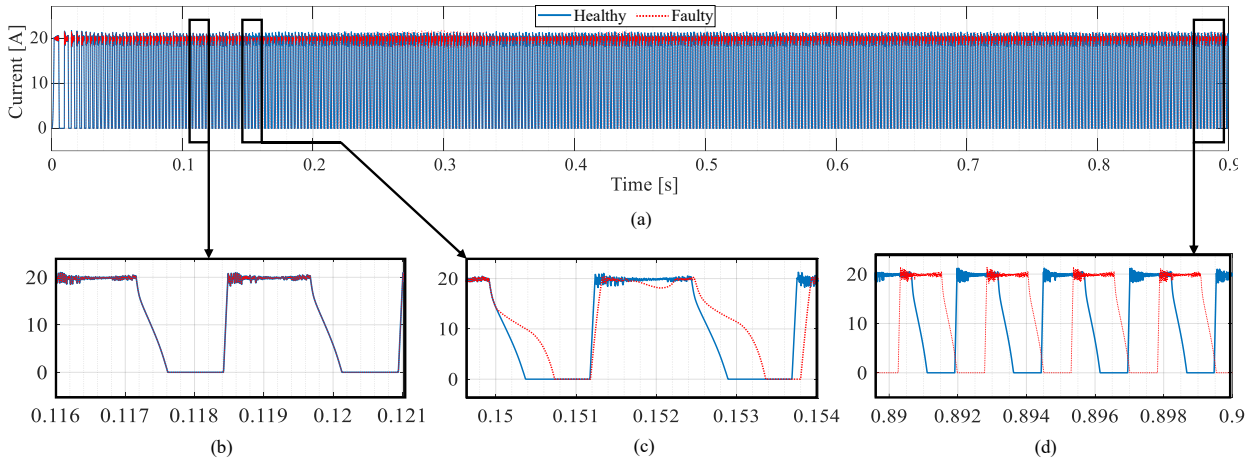


Figure 5.10 Phase B current, (a) the whole simulation time, (b) before fault, (c) when the fault occurred, (c) steady state performance after fault

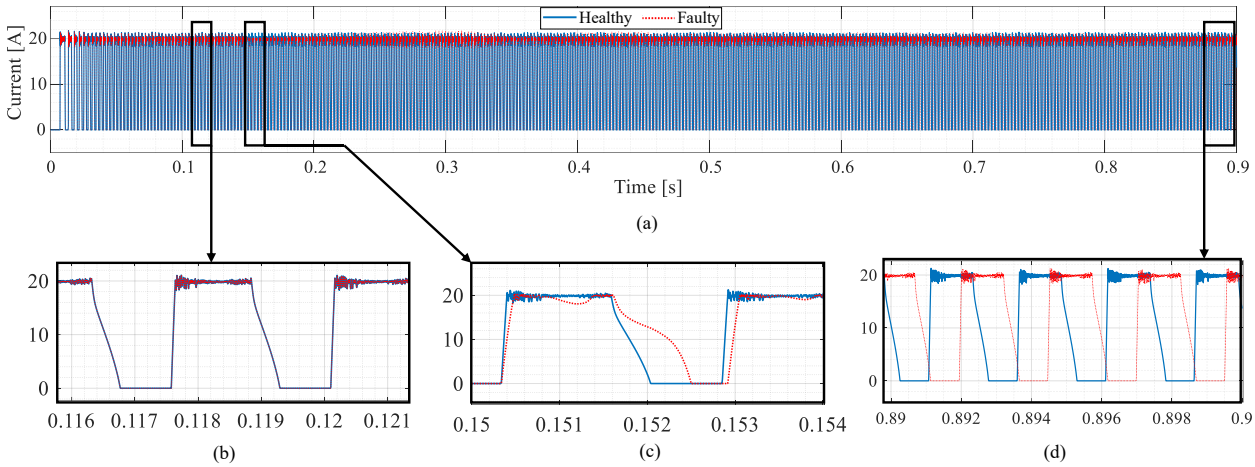


Figure 5.11 Phase C current, (a) the whole simulation time, (b) before fault, (c) when the fault occurred, (c) steady state performance after the fault

Finally, Figure 5.12 shows the effect of the short circuit fault at the terminal of the second battery on the machine's magnetic flux density. Figure 5.12 (a) and Figure 5.12 (b) respectively show the magnetic flux density distribution in the healthy and faulty mode at $t = 0.1505$ s (immediately after fault). Moreover, the magnetic flux density distribution at $t = 0.7$ s in the healthy and faulty operation are presented in Figure 5.12 (c) and Figure 5.12 (d), respectively. As shown, the fault disrupted the sequence of the SRM's phase excitation and also changed the value of its phase currents. Therefore, the magnetic flux density in the yoke and teeth of the SRM has changed.

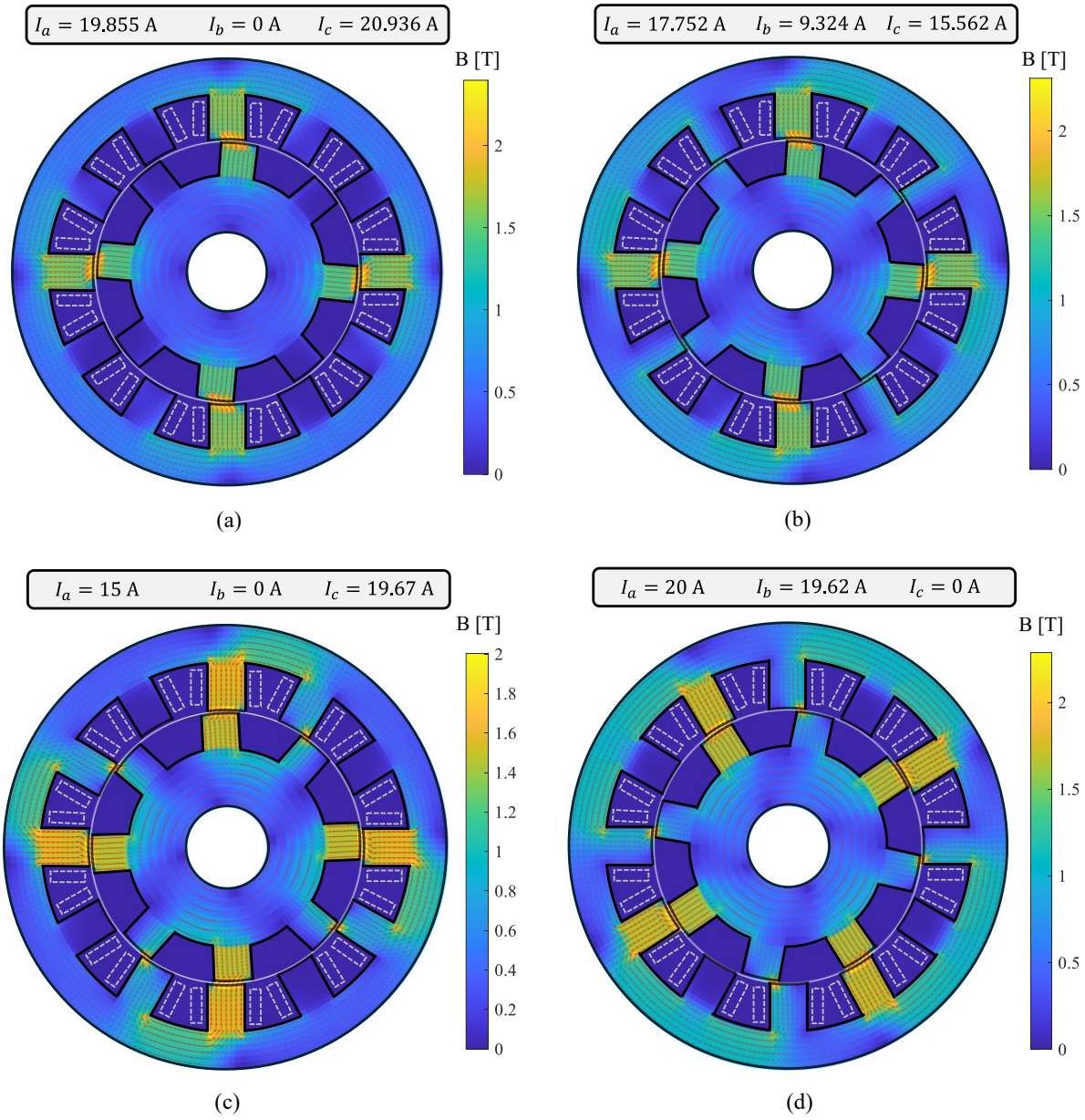


Figure 5.12 Magnetic flux density of SRM, (a) healthy operation, (b) faulty operation immediately after fault, (c) healthy operation at t = 0.7 s, (d) faulty operation at t = 0.7 s (steady-state after fault)

## 5.2 Study of the System's Transient Behavior under Battery and Drive System Faults

In this part, the effects of faults in the battery and drive systems on the transient behavior of the overall system are studied. In this study, the system is modeled from the starting, and two faults happened in the system as follows

1) a short-circuit to ground fault at the terminal of the second battery at $t = 0.1$ s
2) open circuit at the connection point between phase A of the asymmetric bridge converter and the phase A winding of the machine. $t = 0.65$ s

Since the overall behavior of the system is the focus of this study and we do not have any internal fault in the machine, we can use more simplified magnetic circuits. In this regard, we used the topological model of the SRM as it is faster than the simplified distributed and distributed models while it provides higher accuracy than the lumped models.

The circuit-based EMT model of this system, in which the proposed topological circuit-based EMT model of SRM is used, is shown in Figure 5.13. Figure 5.13 (a) shows the topological circuit-based EMT model of the SRM seamlessly integrated within the detailed circuit-based EMT model of its drive system, bidirectional DC–DC converter, and batteries. The controller of the bidirectional DC–DC converter is presented in Figure 5.13 (b). The position and current controllers of the SRM are shown in Figure 5.13 (c) and Figure 5.13 (d), respectively.

This system is simulated for 0.9 s with a simulation time-step of 5 $\mu$s. The SOC of the first battery is shown in Figure 5.14. The short-circuit fault at the terminal of the second battery causes a more rapid discharge of the battery. After the open circuit in phase A of the drive system at $t = 0.65$ s, battery 1 discharges more slowly due to load reduction caused by the open circuit.

The SOC of the second battery is shown in Figure 5.15 where there is a sudden reduction in the SOC of this battery due to the short circuit on its terminal. The open circuit in phase A of the drive system did not affect the SOC of this faulty battery since this battery is discharging to the ground due to the short circuit fault on its terminals.

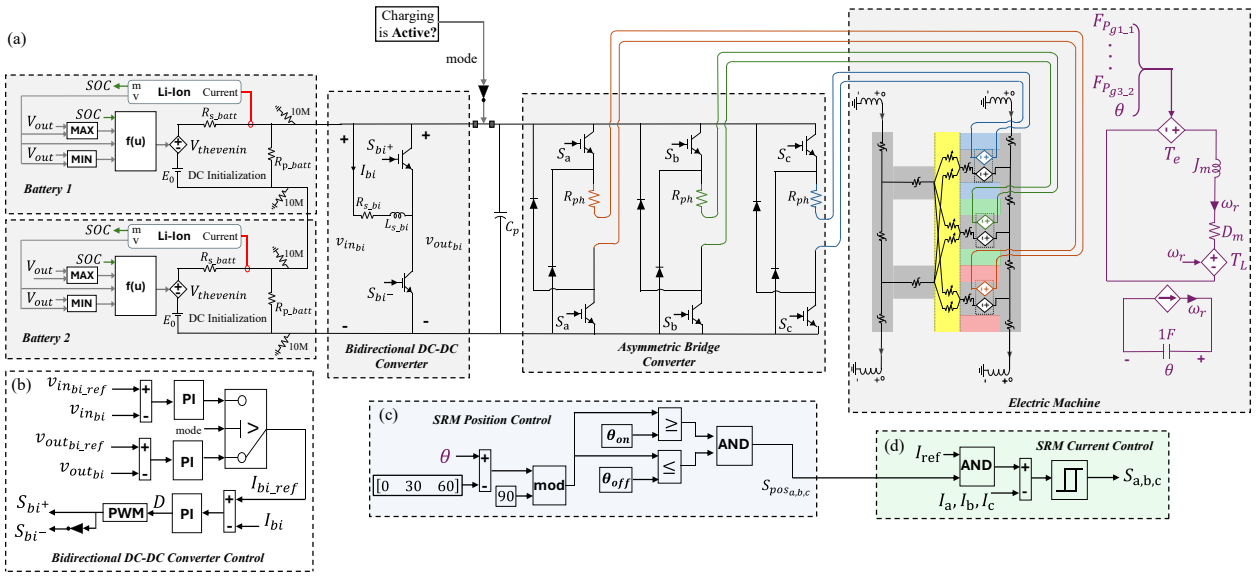


Figure 5.13 Circuit-based EMT model of the studied system (a) detailed EMT model of batteries, bidirectional DC-DC converter, asymmetric bridge converter, and topological circuit-based EMT model of the machine, (b) controller of bidirectional DC-DC converter, (c) position control of SRM, and (d) current control of SRM

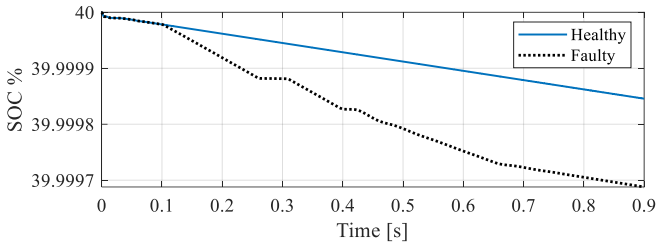


Figure 5.14 SOC of battery 1

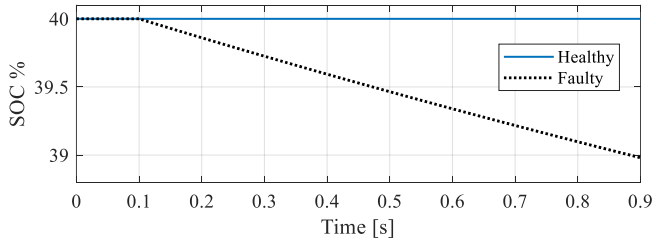


Figure 5.15 SOC of battery 2

The duty cycle of the bidirectional DC-DC converter is illustrated in Figure 5.16. As shown in this figure, the converter's controller determines the duty cycle to compensate for the voltage changes caused by the mentioned faults.

The current of the bidirectional DC-DC converter is illustrated in Figure 5.17. As shown in this figure, the short circuit at the terminal of the second battery increased the current passing through the bidirectional DC-DC converter while the load reduction caused by the open circuit in phase A of the drive system resulted in a lower current of the bidirectional DC-DC converter.

As shown in Figure 5.18, after happening the short-circuit fault at the terminal of the second battery, the DC link voltage dropped suddenly from 300 V to 150 V. It experienced transient behavior while the controller of the bidirectional DC-DC converter adjusted the duty cycle to maintain the DC link voltage at 300 V. Also, this figure shows that the DC link voltage oscillated after the open circuit fault in phase A of the SRM, while the controller of the bidirectional DC-DC converter regulated it to 300 V.

The speed of the SRM during the simulation time is shown in Figure 5.19. As shown in this figure, the sudden drop in DC link voltage from 300 V to 150 V results in a decrease in the machine's speed from 3000 rpm to 2750 rpm. The speed returns to 3000 rpm once the bidirectional DC-DC converter maintains the DC link voltage at 300 V. Additionally, the disruption of SRM's phase A due to the open circuit fault reduced the SRM's speed to 2000 rpm with a higher oscillation than the healthy mode.

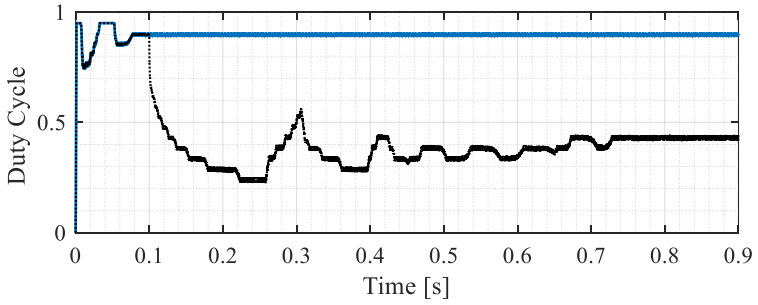


Figure 5.16 The duty cycle of the bidirectional DC-DC converter

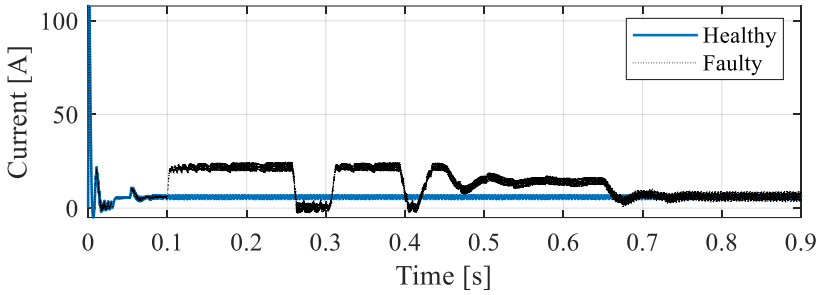


Figure 5.17 Current of bidirectional DC-DC converter

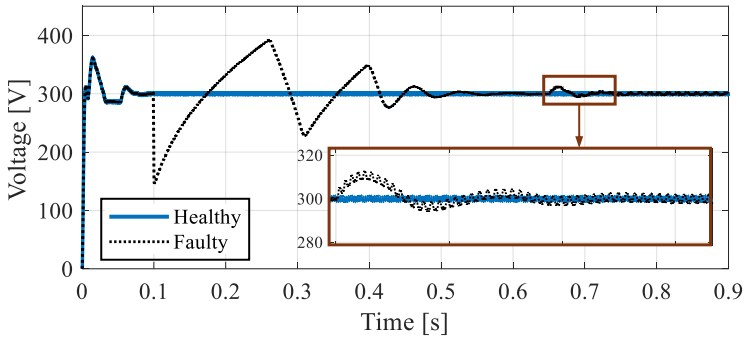


Figure 5.18 DC link voltage

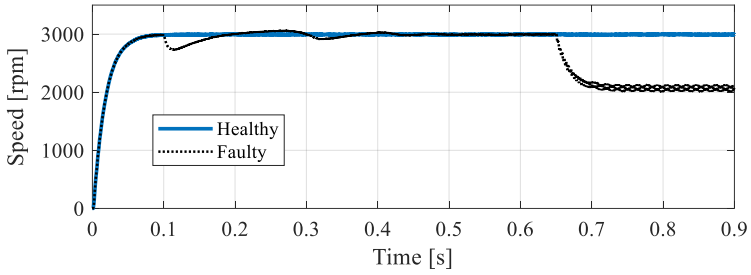


Figure 5.19 Machine's speed

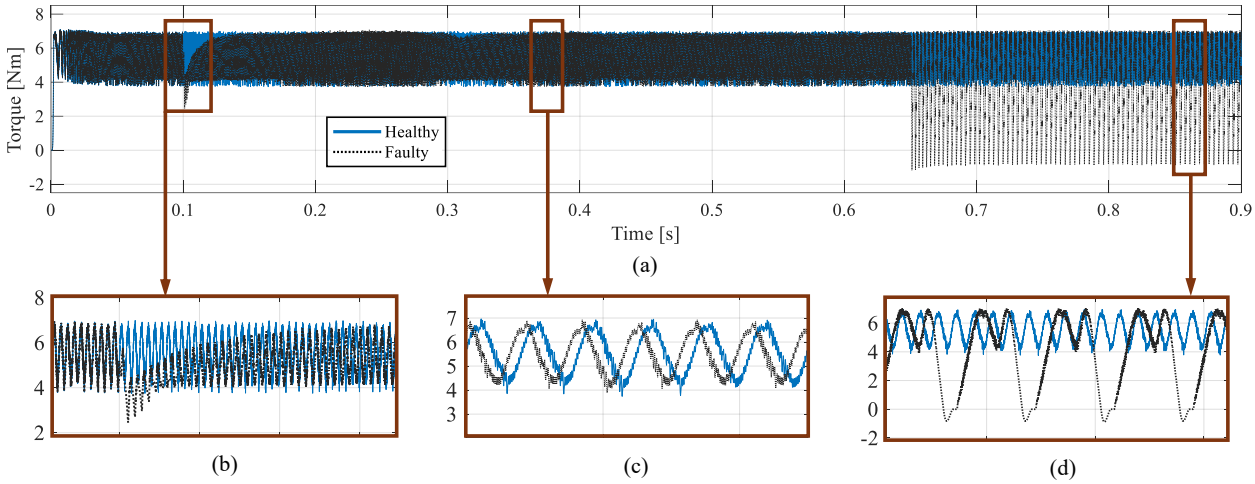


Figure 5.20 Electromagnetic torque, (a) the whole simulation time, (b) when the battery fault happened, (c) steady-state after the battery fault, (c) after the open circuit fault in SRM's phase A

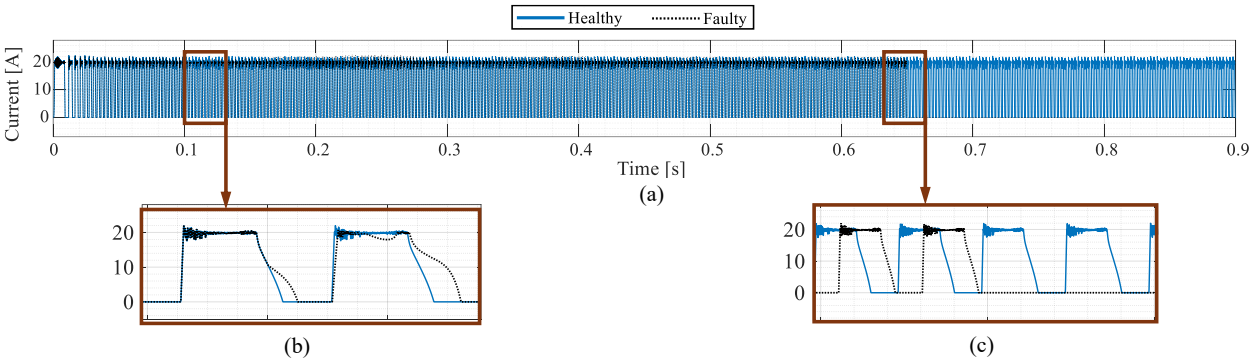


Figure 5.21 Phase A current, (a) the whole simulation time, (b) when the battery fault happened, (c) steady state performance after the battery fault and the occurrence of an open circuit in SRM's phase A

Figure 5.20 illustrates the electromagnetic torque of the SRM. The electromagnetic torque during the whole simulation is shown in Figure 5.20 (a). The electromagnetic torque immediately after the short circuit fault at the second battery terminal is shown in Figure 5.20 (b) where there is a sudden reduction in the electromagnetic torque. Figure 5.20 (c) shows the electromagnetic torque once the system has reached the steady-state after the short circuit fault at the second battery terminal. Also, the open circuit fault in the SRM's phase A at $t = 0.65$ s reduced the electromagnetic torque and increased its oscillation due to the interruption of the phase A, as illustrated in Figure 5.20 (d).

The SRM's phase A current is shown in Figure 5.21. As illustrated in the figure, the hysteresis current controller kept the SRM's phase current within the defined reference current $I_{ref}$ before faults. The SRM's phase current experienced a sudden decrease after the short circuit at the terminal of the second battery, as shown in Figure 5.21 (b). The SRM's current controller maintained the phase current in the defined reference current, while the phase A current dropped to zero after the open circuit fault in phase A, as presented in Figure 5.21 (c).

## 5.3 Studying the Detailed Transient Behavior of the Machine and Drive System Under Machine's Startup and Internal Fault

This part aims to analyze the transient behavior of the SRM drive system under internal machine faults. To achieve this, the distributed circuit-based EMT model of the SRM is employed, as it is the most accurate and most detailed model.

In this study only the drive system of the SRM is considered. In this regard, the SRM drive system is connected to a DC voltage source representing the DC-link voltage. Thus, the circuit-based representation of the SRM drive system consists of the SRM, asymmetric bridge converter and it related controller is shown in Figure 5.22. As shown in this figure, the circuit-based models of the drive system components are seamlessly connected to each other, resulting in a simultaneous solution among them.

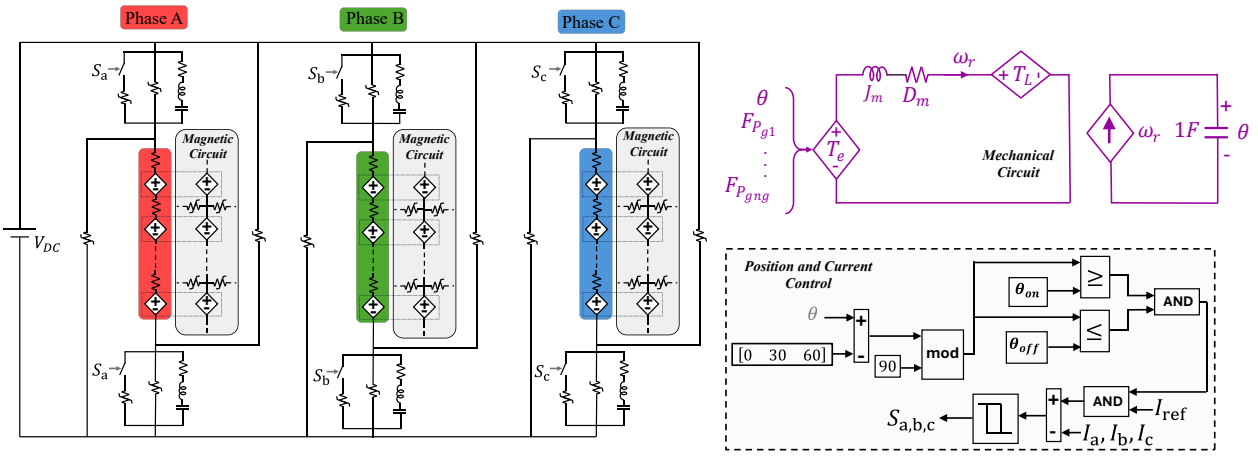


Figure 5.22 The circuit-based EMT model of the SRM drive system consists of the distributed circuit-based model of the machine

### 5.3.1 Machine's startup

In this study, the transient behavior of the SRM drive system from startup to steady-state operation is simulated and the results are compared by those obtained from CoSim-FEM.

The electromagnetic torque of the SRM, calculated by the proposed distributed circuit-based EMT model and CoSim-FEM is shown in Figure 5.23. As shown in this figure, the steady-state values of the torque calculated by the proposed circuit-based EMT model and CoSim-FEM are 5.5583 Nm and 5.7405 Nm, respectively (3.17% difference).

Figure 5.24 presents the speed of the studied SRM. As shown, the final speeds calculated by the circuit-based EMT model and CoSim-FEM are 2993.52 rpm and 3091.63 rpm, respectively (3.17% difference).

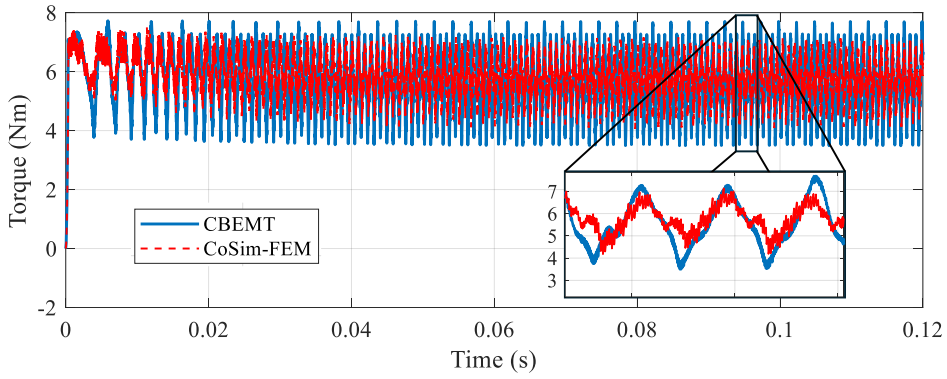


Figure 5.23 Dynamic electromagnetic torque of the studied SRM

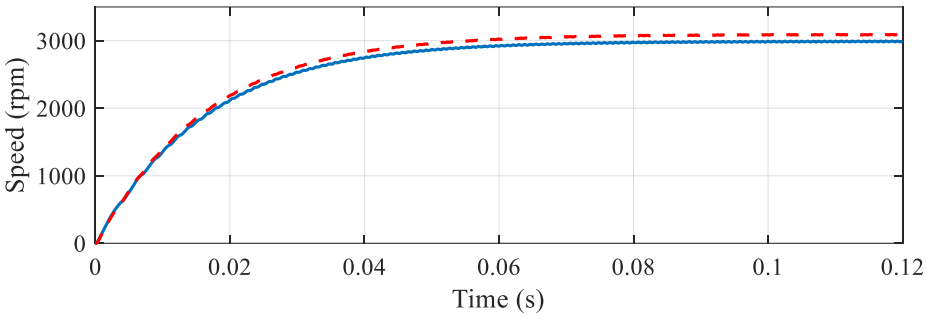


Figure 5.24 Speed of the studied SRM

Figure 5.25 (a), Figure 5.25 (b), and Figure 5.25 (c) respectively show the current waveform of phase A, phase B, and phase C. As shown, the current controller kept the phase current at the

reference level of 20 A. The frequencies of the phase current calculated by CBEMT and CoSim-FEM are 399.136 Hz and 412.2173 Hz, respectively. Therefore, the difference is 3.17%, matching the discrepancy observed in the steady-state speed value. This is due to the relation between the SRM operating frequency and its rotational speed

$$f_s = \frac{N_r \omega_r}{2\pi} \tag{5.1}$$

where $f_s$ is the frequency in Hz and $N_r$ is the SRM rotor pole number.

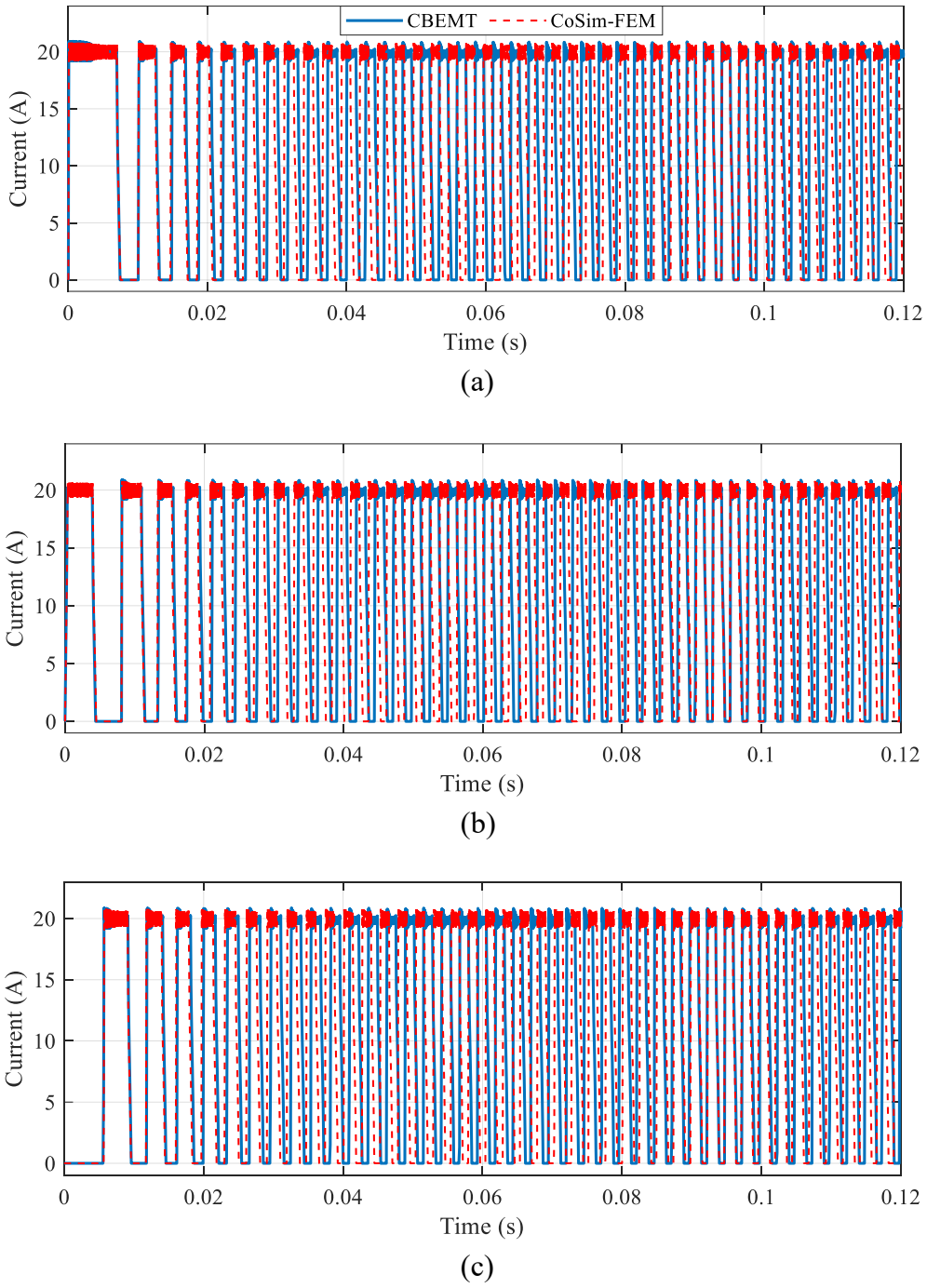


Figure 5.25 Dynamic current of the studied SRM motor drive system, (a)phase A, (b) phase B, and (c) phase C

Finally, Table 5-1 compares the computational time of the proposed distributed circuit-based model and the FEM-based model. As presented in this table, the FEM-based model is considerably slower than the circuit-based model. By employing a non-meshed approach in the airgap, the circuit-based

avoids the significant computational cost of remeshing at each time-step, which is a requirement in the CoSim-FEM model. Furthermore, CBEMT removes the complexity and computational burden introduced by the multi-software integration in CoSim-FEM, offering a more streamlined and efficient solution for system-level EMT simulations.

Table 5-1 Computational performance of the proposed distributed circuit-based model and FEM-based model during transient simulation

| **Model** | **time-step** | **Simulation Time** | **CPU time** |
|---|---|---|---|
| CoSim-FEM | $1\mu$s | 12 ms | 7d, 5h, 2min |
| CBEMT | $1\mu$s | 12 ms | 3h, 27min, 4s |

### 5.3.2 Machine's Internal Fault

To assess the transient performance of the SRM drive system under fault scenarios, the proposed distributed circuit-based EMT model is employed to simulate the transient behavior of the studied SRM drive system from starting to reaching steady-state, fault occurrence, and the steady-state performance after the fault. In these scenarios, the machine operates under healthy conditions from the start to reach a steady state. After reaching the steady state, at $t = 0.09$ s, two faults occur as follows

1) Short circuit of a coil in phase A (Fault 1)
2) Open circuit of phase A (Fault 2)

To simulate Fault 1, a switch in parallel with the fourth coil of phase A (see $SW_1$ in Figure 5.26) is closed at the moment Fault 1 occurs ($t = 0.09$ s), as shown in Figure 5.26. Also, a switch in series with phase A ($SW_2$ in Figure 5.26) is opened at $t = 0.09$ s to simulate the open-circuit fault in phase A.

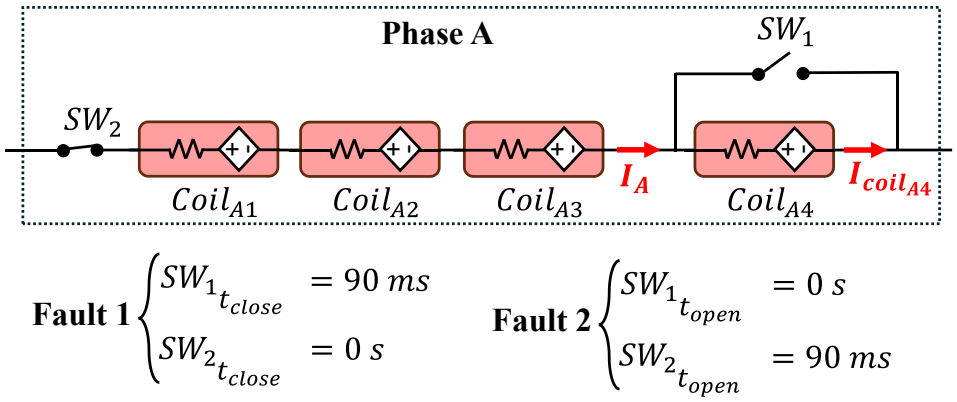


Figure 5.26 Switches simulating fault 1 and fault 2 in phase A

Figure 5.27 illustrates the phase A current of the SRM drive system during normal operation and under the mentioned fault conditions. As shown in this figure, the current frequency is reduced due to the short-circuit of the fourth coil of phase A. However, the hysteresis current controller successfully maintained the phase current at its nominal value of 20 A. After the occurrence of the open-circuit fault (Fault 2), the current of phase A dropped to zero, as depicted in Figure 5.27.

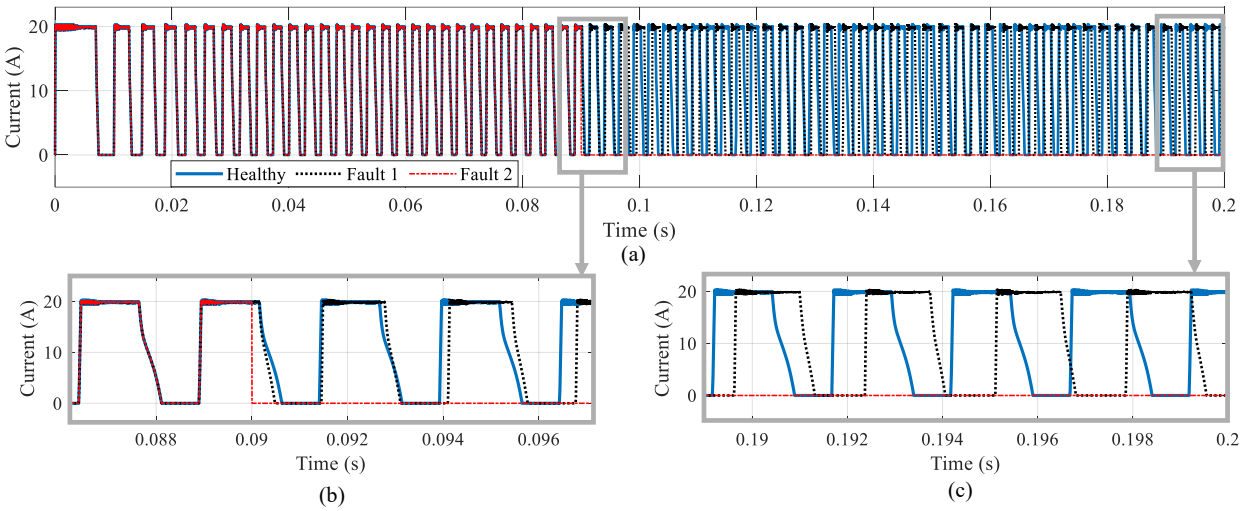


Figure 5.27 Phase A current, (a) whole simulation time, (b) when faults occurred, (c) when reached the steady state after the fault

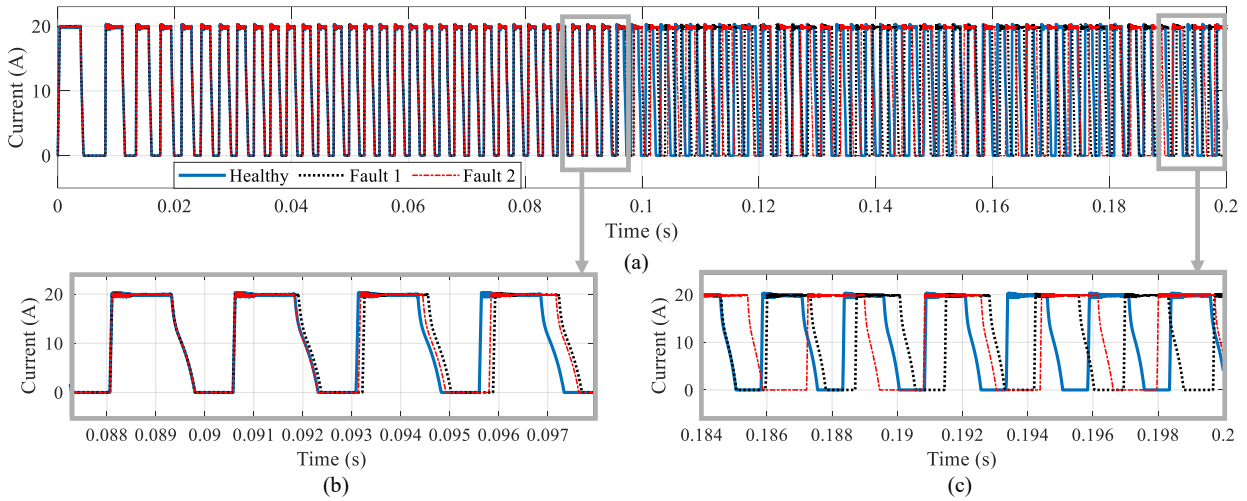


Figure 5.28 Phase B current, (a) whole simulation time, (b) when faults occurred, (c) when reached the steady state after the fault

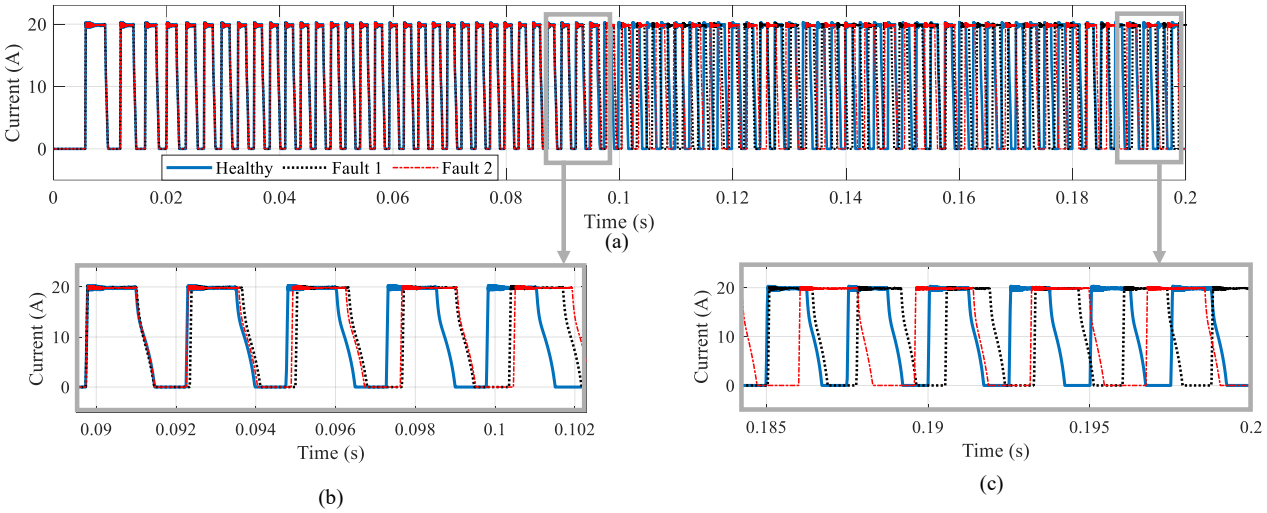


Figure 5.29 Phase C current, (a) whole simulation time, (b) when faults occurred, (c) when reached the steady state after the fault

Figure 5.28 presents the phase B current under both healthy and faulty conditions. As shown in this figure, the current frequency decreases as a result of the Fault 1(short circuit) and Fault 2 (open circuit).

It is also noteworthy that the phase C current exhibits a similar waveform to that of phase B, with a 120° electrical phase shift, as presented in Figure 5.29.

The effect of the mentioned faults on the magnetic flux density distribution immediately after their occurrence is illustrated in Figure 5.30. In this figure, healthy coils are shown in grey, while faulty coils are in red. Figure 5.30 (a) displays the magnetic flux density distribution under healthy operating conditions. Figure 5.30 (b) and Figure 5.30 (c) show the distribution under short-circuit (Fault 1) and open-circuit (Fault 2) conditions, respectively. As seen in Figure 5.30 (b), the short-circuit current in the faulty coil of phase A causes the magnetic flux density in the corresponding stator tooth to exceed 2 T. Also, during the open-circuit fault condition, the magnetic conduction due to the phase A is null in the open circuit fault condition, as illustrated in Figure 5.30 (c).

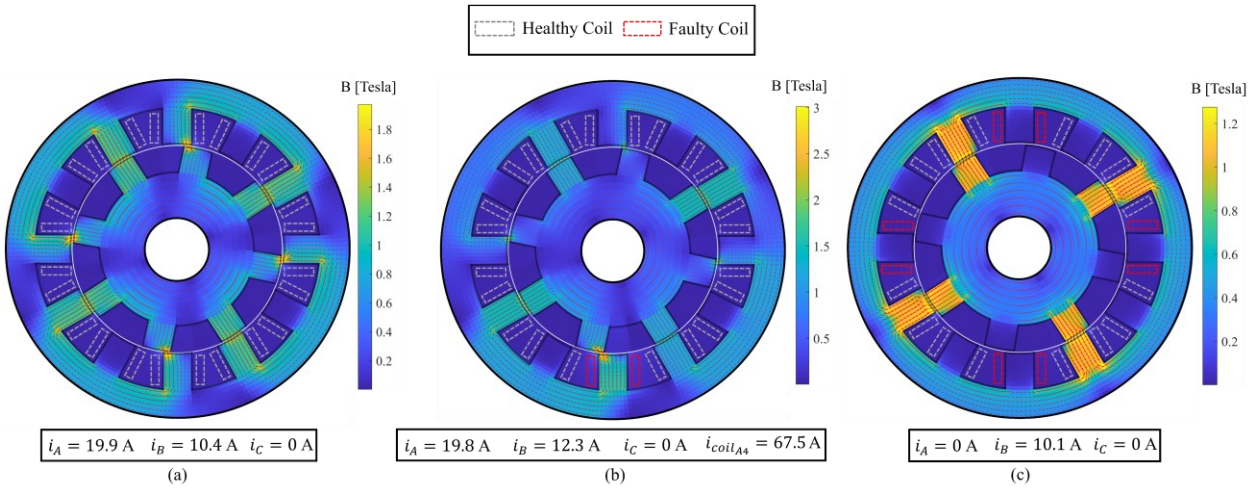


Figure 5.30 Magnetic flux density at, (a) healthy condition, (b) short circuit fault (Fault 1), (c) open circuit fault (Fault 2)

The current in the coil of phase A that experienced the short circuit is shown in Figure 5.31. As illustrated in this figure, the current of the faulty coil experienced a sudden increase immediately after the fault occurred. Once the system reaches steady state, the current in the coil begins to alternate.

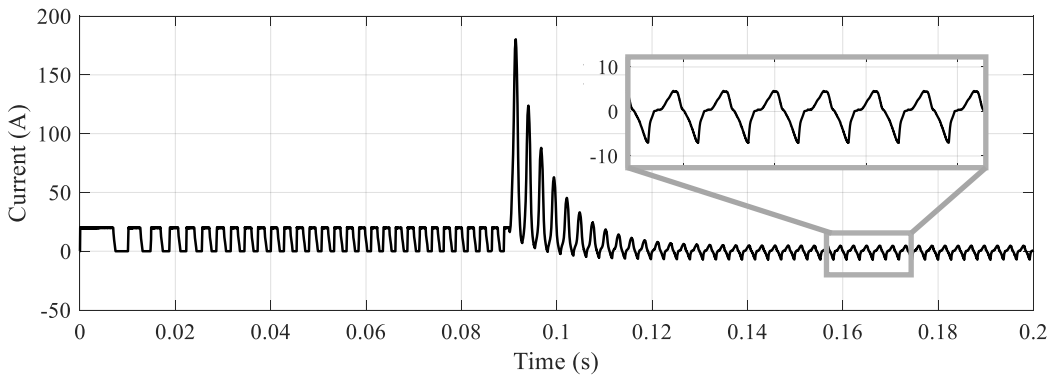

Figure 5.31 Current of the faulty coil of phase A

Figure 5.32 presents the electromagnetic torque of the SRM under both healthy and faulty conditions. As shown, the short circuit in one of the phase A coils causes a sudden change in the electromagnetic torque. Under both fault scenarios, the electromagnetic torque reached a lower average value with higher oscillation.

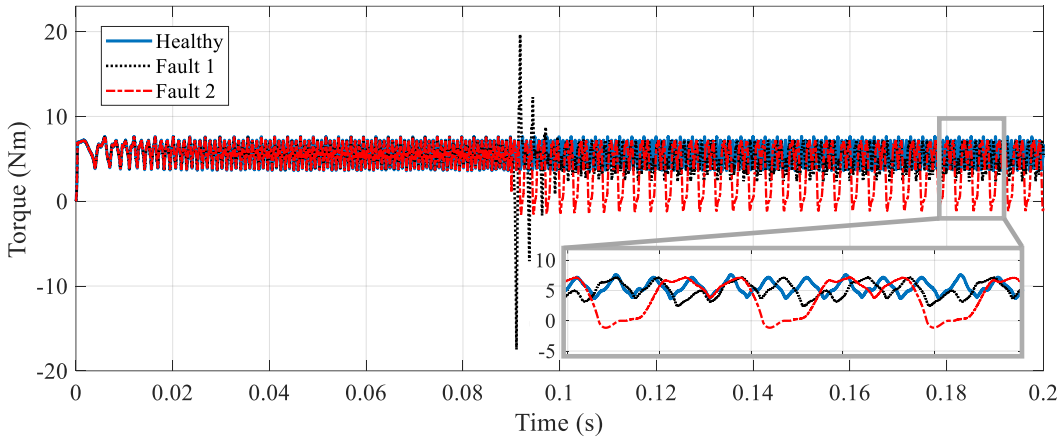


Figure 5.32 Electromagnetic torque of the studied SRM in healthy and faulty conditions

Additionally, Figure 5.33 compares the speed of the studied SRM under normal operation and the mentioned faults. As illustrated, both faults lead to a reduction in the final speed and an increase in speed oscillations. The impact of the open-circuit fault is more severe than that of the short-circuit fault due to the disruption of the entire phase A.

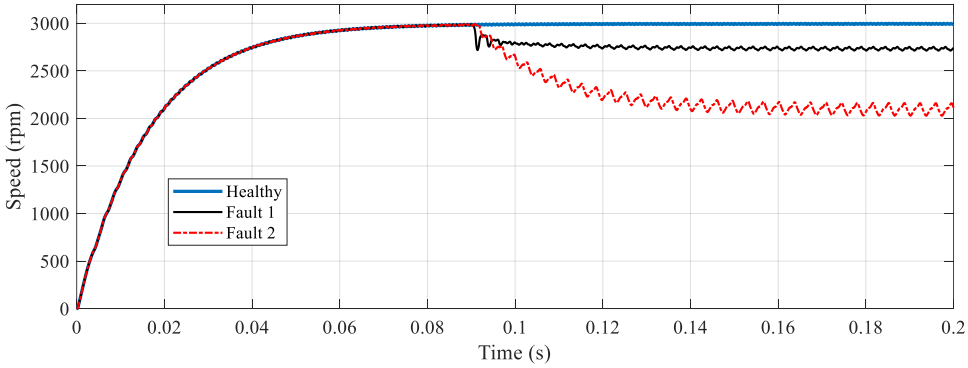


Figure 5.33 Speed of the studied SRM in healthy and faulty conditions

## 5.4 Transient Study of the Motor Drive System Under the Sudden Speed and Load Change

In this part, we aim to analyze the transient behavior of the SRM drive system due to the sudden changes in the machine's speed and load torque. To this aim, we used the simplified distributed magnetic circuit for the machine's EMT model.

Figure 5.34 shows the simplified distributed circuit-based EMT model of this case study. As shown in Figure 5.34 (a), the coupled magnetic and electric circuits of the machine are built for one quarter of it by using symmetry. An ideal transformer is used to implement the antiperiodic boundary condition. The equivalent mechanical circuit is shown in Figure 5.34 (b).

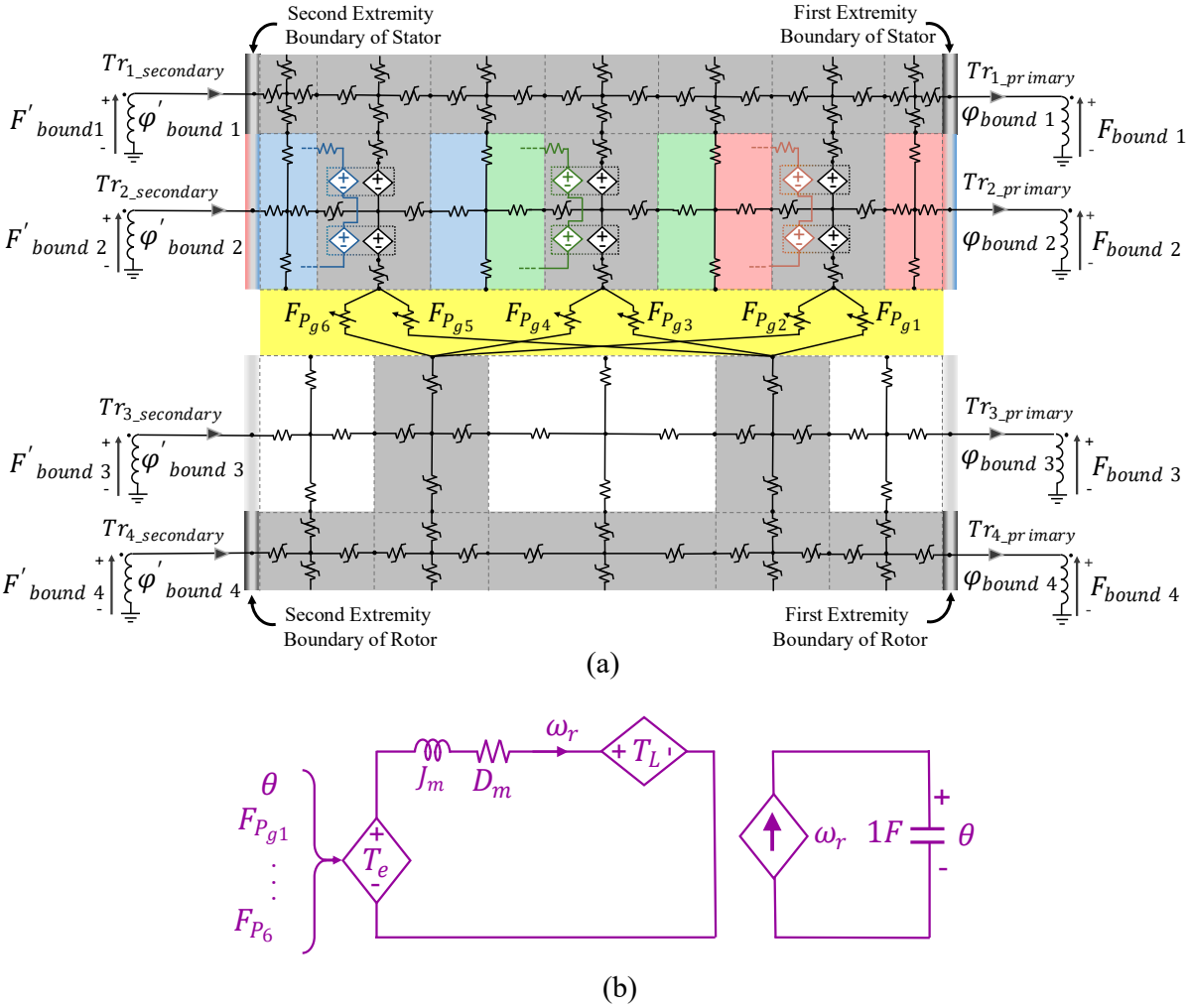


Figure 5.34 simplified distributed circuit-based EMT model of the studied SRM, (a) coupled magnetic and electric circuit, (b) mechanical circuit

Figure 5.35 shows the schematic diagram of the studied SRM drive system. As shown in this figure, the machine is connected to the asymmetric bridge converter. In the control system, the reference current $I_{ref}$ at each time step is determined by the speed controller, based on the machine's speed and the speed command, as shown in Figure 5.35.

The EMT model of this case study shown in Figure 5.35 is implemented by seamlessly integrating the simplified distributed circuit-based EMT model of the machine (named S-CBEMT in Figure 5.35) into the circuit-based EMT model of the other components of the drive system through a simultaneous solution.

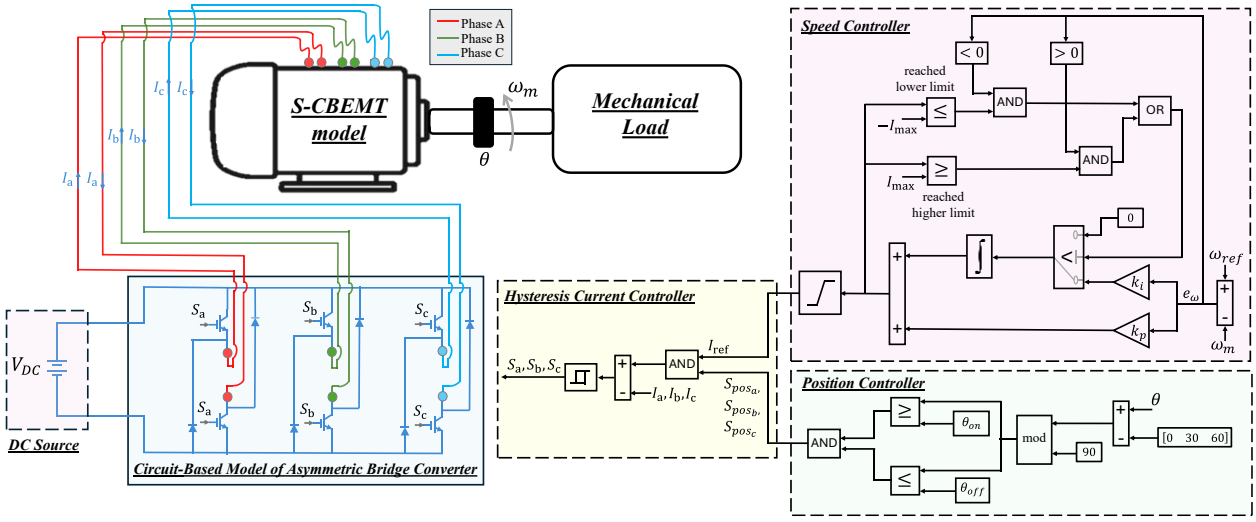


Figure 5.35 Circuit-based EMT model of SRM drive system with the proposed simplified distributed circuit-based EMT model of the machine

The transient output characteristics of the studied SRM drive system, while there are sudden changes in load and speed is shown in Figure 5.36. As shown in Figure 5.36 (a), the machine starts to work under no-load conditions ($T_L = 0$ Nm) with a speed command set to 200 rpm (see Figure 5.36 (b)). At $t = 0.035$ s, a mechanical load $T_L$ of 4.6 Nm is applied, and the speed command is increased to 1000 rpm. The machine experienced a transient and reached the steady-state before $t = 0.1$ s. At $t = 0.135$ s, the speed command is suddenly raised from 1000 rpm to 3000 rpm while the load torque remaining unchanged at 4.6 Nm. The machine accelerates until it reaches the steady-state at about $t = 0.2$ s. Then, there is a sudden reduction of speed command from 3000 rpm to 2250 rpm, at $t = 0.245$ s. Finally, at $t = 0.345$ seconds, the load torque suddenly drops to 3.4 Nm, while the speed command remains constant at 2250 rpm. As a result of the sudden drop in

load torque, the motor accelerates until the speed controller adjusts the peak phase current to bring the motor speed back to 2250 rpm. The values of $I_{ref}$ and the current of phase A are presented in Figure 5.36 (c). As shown in this figure, the value of $I_{ref}$ is determining based on the machine's speed and the speed command, and the current controller is maintaining the phase current in the defined $I_{ref}$. It is worth mentioning that the currents of phases B and C are similar to the current of phase A with 120 and 240 degrees phase shifts, respectively.

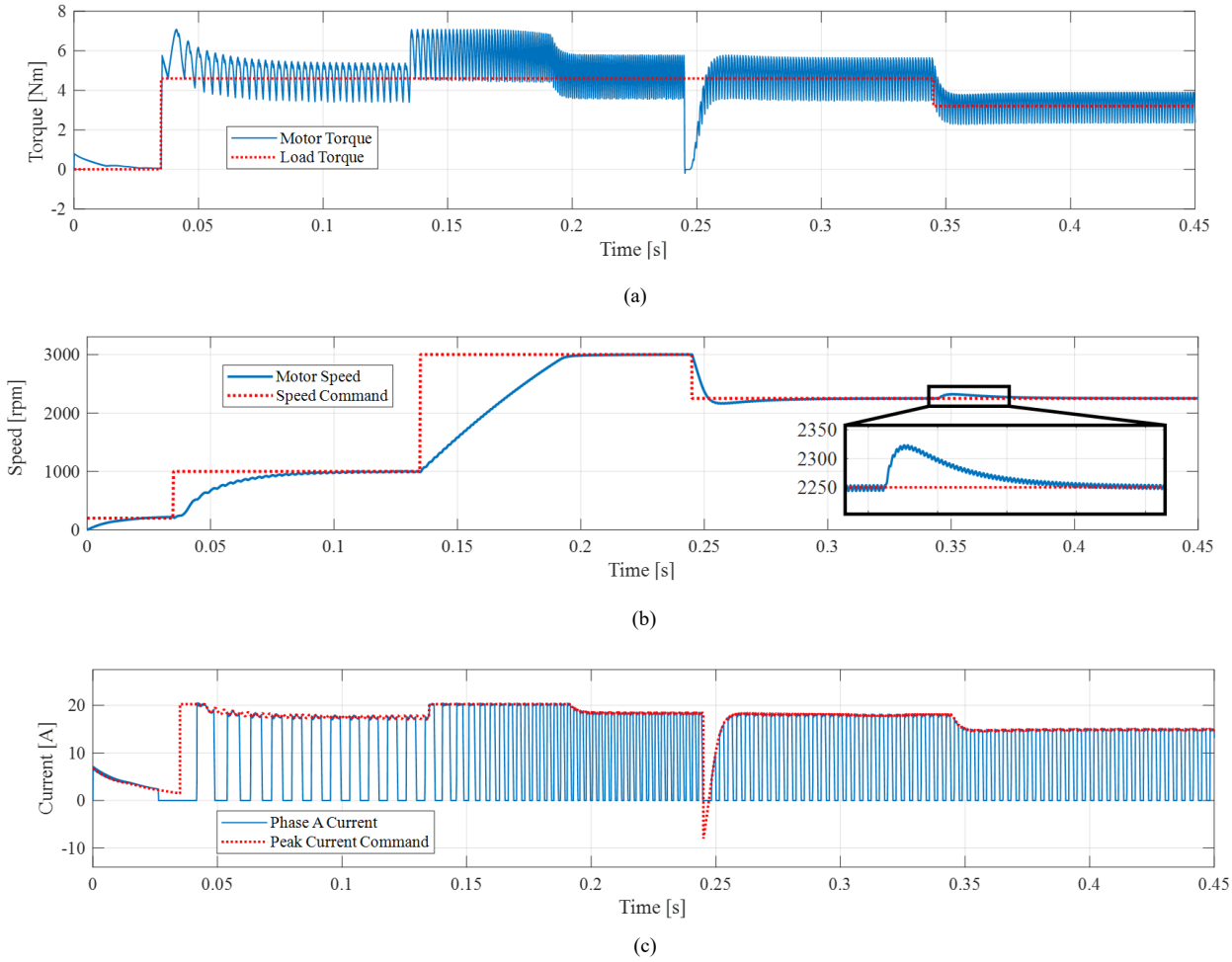


Figure 5.36 Transient output characteristics of the SRM drive system due to the sudden changes in the load torques and speed commands, (a) torque, (b) motor speed and speed commands, and (c) current of phase A and the command of phase peak

## 5.5 Transient Study of the Motor Drive System Under Speed Command Change

In this study, the transient behavior of the motor drive system during startup and due to the sudden changes in the speed command is studied. To achieve a fast solution, the type-3 lumped model of the SRM is used in this study.

Figure 5.37 illustrates the circuit-based EMT model of the SRM drive system, where there is a simultaneous solution between the machine's model and the power converter with its related controller. As depicted in Figure 5.37 (a), the magnetic behavior of the SRM is modeled by the type-3 lumped model.

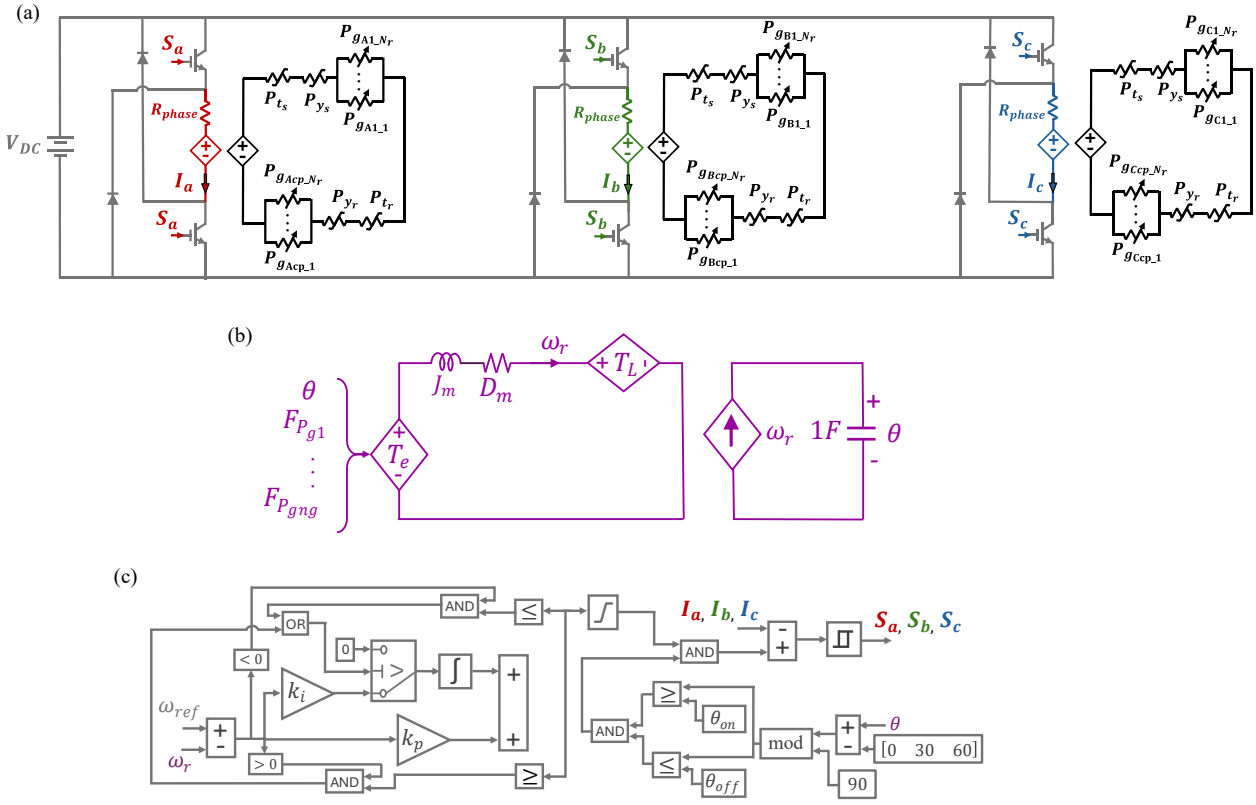


Figure 5.37 Circuit-based EMT model of SRM's drive system, (a) type-3 lumped magnetic model seamlessly coupled with the power converter, (b) equivalent circuit representation of the machine's mechanical dynamics, (c) controller of SRM drive system

As shown in Figure 5.38 (a), the machine starts to work in the no-load condition ($T_L = 0$ Nm) and low speed ($\omega_{ref} = 100$ rpm) while there is a sudden increase in the load torque to $T_L = 4.5$ Nm at

$t = 0.01$ s. As shown in Figure 5.38 (b). the speed command is gradually increased from $\omega_{ref} = 100$ rpm to $\omega_{ref} = 2500$ rpm. The controller keeps the machine's speed to the speed command value by regulating the phase current, as depicted in Figure 5.38 (c). It is worth noting that other control schemes can also be used to control the proposed circuit-based model of the machine and converter.

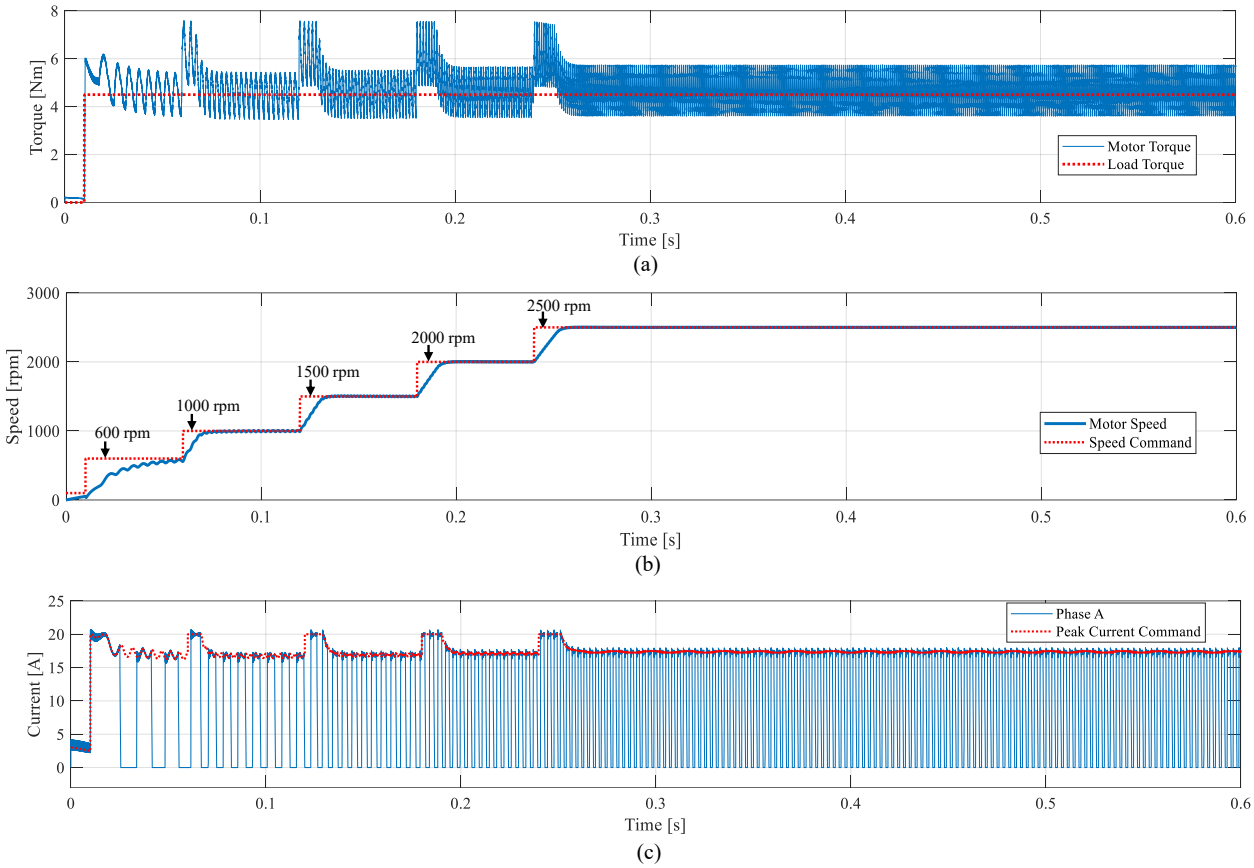


Figure 5.38 Transient behavior of SRM drive system due to the sudden changes in speed and load torque, (a) electromagnetic torque, (b) speed, (c) phase current

## 5.6 Conclusion

In this chapter, the circuit-based system-level EMT model of a power system representing an EV's power system is developed. This system includes the batteries, power electronic converters, electric machine, and their associated control systems. In the proposed EMT model, the detailed circuit-based model of the power electronic converters and battery are employed. The machine's EMT model is seamlessly integrated within the studied power system through a simultaneous solution approach.

Various transient studies were conducted, including the machine's internal faults, battery faults and their impact on the machine's internal magnetic behavior, as well as the system's transient behavior due to the sudden changes in load torque and speed. It is worth noting that for each transient study, the proper magnetic circuit model of the SRM is selected.

# CHAPTER 6 CONCLUSION

## 6.1 Summary of Thesis

The purpose of this thesis was to develop efficient and suitable machine models for various EMT studies, in conjunction with their external power circuits, particularly in case studies such as the power system of electric vehicles, which includes the battery system, various power electronic converters, and their associated control systems.

To this aim, we used the circuit-based approach. In this regard, the machine's EMT model consists of seamlessly coupled equivalent magnetic, electric, and mechanical circuits, where the performance of the machine's circuit based EMT model highly depends on the magnetic circuit.

In Chapter 2, the principle of using circuit-based approach to develop the EMT model of the EV power system is presented. This chapter demonstrates the modeling of the machine's EMT model which consists of interconnected magnetic, electric, and mechanical equivalent circuits. The magnetic behavior of various parts of the machine are modeled by magnetic circuits. The flux paths within machine's slots are modeled by linear permeances. The nonlinear permeances accounts for the magnetic behavior of the ferromagnetic core. These nonlinear permeances are implemented by their Norton companion model in the main system equations. The machine's rotation and flux path within the airgap is modeled by the variable permeances. The magnetic circuit seamlessly coupled with the electric circuit through mutators. The machine's torque is calculated by the co-energy method while the mechanical equations of the machine are represented by their equivalent circuit. Furthermore, the detailed circuit-based EMT model of the battery and power electronics devices are presented in this chapter.

In Chapter 3, various circuit-based EMT models of SRM are proposed. This chapter starts with proposing the lumped circuit-based model, which employs a limited number of equivalent magnetic elements to construct the magnetic circuit. The type-1 lumped model is the basic version, which does not consider the nonlinear magnetic behavior of the ferromagnetic core and assumes a cosine variation of the airgap permeance seen by each phase. In the type-2 model, the effect of saliency in the stator and rotor is accurately considered. By adding nonlinear permeances to the type-2 model to account for the MMF drop in the machine's ferromagnetic core, the type-3 lumped model was developed. Among these three types, only the type-3 model provided acceptable accuracy.

Furthermore, the topological model which uses the non-meshed permeance network is proposed. In this model, only one permeance is used to account for the flux path within each tooth and the yoke connecting two adjacent teeth. This model is more accurate than the lumped models due to the considering the effect of mutual couping. However it requires predefining the flux path and it neglects the flux path within the machine's slots.

To enhance the model's accuracy, the simplified distributed model is used. In this model, the mesh-based permeance network is used to build the magnetic circuit within the stator and rotor while the airgap is modeled by the non-meshed approach. In the proposed simplified distributed model, the radial direction can have any number of mesh divisions, but the number of mesh divisions in the orthoradial direction within each tooth and slot is limited to one.

Chapter 3 also introduces the distributed model, which employs the same methodology as the simplified distributed model. However, any number of mesh divisions can be applied in the radial and orthoradial directions, in this model. Thus, this model can account for all details and local magnetic phenomena happening inside the machine.

In Chapter 4, the proposed circuit-based EMT models of the SRM are verified and their performance are compared. All proposed magnetic models are compared in terms of accuracy and computational speed. The advantages and disadvantages of each model are highlighted, and based on these, each model is recommended for specific transient study scenarios.

In Chapter 5, the machine's EMT model are also integrated within an external system representing the EV's power system. This power system consists of batteries, power electronics converters, and their related control system. Various transient scenarios are studied, including those caused by control commands, faults in the external power system, and internal faults of the machine

## 6.2 Future Works

This research can be extended to address its limitations. These limitations can be summarized as follows:

1. The proposed machine models are developed in two dimensions. To apply these models to axial-flux machines, three-dimensional models should be developed. Moreover, using a three-dimensional model can further increase the model's accuracy.

2. The impact of transient phenomena on machine's losses, as well as on other physical behaviors of the machine, has not been completely investigated.

To further complete the ideas and methods presented in this thesis, the following topics are suggested for future studies:

**1- Applying the proposed circuit-based EMT models to other machine types**

The proposed models can be used to represent various electric machines and can be integrated into any external power system. The same circuit-based approach can be applied to model:

- Induction machines and their drive systems in a wide range of applications
- Interior permanent magnet synchronous machines in electric vehicles
- Synchronous machines in power systems
- Detailed model of the wind turbine systems consisting of doubly-fed induction machines and permanent magnet synchronous machines

**2- Adding loss modeling to the proposed circuit-based EMT models**

The calculation of magnetic losses can be added to the proposed circuit-based models of the machine. This can be achieved either through seamless coupling during the simulation or as a post-processing.

**3- Developing three-dimensional circuit-based EMT models**

The proposed circuit-based EMT model can be extended to three-dimensional analysis, which is particularly important for the study of axial flux machines. Due to the ability of the proposed circuit-based EMT models to seamlessly integrate with large and complex external circuits, this modeling approach offers a useful tool for simulating the power systems of in-wheel electric vehicles, where multiple axial flux machines are employed.

**4- Extending the proposed circuit-based EMT models to various multi-physics domains such as noise, vibration, and thermal analyses**

Various physical behaviors of the machine can be represented using the circuit-based approach and added to the proposed circuit-based EMT models. It would be interesting to investigate how transient phenomena, occurring inside or outside of the machine, affect its thermal behavior,

vibration, and noise. For such studies, the distributed circuit-based EMT model is recommended to be used.

**5- Verification of the proposed models by the experimental test setups**

The proposed models can be applied to prototype and experimental motor drive systems. This includes performing various tests on experimental setups, such as fault analysis in the machine, power electronic converters, and control systems.

# REFERENCES


[1] J. G. Hayes and G. A. Goodarzi, "*Electric powertrain: energy systems, power electronics and drives for hybrid, electric and fuel cell vehicles*," 2018.

[2] R. Mayer, M. B. El Kattel, and S. V. G. Oliveira, "Multiphase interleaved bidirectional DC/DC converter with coupled inductor for electrified-vehicle applications," *IEEE Transactions on Power Electronics*, vol. 36, no. 3, pp. 2533-2547, 2020.

[3] G. M. A. Watthewaduge, *A reluctance mesh-based modeling method for electromagnetic characterization and radial force calculation in switched reluctance machines*, Ph.D. dissertation, Dept. Electrical & Computer Eng., McMaster Univ., Hamilton, ON, Canada, Mar. 2022.

[4] A. M. Silva, C. H. Antunes, A. M. Mendes, and F. J. Ferreira, "Generalized reluctance network framework for fast electromagnetic analysis of radial-flux machines," *IEEE Transactions on Energy Conversion,* vol. 38, no. 1, pp. 310-320, 2022

[5] B. Bilgin, J. W. Jiang, and A. Emadi, "Switched reluctance motor drives: fundamentals to applications," *Boca Raton, FL,* 2018.

[6] A. Alsabbagh, M. Naïdjate, J. Mahseredjian, and M. Matehkolaei, "A Julia-based simulation platform for power system transients," *Electric Power Systems Research,* vol. 251, p. 112307, 2026.

[7] J. Mahseredjian, S. Dennetière, L. Dubé, B. Khodabakhchian, and L. Gérin-Lajoie, "On a new approach for the simulation of transients in power systems," *Electric power systems research,* vol. 77, no. 11, pp. 1514-1520, 2007.

[8] S. A. Mirnikjoo, K. Abbaszadeh, and S. E. Abdollahi, "Multiobjective design optimization of a double-sided flux switching permanent magnet generator for counter-rotating wind turbine applications," *IEEE Transactions on Industrial Electronics,* vol. 68, no. 8, pp. 6640-6649, 2020.

[9] S. A. Mirnikjoo, F. Asadi, K. Abbaszadeh, and S. E. Abdollahi, "Effect of rotor topology on the performance of counter-rotating double-sided flux switching permanent magnet generator," *IEEE Transactions on Energy Conversion,* vol. 37, no. 1, pp. 65-74, 2021.

[10] H.-M. Ahn, J.-Y. Lee, J.-K. Kim, Y.-H. Oh, S.-Y. Jung, and S.-C. Hahn, "Finite-element analysis of short-circuit electromagnetic force in power transformer," *IEEE Transactions on Industry Applications,* vol. 47, no. 3, pp. 1267-1272, 2011.

[11] A. Khaligh and M. Vakilian, "Power transformers internal insulation design improvements using electric field analysis through finite-element methods," *IEEE Transactions on Magnetics,* vol. 44, no. 2, pp. 273-278, 2008.

[12] Y. Bi and D. Jiles, "Finite element modeling of an electrically variable inductor," *IEEE transactions on magnetics,* vol. 35, no. 5, pp. 3517-3519, 2002.

[13] A. Canova and B. Vusini, "Design of axial eddy-current couplers," *IEEE Transactions on Industry Applications,* vol. 39, no. 3, pp. 725-733, 2003.

[14] F. Zare and Z. Nasiri-Gheidari, "Proposal of a 2DOF wound-rotor resolver," *IEEE Sensors Journal,* vol. 21, no. 17, pp. 18633-18640, 2021.

[15] H. Saneie, R. Alipour-Sarabi, Z. Nasiri-Gheidari, and F. Tootoonchian, "Challenges of finite element analysis of resolvers," *IEEE Transactions on Energy Conversion,* vol. 34, no. 2, pp. 973-983, 2018.

[16] X. Ling, B. Li, L. Gong, Y. Huang, and C. Liu, "Simulation of switched reluctance motor drive system based on multi-physics modeling method," *IEEE Access*, vol. 5, pp. 26184-26189, 2017.

[17] S. Dennetière, Y. Guillot, J. Mahseredjian, and M. Rioual, "A link between EMTP-RV and FLUX3D for transformer energization studies," *Electric power systems research*, vol. 79, no. 3, pp. 498-503, 2009.

[18] C. Lin, W. Wang, M. McDonough, and B. Fahimi, "An extended field reconstruction method for modeling of switched reluctance machines," *IEEE transactions on magnetics,* vol. 48, no. 2, pp. 1051-1054, 2012.

[19] M. Yin, N. Mohammed, N. Bracikowski, A. Pierquin, and D. Trichet, "Topology Optimization of Coaxial Magnetic Gear based on Reluctance Network Analysis," in *2024 International Conference on Electrical Machines (ICEM)*, 2024: IEEE, pp. 1-8.

[20] R. Nasiri-Zarandi, A. M. Ajamloo, and K. Abbaszadeh, "Proposing the output equations and 3-D MEC modeling for U-Core TFPM generators," in *2018 International Symposium on Power Electronics, Electrical Drives, Automation and Motion (SPEEDAM)*, 2018: IEEE, pp. 292-297.

[21] A. Beirami, H. F. Farahani, R. M. Rahimi, and S. Amini, "Dynamic analysis of Halbach coaxial magnetic gears based on magnetic equivalent circuit modelling," *IET Circuits, Devices & Systems,* vol. 15, no. 3, pp. 260-271, 2021.

[22] M. Naïdjate, N. Bracikowski, M. Hecquet, M. Fratila, M. M. Duro, and J.-P. Ducreux, "An intelligent reluctance network model for the study of large power and distribution transformers," in *2019 6th International Advanced Research Workshop on Transformers (ARWtr)*, 2019: IEEE, pp. 89-92.

[23] S. Mohammadi, M. Mirsalim, and S. Vaez-Zadeh, "Nonlinear modeling of eddy-current couplers," *IEEE Transactions on Energy Conversion,* vol. 29, no. 1, pp. 224-231, 2013.

[24] R. Nasiri-Zarandi, M. Farahzadi, and M. S. Toulabi, "Thermal Modeling of an Outer Rotor PM Assisted SynRM for the Electric Bike Applications Using a New 3-D LPTN," *IEEE Transactions on Transportation Electrification,* 2024.

[25] D. Liang, Z. Q. Zhu, R. Nilifard, Z. Azar, N. Madani, and J. B. Christensen, "Novel Lumped-parameter Thermal Modelling. Part I: Thermal Models for Cuboidal Components," *IEEE Transactions on Transportation Electrification,* 2024.

[26] D. Liang *et al.*, "A hybrid lumped-parameter and two-dimensional analytical thermal model for electrical machines," *IEEE Transactions on Industry Applications,* vol. 57, no. 1, pp. 246-258, 2020.

[27] J. O. Fiedler, K. A. Kasper, and R. W. De Doncker, "Calculation of the acoustic noise spectrum of SRM using modal superposition," *IEEE transactions on industrial electronics,* vol. 57, no. 9, pp. 2939-2945, 2010.

[28] M. Naïdjate, N. Bracikowski, M. Hecquet, M. Fratila, M. M. DURO, and J.-P. Ducreux, "A configurable reluctance network model for the study of large power and distribution transformers," in *2019 19th International Symposium on Electromagnetic Fields in Mechatronics, Electrical and Electronic Engineering (ISEF)*, 2019: IEEE, pp. 1-2.

[29] J. Mahseredjian, M. Naidjate, M. Ouafi, and J. A. O. Wilches, "Electromagnetic Transients Simulation Program: A unified simulation environment for power system engineers," *IEEE Electrification Magazine,* vol. 11, no. 4, pp. 69-78, 2023.

[30] A. Ruehli, "Partial element equivalent circuit (PEEC) method and its application in the frequency and time domain," in *Proceedings of symposium on electromagnetic compatibility*, 1996: IEEE, pp. 128-133.

[31] G. Antonini, A. E. Ruehli, D. Romano, and F. Loreto, "The partial elements equivalent circuit method: The state of the art," *IEEE Transactions on Electromagnetic Compatibility,* vol. 65, no. 6, pp. 1695-1714, 2023.

[32] D. M. Gamage, M. Ranasinghe, and V. Dinavahi, "Applications of the partial element equivalent circuit method in computational electromagnetics simulation: An overview," *Electric Power Systems Research,* vol. 243, p. 111487, 2025.

[33] A. Demenko, J. Sykulski, and R. Wojciechowski, "On the equivalence of finite element and finite integration formulations," *IEEE Transactions on Magnetics,* vol. 46, no. 8, pp. 3169-3172, 2010.

[34] M. Ranasinghe and V. Dinavahi, "Massively parallel hybrid TLM-PEEC solver and model order reduction for 3D nonlinear electromagnetic transient analysis," *IEEE Transactions on Electromagnetic Compatibility,* 2024.

[35] V. Dinavahi, “Transient analysis of systems with multiple nonlinear elements using TLM,” IEEE Trans. Power Syst., vol. 19, no. 4, pp. 2102–2103, Nov. 2004

[36] C. Christopolous and A. Zemanian, "The transmission-line modeling method TLM," *SIAM Review,* vol. 38, no. 4, p. 711, 1996.

[37] D. Fu, F. Gillon, Y. Xu, N. Bracikowski, and J. Gong, "Equivalent magnetic network of a transverse-flux permanent magnet linear motor," in *2018 XIII International Conference on Electrical Machines (ICEM)*, 2018: IEEE, pp. 2157-2163.

[38] D. Fu, J. Gong, Y. Xu, F. Gillon, and N. Bracikowski, "Coupled circuit and magnetic model for a transverse flux permanent magnet linear motor," *IEEE Access,* vol. 8, pp. 159274-159283, 2020.

[39] D. Cao, W. Zhao, J. Ji, L. Ding, and J. Zheng, "A generalized equivalent magnetic network modeling method for vehicular dual-permanent-magnet vernier machines," *IEEE Transactions on Energy Conversion,* vol. 34, no. 4, pp. 1950-1962, 2019.

[40] P. Naderi, S. Sharouni, and M. Heidary, "A novel analysis on a new DC-excited flux-switching machine using modified MEC method for ground power unit application," *IEEE Transactions on Energy Conversion,* vol. 35, no. 4, pp. 1907-1915, 2020.

[41] P. Naderi and M. Heidary, "A novel permanent magnet flux-switching linear motor performance analysis by flexible MEC method," *IEEE Transactions on Energy Conversion,* vol. 36, no. 3, pp. 1910-1918, 2020.

[42] D. Cao, W. Zhao, J. Ji, L. Ding, and J. Zheng, "A generalized equivalent magnetic network modeling method for vehicular dual-permanent-magnet vernier machines," *IEEE Transactions on Energy Conversion,* vol. 34, no. 4, pp. 1950-1962, 2019.

[43] G. Liu, Y. Wang, Q. Chen, G. Xu, and D. Cao, "Design and analysis of a new equivalent magnetic network model for IPM machines," *IEEE Transactions on Magnetics,* vol. 56, no. 6, pp. 1-12, 2020.

[44] D. Cao, B. Mecrow, J. Ji, and T. Liu, "Hybrid Network Model for PM Eddy Current Losses Considering Eddy Current Reaction Field and PWM Effects of PM Machine," *IEEE Transactions on Transportation Electrification,* 2024.

[45] G. Watthewaduge, E. Sayed, A. Emadi, and B. Bilgin, "Electromagnetic modeling techniques for switched reluctance machines: State-of-the-art review," *IEEE Open Journal of the Industrial Electronics Society,* vol. 1, pp. 218-234, 2020.

[46] M. Ghods, J. Faiz, H. Gorginpour, M. A. Bazrafshan, and J. K. Nøland, "Equivalent magnetic network modeling of variable-reluctance fractional-slot V-shaped Vernier permanent magnet machine based on numerical conformal mapping," *IEEE Transactions on Transportation Electrification,* vol. 9, no. 3, pp. 3880-3893, 2023.

[47] W. Peng and J. Gyselinck, "Magnetic-equivalent-circuit modelling of switched reluctance machines with mutual coupling effects," in *2016 XXII International Conference on Electrical Machines (ICEM)*, 2016: IEEE, pp. 426-432.

[48] W. Peng and J. Gyselinck, "Combined magnetic-equivalent-circuit and finite-element modelling of switched reluctance machines," in *2016 IEEE International Energy Conference (ENERGYCON)*, 2016: IEEE, pp. 1-6.

[49] V. Ostovic, *Dynamics of saturated electric machines*. Springer Science & Business Media, 2012.

[50] M. Rostami, P. Naderi, and A. Shiri, "Modelling and analysis of permanent magnet vernier machine using flexible magnetic equivalent circuit method," *IET Science, Measurement & Technology,* vol. 16, no. 3, pp. 160-170, 2022.

[51] S. Mirnikjoo, M. Naidjate, J. Mahseredjian, N. Bracikowski, and P. Akiki, "Electromagnetic Transient Modeling of Switched Reluctance Motor Drive System Using a Circuit-Based Approach," submitted to *XXIV Power Systems Computation Conference PSCC 2026, Limassol, Cyprus,* 2026.

[52] S. Alli, N. Bracikowski, L. Moreau, and M. Zaïm, "Reluctance network modeling of a low speed doubly salient permanent magnet machine," in *IECON 2017-43rd Annual Conference of the IEEE Industrial Electronics Society*, 2017: IEEE, pp. 2138-2143.

[53] J. Nazarzadeh and V. Naeini, "Magnetic reluctance method for dynamical modeling of squirrel cage induction machines," in *Electric machines and Drives*: IntechOpen Rijeka, Croatia, 2011, pp. 41-60.

[54] J. Lannoo, D. Vanoost, J. Peuteman, S. Debruyne, H. De Gersem, and D. Pissoort, "Improved air gap permeance model to characterise the transient behaviour of electrical machines using magnetic equivalent circuit method," *International Journal of Numerical Modelling: Electronic Networks, Devices and Fields,* vol. 33, no. 5, p. e2749, 2020.

[55] M. Ghods, H. Gorginpour, J. Faiz, M. A. Bazrafshan, and M. S. Toulabi, "Design and enhanced equivalent magnetic network modeling of a fractional-slot spoke-array vernier PM machine with rotor flux barriers," *IEEE Transactions on Energy Conversion,* vol. 38, no. 2, pp. 1060-1072, 2022.

[56] M. Ghods, J. Faiz, M. A. Bazrafshan, and M. H. Arianborna, "A mesh design technique for double stator linear PM Vernier machine based on equivalent magnetic network modeling," *IEEE Transactions on Energy Conversion,* vol. 37, no. 2, pp. 1087-1095, 2021.

[57] H. Dogan, L. Garbuio, H. Nguyen-Xuan, B. Delinchant, A. Foggia, and F. Wurtz, "Multistatic reluctance network modeling for the design of permanent-magnet synchronous machines," *IEEE transactions on magnetics,* vol. 49, no. 5, pp. 2347-2350, 2013.

[58] J. Gong, N. Bracikowski, and X. Wang, "Magnetic modeling of a linear motor using lumped approach," in *2014 17th International Conference on Electrical Machines and Systems (ICEMS)*, 2014: IEEE, pp. 1768-1773.

[59] G. Davarpanah, S. Mohammadi, and J. L. Kirtley, "Modelling of switched reluctance machines," *IET Electric Power Applications,* vol. 14, no. 11, pp. 1997-2006, 2020.

[60] M. Lambert, J. Mahseredjian, M. Martı, and F. Sirois, "Magnetic circuits within electric circuits: critical review of existing methods and new mutator implementations," *IEEE Transactions on Power Delivery,* vol. 30, no. 6, pp. 2427-2434, 2015.

[61] S. R. Pordanjani, J. Mahseredjian, M. Naïdjate, N. Bracikowski, M. Fratila, and A. Rezaei-Zare, "Electromagnetic modeling of inductors in EMT-type software by three circuit-based methods," *Electric Power Systems Research*, vol. 211, p. 108304, 2022.

[62] S. Mirnikjoo, M. Naidjate, J. Mahseredjian, N. Bracikowski, and P. Akiki, "Comprehensive Electromagnetic Transient Modeling of Switched Reluctance Motor Drive Sy," submitted to *IEEE Open Access Journal of Power and Energy*.

[63] S. R. Pordanjani, M. Naïdjate, N. Bracikowski, M. Fratila, J. Mahseredjian, and A. Rezaei-Zare, "Electromagnetic modeling of transformers in emt-type software by a circuit-based method," *IEEE Transactions on Power Delivery,* vol. 37, no. 6, pp. 5402-5413, 2022.

[64] S. Rahimi Pordanjani, *Electromagnetic Device Modeling by Circuit-Based Methods*, Ph.D. dissertation, Polytechnique Montréal, 2022.

[65] U. Karaagac, J. Mahseredjian, and O. Saad, "An efficient synchronous machine model for electromagnetic transients," *IEEE transactions on power delivery,* vol. 26, no. 4, pp. 2456-2465, 2011.

[66] S. D. Sudhoff, *Power magnetic devices: a multi-objective design approach*. John Wiley & Sons, 2021.

[67] U. Karaagac, J. Mahseredjian, R. Gagnon, H. Gras, H. Saad, L. Cai, I. Kocar, A. Haddadi, E. Farantatos, S. Bu, K. W. Chan, and L. Wang, "A generic EMT-type model for wind parks with permanent magnet synchronous generator full size converter wind turbines," *IEEE Power and Energy Technology Systems Journal,* vol. 6, no. 3, pp. 131-141, 2019.

[68] EMTP, *Battery Model Help File*, 2025. [Online].

[69] R. Palka, "Operation of High-Speed Switched Reluctance Machines with a Non-Uniform Air Gap," *Energies,* vol. 18, no. 12, p. 3033, 2025.

[70] S. Mirnikjoo, N. Bracikowski, M. Naidjate, J. Mahseredjian, and P. Akiki, "Assessment of Circuit-Based Electromagnetic Transient Models of Switched Reluctance Machine," submitted to *XXIV Power Systems Computation Conference PSCC 2026,* Limassol, Cyprus, 2026

[71] M. Chakir, "Conception et optimisation de la performance d'une génératrice à réluctance variable," 2010.

[72] S. Mohammadi and M. Mirsalim, "Design optimization of double-sided permanent-magnet radial-flux eddy-current couplers," *Electric Power Systems Research,* vol. 108, pp. 282-292, 2014.

[73] G. Davarpanah, S. Mohammadi, J. H. Lang, and J. L. Kirtley, "Two-phase switched reluctance motor with hybrid excitation: Modeling and evaluation," *IET Electric Power Applications,* vol. 17, no. 7, pp. 939-951, 2023.

[74] K. Nakamura, K. Kimura, and O. Ichinokura, "Electromagnetic and motion-coupled analysis for switched reluctance motor based on reluctance network analysis," *Journal of Magnetism and Magnetic Materials,* vol. 290, pp. 1309-1312, 2005.

[75] N. K. Sheth and K. Rajagopal, "Calculation of the flux-linkage characteristics of a switched reluctance motor by flux tube method," *IEEE Transactions on Magnetics,* vol. 41, no. 10, pp. 4069-4071, 2005.

[76] B. Multon Principe et éléments de dimensionnement des machines à réluctance variable à double saillance autopilotées in *Journées de la section électrotechnique du club EEA 1993*.

[77] J. Dong, B. Howey, B. Danen, J. Lin, J. W. Jiang, B. Bilgin, and A. Emadi, "Advanced dynamic modeling of three-phase mutually coupled switched reluctance machine," *IEEE Transactions on Energy Conversion,* vol. 33, no. 1, pp. 146-154, 2017.

[78] Z. Wang, X. Cao, Z. Deng, and J. Cai, "Electromagnetic modeling and investigation for bearingless switched reluctance motor considering magnetic saturation," *IEEE transactions on energy conversion,* vol. 38, no. 1, pp. 122-133, 2022.

[79] Ahamed, F. (2025). *Electric Vehicle Powertrain Modelling using Simulink* (Version 1.0.2).

[80] V. Nasirian, S. Kaboli, A. Davoudi, and S. Moayedi, "High-fidelity magnetic characterization and analytical model development for switched reluctance machines," *IEEE Transactions on Magnetics,* vol. 49, no. 4, pp. 1505-1515, 2012

[81] R. B. Inderka and R. W. De Doncker, "DITC-direct instantaneous torque control of switched reluctance drives," *IEEE Transactions on Industry Applications,* vol. 39, no. 4, pp. 1046-1051, 2003.

[82] P. Azer, B. Bilgin, and A. Emadi, "Mutually coupled switched reluctance motor: Fundamentals, control, modeling, state of the art review and future trends," *IEEE Access,* vol. 7, pp. 100099-100112, 2019.

[83] E. Ofori, "A Pulse Injection Based Sensorless Position Estimation Method for a Switched Reluctance Motor over a Wide Speed Range," University of Akron, 2014.

[84] C. Roux and M. M. Morcos, “On the use of a simplified model for switched reluctance motors,” IEEE Trans. Energy Convers., vol. 17, no. 3, pp. 400–405, Sep. 2002.

[85] X.-D. Xue, K. Cheng, and S. Ho, “Simulation of switched reluctance motor drives using two-dimensional bicubic spline,” IEEE Trans. Energy Convers., vol. 17, no. 4, pp. 471–477, Dec. 2002.

[86] X. Xue, K. Cheng, and S. Ho, “A self-training numerical method to calculate the magnetic characteristics for switched reluctance motor drives,” IEEE Trans. Magn., vol. 40, no. 2, pp. 734–737, Mar. 2004.

[87] H.-J. Chen, D.-Q. Jiang, J. Yang, and L.-X. Shi, “A new analytical model for switched reluctance motors,” IEEE Trans. Magn., vol. 45, no. 8, pp. 3107–3113, Aug. 2009.

[88] M. Farshad, J. Faiz, and C. Lucas, “Development of analytical models of switched reluctance motor in two-phase excitation mode: Extended miller model,” IEEE Trans. Magn., vol. 41, no. 6, pp. 2145–2155, Jun. 2005.

[89] D. Torrey and J. Lang, “Modelling a nonlinear variable-reluctance motor drive,” IEE Proc. B (Electric Power Appl.), vol. 137, no. 5, pp. 314–326, Sep. 1990.

[90] S. Mir, I. Husain, and M. E. Elbuluk, “Switched reluctance motor modeling with on-line parameter identification,” IEEE Trans. Ind. Appl., vol. 34, no. 4, pp. 776–783, Aug. 1998.

[91] J. Y. Loh, M. A. Prabhu, S. Wang, S. C. Joshi, V. Viswanathan, and S. Ramakrishna, “Optimal segmented rotor design for the embedded electrical machine for the more electric aircraft,” J. Eng., vol. 2019, no. 17, pp. 4321–4324, Jun. 2019.

[92] S. Song, M. Zhang, and L. Ge, “A new decoupled analytical modeling method for switched reluctance machine,” IEEE Trans. Magn., vol. 51, no. 3, Mar. 2015, Art. no. 8100504.

[93] S. A. Hossain and I. Husain, “A geometry based simplified analytical model of switched reluctance machines for real-time controller implementation,” IEEE Trans. Power Electron., vol. 18, no. 6, pp. 1384–1389, Nov. 2003.

[94] A. Khalil and I. Husain, “A Fourier series generalized geometry-based analytical model of switched reluctance machines,” IEEE Trans. Ind. Appl., vol. 43, no. 3, pp. 673–684, Jun. 2007.

[95] F. R. Salmasi and B. Fahimi, “Modeling switched-reluctance machines by decomposition of double magnetic saliencies,” IEEE Trans. Magn., vol. 40, no. 3, pp. 1556–1561, May 2004.

[96] J. R. Camacho and R. E. Araújo, *Modelling and Control of Switched Reluctance Machines*. IntechOpen, 2020.

[97] S. Mirnikjoo, N. Bracikowski, M. Naidjate, J. Mahseredjian, and P. Akiki, "Electromagnetic Transient Modeling of Switched Reluctance Motor Drive System by a Circuit-based Method," accepted in *IECON 2025-51st Annual Conference of the IEEE Industrial Electronics Society,* Madrid, Spain, 2025.

[98] S. Mirnikjoo, M. Naidjate, J. Mahseredjian, N. Bracikowski, and P. Akiki, "Detailed Electromagnetic Transient Model of Switched Reluctance Motor Drive System," *Electric Power Systems Research,* vol. 251, p. 112230, 2026.

[99] S. Mirnikjoo, M. Naidjate, J. Mahseredjian, N. Bracikowski, and P. Akiki, “Detailed circuit-based model of switched reluctance motor drive system for electromagnetic transient studies,” in *Proc. CIGRE 2025 International Symposium*, Montréal, QC, Canada, 2025.